sciendo

Contributions to Geophysics and Geodesy Vol. 49/3, 2019 (229–247)

A least-squares minimization approach to interpret gravity anomalies caused by a 2D thick, vertically faulted slab

El-Sayed ABDELRAHMAN, Mohamed GOBASHY

Geophysics Department, Faculty of Science, Cairo University, Giza, Egypt;
e-mail: sayed5005@yahoo.com, bouguer3000@yahoo.com

Abstract: We present a least-squares minimization approach to estimate simultaneously the depth to and thickness of a buried 2D thick, vertically faulted slab from gravity data using the sample spacing – curves method or simply s-curves method. The method also provides an estimate for the horizontal location of the fault and a least-squares estimate for the density contrast of the slab relative to the host. The method involves using a 2D thick vertical fault model convolved with the same finite difference second horizontal gradient filter as applied to the gravity data. The synthetic examples (noise-free and noise affected) are presented to illustrate our method. The test on the real data (Central Valley of Chile) and the obtained results were consistent with the available independent observations and the broader geological aspects of this region.

Key words: gravity thick fault, depth and thickness solutions, s-curves method, least-squares method

1. Introduction

A number of simple model geometries have been used to model the gravitational effect of the vertical fault. Many previous workers have assumed an infinite vertical step and chosen a geometry where one or more semi-infinite thin horizontal sheets are terminated by a vertical fault plane (*Nettleton, 1942; Grant and West, 1965; Sharma and Vyas, l970; Geldart et al., 1966; Gupta, 1983; Blakely and Simpson 1986; Klingelé et al., l991; Abdelrahman et al., 2003; Abdelrahman and Essa, 2015*). *Gendzwill (1970)* examined a different scenario where the fault was represented by a horizontal slab that was divided into 3 regions. The fault itself was associated with the central region, with linear density distribution, limited by constant density of surrounded sectors. In this paper, we examine the use of a truncated thick slab to represent a vertical fault. We present a methodology for simultaneously

doi: 10.2478/congeo-2019-0012

estimating the depth to and thickness of the slab as well as the density contrast.

The gravitational effect of some simple bodies (e.g., sphere, horizontal cylinder, vertical cylinder) is of symmetrical shape (with respect to horizontal coordinates). On the other hand, the effect of vertical fault is asymmetrical in the direction of horizontal profile. If geological knowledge suggests that a horizontally layered sequence is present, and that the vertical throw of the interpreted fault is large compared to the depth to the layer with a density contrast relative to the host, it is safe to simplify the model under consideration to just a truncated horizontal slab on the upthrown side of the fault. A 2D approximation can be used when the strike length of the fault is greater than the depth to the top of the faulted slab. Despite very significant differences in mathematical complexity, the expressions for calculating gravity effects of thin and thick truncated horizontal slabs produce responses that are difficult to distinguish. We argue that a slab with finite thickness (i.e., the thick slab model) be used in preference to the thin slab model. We assume the 2D thick, vertically faulted slab is characterized by: 1) semi infinite thick slab, 2) a density contrast relative to the host density, 3) a thickness that is significant in relation to the depth of burial, 4) a strike length that is large relative to the depth of burial, 5) a truncated vertical plane where the plane is perpendicular to a profile of vertical gravity measurements, 6) equi-spaced measurements along the profile and all taken at the same elevation, and 7) a vertical throw which is large when compared with the depth of burial.

Several methods have been used to interpret gravity data due to faults. *Geldart et al. (1966)* described a method of interpreting 2D gravity data of a single bed that is cut by a flat fault plane of arbitrary dip angle, taking into account the bed in both the upthrown and downthrown blocks. *Sharma and Vyas (1970*) presented a graphical methodology to interpret gravity data of a 2D fault cutting a series of beds. *Parasnis (1973)* showed the application of a vertical fault model to various geological scenarios, and how the gravity data of one or more thick truncated 2D slabs can be used to model these geological situations. *Telford et al. (1976)* developed the equation for modeling a thick slab with a dipping truncation plane and describe the application even if the depth of overburden is less than about twice the thickness of the slab. However, most of these methods are highly subjec-

tive in determining the fault parameters and can not be applied directly to measured gravity data consisting of the combined effect of a local structure (2D thick, vertically faulted slab) and a regional polynomial of zero or first order, i.e., some preparatory work is necessary to isolate a residual from the input data.

On the other hand, numerical methods are widely used to interpret gravity data due to simple structures. *Gupta (l983)* developed a least-squares approach to depth determination from gravity data due to sphere, cylinder, and first horizontal gradient of gravity data due to a thin faulted layer. *Abdelrahman et al. (1987)* showed the effectiveness of the least-squares method in determining depths to a vertical step (thin plate approximation) and a horizontal cylinder from second vertical gradient maps by finding a solution of a non-linear equation in depth. *Abdelrahman and El-Araby (1993)* suggested a least-squares approach to depth determination from moving average residual gravity profiles.

Finally, continuous modeling methods are excellent in determining the depth and the thickness of a buried faulted structure from gravity data (*Talwani et al., l959; Tanner, 1967; Cordell and Henderson, l968*). In these methods, iterative 2D and 3D solutions of gravity data were suggested. Given girded gravity values and certain limited restrictions on the mass distribution, a 2D or 3D structural model can be calculated automatically from gravity data by successive approximations.

In the present paper, we describe a least-squares minimization approach to estimate simultaneously the depth to and the thickness of a buried 2D thick, vertically faulted slab from gravity data using a technique that is termed the "s-curves method". Our method involves using a 2D thick vertical fault model convolved with the same finite difference second horizontal gradient filter as applied to the gravity data. The method also provides an estimate for the horizontal location of the fault and a least-squares estimate for the density contrast of the slab relative to the host. The method is similar to Euler deconvolution, but it solves not only for depth to the source but also the thickness independently. A scheme for analysis of gravity data has been formulated to determine the model parameters of the 2D thick, vertically faulted slab. We apply the method to synthetic data with and without random noise, and tested it on a field example from Central Valley of Chile.

2. The method

The direct problem for the 2D vertical fault (or semi-infinite Bouguer slab) can be derived with reference to the solid angle concept and is given by *Telford et al. (1976)* as:

$$g(x,t,d) = 2G\sigma\left[x\,\ln\frac{\sqrt{x^2+(d+t)^2}}{\sqrt{x^2+d^2}} + \pi t/2 + \right. \\ \left. + (t+d)\,\mathrm{atan}\left(\frac{x}{d+t}\right) - d\,\mathrm{atan}\left(\frac{x}{d}\right)\right], \tag{1}$$

where $g(x,t,d)$ is the gravitational effect of the 2D vertical fault, d is the depth to the top of the slab, t is the thickness of the slab, x is the horizontal position coordinate, G is the gravitational constant, and σ is the density contrast of the slab. The 2D thick, vertically faulted slab model is shown in Fig. 1.

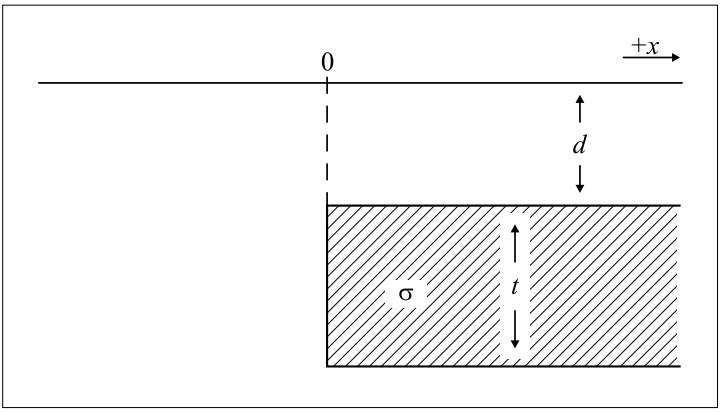

Fig. 1. Vertical schematic section through a 2D thick, vertically faulted slab. The fault is located at $x = 0$ on the horizontal coordinate axis. The slab has a thickness of t and the top of the slab is buried at a depth d. The slab has a density contrast of σ relative to the host density.

Consider five observation points $x_i + 2s$, $x_i + s$, x_i, $x_i - s$, and $x_i - 2s$ on the gravity profile where $s = k\,s_0,\ k = 1, 2, 3, ..., M$ spacing units and is called the graticule spacing and where s_0 is the fundamental sample spacing (*Hammer, 1977*). The numerical first horizontal gradient computed from gravity data is defined as:

$$g_x(x_i) = \frac{g(x_i + s) - g(x_i - s)}{2s}, \qquad i = 1, 2, 3, \ldots, N. \tag{2}$$

Using Eq. (2), the numerical second horizontal gradient computed from gravity data is then defined (*Levy, 2010*) as:

$$g_{xx}(x_i) = \frac{g(x_i + 2s) - g(x_i) + g(x_i - 2s)}{4s^2}. \tag{3}$$

Substituting (1) in (3), we obtain:

$$g_{xx}(x_i, t, d, s) = G\sigma W(x_i, t, d, s)/2s^2, \tag{4}$$

where

$$\begin{aligned} W(x_i, t, d, s) = {} & (x_i + 2s) \ln \frac{\sqrt{(x_i + 2s)^2 + (d + t)^2}}{\sqrt{(x_i + 2s)^2 + d^2}} + \\ & + (t + d) \operatorname{atan}\left(\frac{x_i + 2s}{t + d}\right) - d \operatorname{atan}\left(\frac{x_i + 2s}{d}\right) + \\ & - 2x_i \ln \frac{\sqrt{x_i^2 + (d + t)^2}}{\sqrt{x_i^2 + d^2}} - 2(t + d) \operatorname{atan}\left(\frac{x_i}{t + d}\right) + \\ & + 2d \operatorname{atan}\left(\frac{x_i}{d}\right) + (x_i - 2s) \ln \frac{\sqrt{(x_i - 2s)^2 + (d + t)^2}}{\sqrt{(x_i - 2s)^2 + d^2}} + \\ & + (t + d) \operatorname{atan}\left(\frac{x_i - 2s}{t + d}\right) - d \operatorname{atan}\left(\frac{x_i - 2s}{d}\right). \end{aligned} \tag{5}$$

Eq. (4) gives the following value at $x_i = s$:

$$g_{xx}(s) = G\sigma W(t, d, s)/2s^2, \tag{6}$$

where

$$\begin{aligned} W(t, d, s) = {} & 3s \ln \frac{\sqrt{9s^2 + (d + t)^2}}{\sqrt{9s^2 + d^2}} + (t + d) \operatorname{atan}\left(\frac{3s}{t + d}\right) + \\ & - d \operatorname{atan}\left(\frac{3s}{d}\right) - 3s \ln \frac{\sqrt{s^2 + (d + t)^2}}{\sqrt{s^2 + d^2}} + \\ & - 3(t + d) \operatorname{atan}\left(\frac{s}{t + d}\right) + 3d \operatorname{atan}\left(\frac{s}{d}\right). \end{aligned} \tag{7}$$

Using (6), (4) can be written as:

$$g_{xx}(x_i, t, d, s) = g_{xx}(s)\, W(x_i, t, d, s)/W(t, d, s)\,. \tag{8}$$

The unknown depth d in (8) can be obtained by minimizing:

$$\psi(d) = \min \|g_{xx}(x_i) - g_{xx}(s)\, W(x_i, t, d, s)/W(t, d, s)\|_2^2\,, \tag{9}$$

where $g_{xx}(x_i)$ represents the numerical second horizontal gradient computed from gravity data using Eq. (3) at x_i and where $g_{xx}(s)$ is a fixed numerical value at $x_i = s$ computed from the second horizontal gradient profile thus obtained, provided that the thickness t is known and remained constant in the process.

The minimization of the objective function is based on using the MATLAB function "lsqnonlin" which solves nonlinear least-squares problems of the form given in (9) (*Mathworks, 2018*). The "lsqnonlin" requires the user-defined function to compute the *vector*-valued function:

$$\psi(d) = \begin{bmatrix} \psi_1(d) \\ \psi_2(d) \\ \psi_3(d) \\ . \\ . \\ . \\ \psi_n(d) \end{bmatrix}. \tag{10}$$

Then, in vector terms, one can restate this optimization problem as:

$$\min_d \|\psi(d)\|_2^2 = \min_d \left(\psi_1(d)^2 + \psi_2(d)^2 + \psi_3(d)^2 + \ldots \psi_n(d)^2\right), \tag{11}$$

where d is a depth vector and $\psi(d)$ is a function that returns a vector value $d = \text{lsqnonlin}(\psi(d), d\_initial)$ starts at the depth $d\_initial$ (to be used only in the first iteration) and finds a minimum of the sum of squares of the functions described in $\psi(d)$. The minimization is performed using the Levenberg-Marquardt algorithm which uses a search direction that is a cross between the Gauss-Newton direction and the steepest descent direction. Any reasonable guess for d works well because there is only one minimum which is the global minimum (Fig. 2). In Fig. 2, we demonstrate an example of the objective function space when $s = 1\,\text{km}$, $t = 1\,\text{km}$, and initial guess of $d = 1\,\text{km}$ in case the model parameters are [$t = 9\,\text{km}$, $d = 5\,\text{km}$,

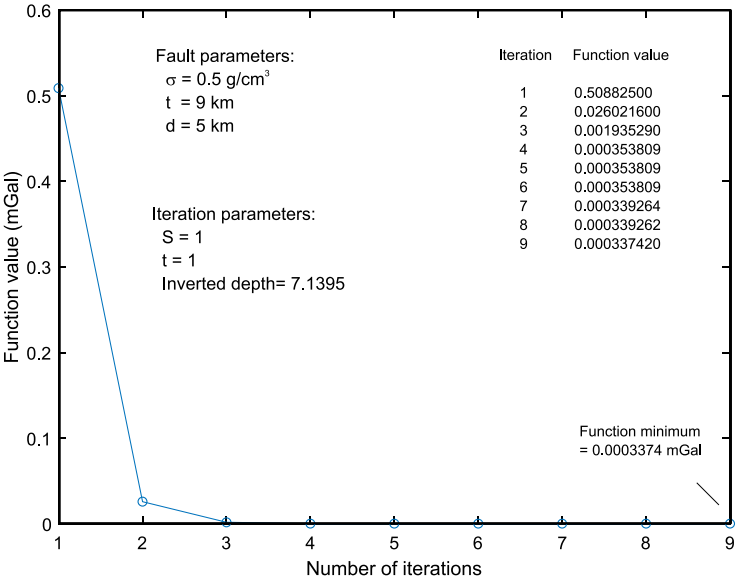

Fig. 2. A numerical example of the objective function space when $s = 1$ km, $t = 1$ km, and initial guess of $d = 1$ km in case the model parameters are: $t = 9$ km, $d = 5$ km, $\sigma = 0.5$ g/cm^3, profile length of 80 km, and sample interval of 1 km.

$\sigma = 0.5$ g/cm^3, profile length of 80 km, and sample interval of 1 km]. It is clear that among the function space, only one minimum is achieved at (iteration number 9) where the minimum is 0.0003374 mGal, which is at the same time as the global minimum. This shows that the function is generally concave and consequently the algorithm always converges to the minimum. In this case, any initial guess for d will work well.

Eq. (9) represents a parametric family of curves for different values of "s" (i.e., different sample spacings) and thus it can be used not only to determine depth d but also to estimate simultaneously the thickness of the buried fault t. For a fixed parameter s, the computed depths are plotted against the thickness values representing a continuous curve. The solution for the depth and the thickness of buried faulted slab is read at the common intersection of the curves. Theoretically, any two curves of the parameters are enough to simultaneously determine d and t. The curves intersect at the true values of d and t because (9) has only two unknowns. In practice, more than two values of graticule or sample spacing are desirable because

of the presence of noise in the data.

Finally, substituting the computed depth d_c and thickness t_c in (4) as fixed parameters and applying the least-squares method, we obtain the density contrast $\sigma(s)$ for any graticule spacing s as:

$$\sigma(s) = \sum \frac{2s^2 \left[g_{xx}(x_i)\, W(x_i, t_c, d_c, s)\right]}{G[W(x_i, t_c, d_c, s)]^2} \,. \tag{12}$$

The present method is capable of determining the model parameters, particularly the depth and the thickness of a buried thick vertically faulted slab from gravity data given in a small area over the buried structure, i.e., from a small segment of the gravity profile around the origin. In addition, the second horizontal gradient profiles exhibit a zero crossover at the origin (i.e., $x = 0$), hence, our method provides a simple way to estimate the horizontal location of the fault.

An automatic interpretation scheme based on the above equations for analyzing field data is as follows:

1) Digitize the anomaly profile at N data points.
2) Produce a set of second horizontal gradient profiles by applying the second horizontal gradient filter with different sample spacing values to the profile data set. The horizontal distance at which the second gradient profiles attain their zero value is taken as the origin of the gravity profile (i.e., $x = 0$). The default choice of the graticule spacing s is taken as $s = 5$ starting from $s = 1$ sampling interval.
3) For each second horizontal gradient profile, use (9) to determine the depth d of the buried fault structure for assumed values of thickness t. The default choice of the thickness values t is taken from 1 to 12 units every one sampling interval.
4) Construct the "s-curves" by plotting the computed depths against the thickness values for each s. The solution for the depth and thickness of buried faulted slab is read at the common intersection of the curves. The choice of the appropriate graticule spacings s) is based upon the resolution of the resulted intersected curves. If the intersection is not clear, the interpreter should use another set of graticule spacings (e.g. from s equals 6 to 10 sampling units).

A flowchart based on the above method for analyzing gravity data is shown in Fig. (3).

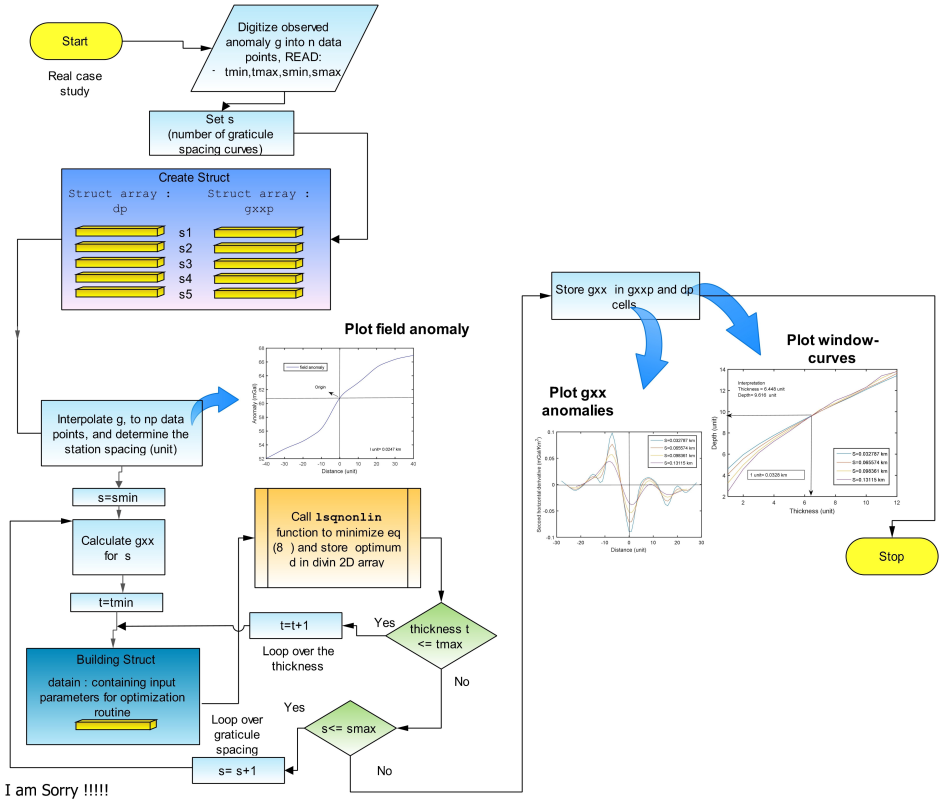

Fig. 3. A flowchart based on the present method for analyzing gravity data.

3. Theoretical examples

3.1. Noise free data

A composite synthetic example consisting of the combined gravity effect of a 2D thick, vertically faulted slab ($t = 9$ km, $d = 5$ km, $\sigma = 0.5$ g/cm^3, profile length $= 80$ km, and sample interval $= 1$ km) and a first-order regional polynomial (Fig. 4) was computed to allow us to demonstrate our method

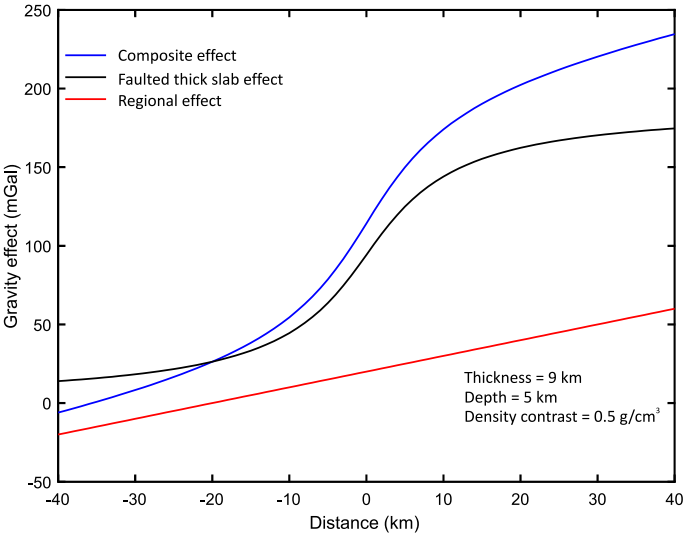

Fig. 4. A composite gravity profile consisting of the combined gravity effects due to a 2D thick vertically faulted slab ($t = 9$ km, $d = 5$ km, $\sigma = 0.5$ g/cm^3, profile length of 80 km, and sample interval of 1 km) and a regional component represented by a first-order polynomial.

for estimating the location, density contrast, depth to and thickness of the faulted thick slab. We produced profiles of the second horizontal gravity gradient using the discrete form of calculation (Eq. (3)) for values of the sample interval, s, of 1, 2, 3, 4, and 5 km (Fig. 5). The use of the second horizontal gradient filter has the effect of suppressing the longer wavelength components of the data in favor of the shorter wavelength components that are related to the buried truncated slab. Profiles for values of "s" greater than 5 km could have been calculated but the gradient profiles would continue to shrink in length due to the inability to calculate the result at locations close to either end of the profile.

Eq. (9) was applied to each point of the five-second horizontal gradient gravity profiles, yielding depth solutions for each of the thickness values that were proposed. The computed depths were plotted against the thickness values to produce the curves shown in Fig. 6. This figure shows the intersection at the correct location $t = 9$ km and $d = 5$ km. In this case, the solutions for the depth and thickness are in excellent agreement with the input model defined above.

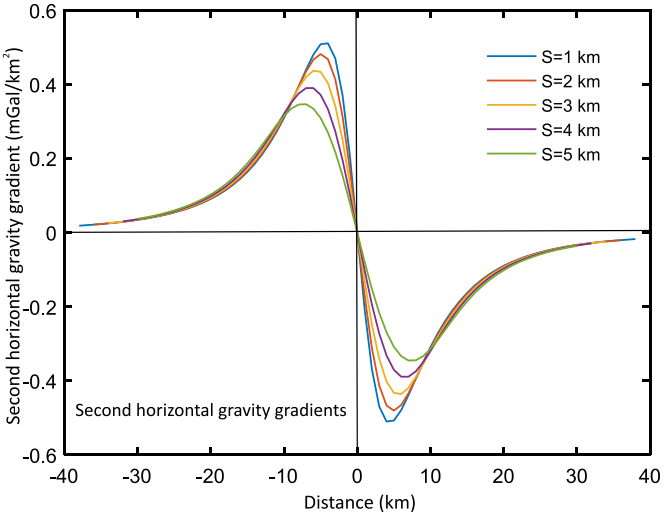

Fig. 5. Profiles of the discrete second horizontal gravity gradients for the composite field shown in Fig. 4. The gradients were calculated using a 3-point moving sampling spacing. The profiles represent the results that would be obtained using different gravity sample values (i.e., $s = 1, 2, 3, 4$, and 5 km).

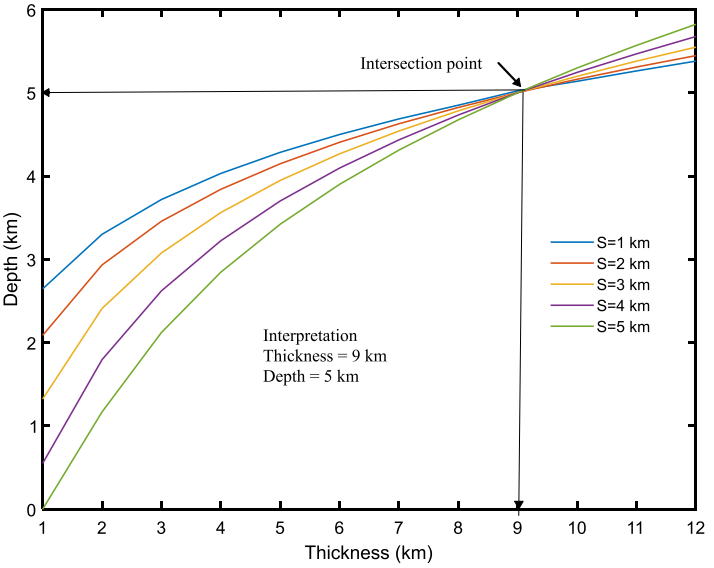

Fig. 6. Family of s-curves of thickness t as a function of depth to top d for sample interval s of 1, 2, 3, 4, and 5 km obtained from noise free composite gravity data using the present approach.

3.2. Effect of noise

The noise term in the measured signal, traditionally is related to the measurement errors (including instrumental errors). In the context of potential field analysis, two more types of noise are present, namely, earth noise (contribution from other neighboring undesired sources) and model errors (results from simplifying the real complex model). A common property of noise from all sources is the presence of significant power in the high frequency band. In the limiting case, we have white noise which has equal power in the entire frequency band of the observation (*Naidu and Mathew, 1998*). The measurement noise is more likely to be white noise. On the above basis, we implemented white noise in the simulation study. In our work, the "awgn" MATLAB function is used and the noise power is implemented. In this case, the SNR $= 20 \log_{10}(X^2/Y^2)$, where X represents the input signal and Y represents the noise. The SNR in the "awgn" function used specifies the (signal/noise) / sample in dB. The power used in "awgn" is measured from the input observed regularly spaced data $X(N)$. In this

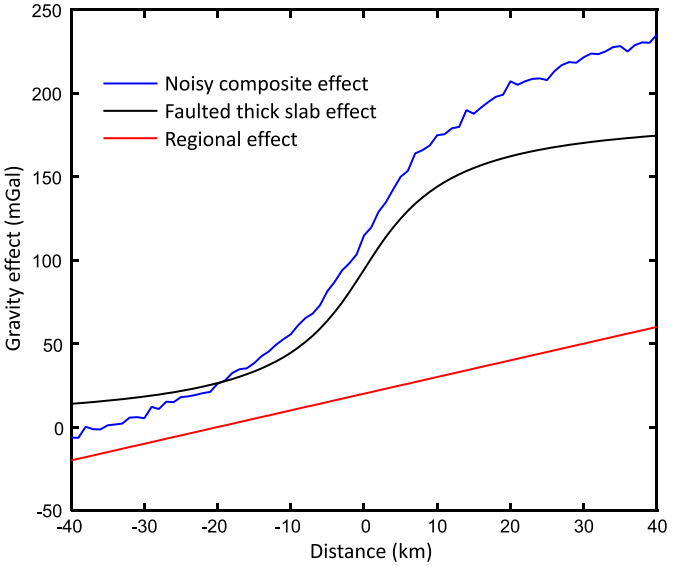

Fig. 7. A noisy composite gravity profile consisting of the combined effects due to a 2D thick, vertically faulted slab ($t = 9$ km, $d = 5$ km, $\sigma = 0.5$ g/cm^3 is the density contrast of the slab relative to the host, profile length $= 80$ km, and sample interval $= 1$ km) and a regional component represented by a first-order polynomial.

subsection, we investigate the effect of adding random noise.

The computed gravity effect of Fig. 4 was contaminated with 20 dB random noise (Fig. 7). The noisy composite gravity data thus obtained were subjected to the second horizontal gravity gradients filter to produce noisy second horizontal gravity gradients (Fig. 8). The second horizontal gravity gradients due to noisy data are more dominated in the right side of the Fig. 8 as compared to the left side. This is due to the fact the truncated slab is located below the positive profile values w.r.t. the start profile, i.e. zero crossing where the main part of the gravity effect of the truncated slab is emphasized. The gravity data below the positive is greatly affected by the second horizontal gradient filter compared with gravity data located below the negative profile side. Adapting the same interpretation technique described above, the results are shown in Fig. 9. The "s-curves" intersect each other at the location $t = 8.85$ km and $d = 4.94$ km. This demonstrates that our method can give reliable results even when the gravity data contains measurement errors or geological noise.

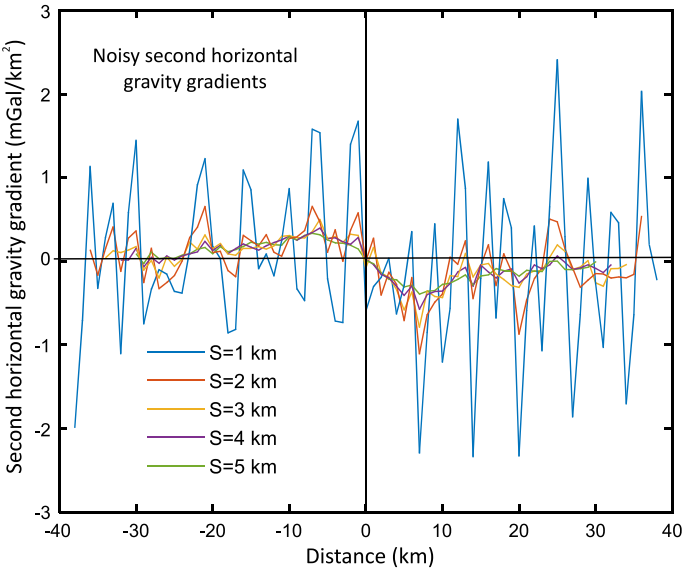

Fig. 8. Profiles of the discrete noisy second horizontal gravity gradients for the composite field shown in Fig. 7. The gradients were calculated using a 3-point sampling spacing. The profiles represent the results that would be obtained using different gravity sample values (i.e., $s = 1, 2, 3, 4,$ and 5 km).

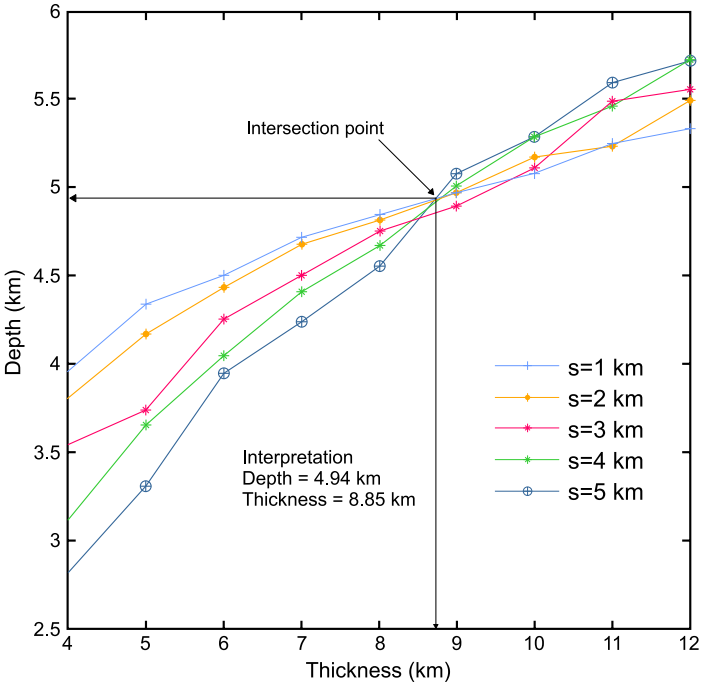

Fig. 9. Family of s-curves of t as a function of d for $s = 1, 2, 3, 4$, and 5 km as obtained from the noisy composite gravity data using the present approach.

4. Discussion

The present method assumes that the gravity data are regularly spaced and solution of Eq. 9) yields the exact value of depth and thickness when using synthetic data. Adding random noise to the synthetic data results in maximum uncertainties of ± 2.0 percent for parameters t and d.

For large s values, the number of samples on the second horizontal gradient curves decreases on both ends, which in turn may result in an instable interpretation curves. However, since the interpretation requires only a relatively short length profile, the problem may be solved effectively and economically by increasing the number of measurements made within the restricted length of the profile. At the same time, using a relatively short length of profile, results in a very high rejection of neighboring disturbances. The above explanation helps the user choose the proper s to use in Eq. (10).

The disadvantage of the present least-squares second horizontal gradient "*s*-curves" method is that it cannot be applied in complex geologic situations or areas with large-scale topographic and near-surface density variations. In this case, there is instability of the proposed inversion on the base of intersections of "*s*-curves".

5. Field example

To illustrate the practical application of the theory developed in the previous section, a field example from the Central Valley of Chile (*Garland, 1970*, the Figure 7.8, p. 116) is presented. A Bouguer anomaly profile across an outcropping fault structure in the basin is shown in Fig. 10 (*Lomnitz, l959*). The depth to the fault interpreted from surface geology and drilling information is about 0.15 km and the thickness estimated by *Lomnitz (l959)* using the Bouguer formula for a slab is about 2 km. The gravity profile of 16.55 km length has been digitized at an interval of 0.207 km. The Bouguer gravity anomalies thus obtained have been subjected to a separation technique using the second horizontal gradient method. Filters were applied

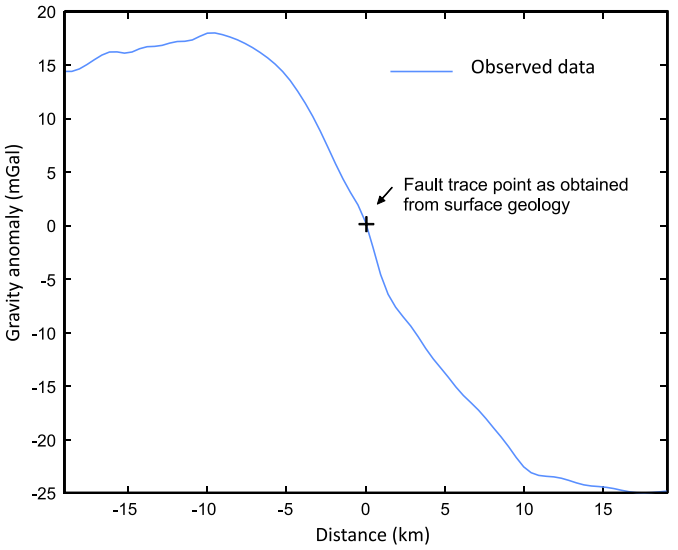

Fig. 10. Observed gravity anomaly over a 2D thick vertically faulted structure in the Central Valley of Chile (after *Lomnitz, l959*).

in four successive windows ($s = 2.482, 2.689, 2.896, 3.103$ km). In this way, four second horizontal gradient profiles were obtained (Fig. 11). The same procedure described for the synthetic examples was used to estimate the depth and the thickness of the fault. The results are shown in Fig. 12.

The result of the present study ($d = 0.19$ km and $t = 2.38$ km), based on the least-squares method, and that obtained from surface geology, drilling information, and application of the Bouguer formula for a horizontal slab are in a very good agreement.

6. Conclusions

The problem of determining the depth and the thickness of a 2D thick vertically faulted slab from second horizontal gradient gravity effects can be solved using the least-squares "s-curves" method described in this paper. The method involves fitting the response of a 2D thick vertical fault model convolved with the same second horizontal gradient filter as applied to the

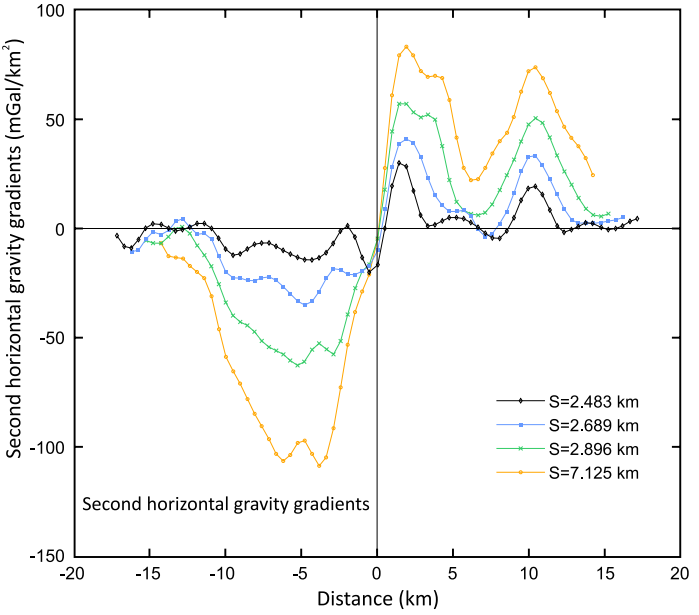

Fig. 11. Second horizontal gravity gradients due to a 2-D thick, vertically faulted structure, the Central valley of Chile for $s = 2.482, 2.689, 2.896, 3.103$ km.

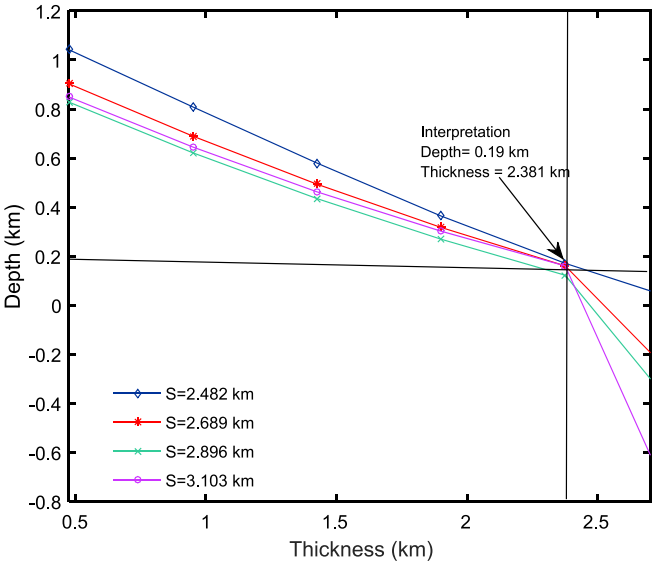

Fig. 12. Family of window curves of t as a function of d for $s = 2.482, 2.689, 2.896, 3.103$ km as obtained from the observed gravity anomaly due to a 2-D thick, vertically faulted structure, the Central valley of Chile, using the present approach.

observed data. Since the second horizontal gradient filter strongly attenuates any long wavelength regional component in the data, our method can be applied not only to data that have been pre-processed to remove a regional component but also to the measured Bouguer gravity data. The advantages of the present method over previous techniques are: (1) the least-squares "s-curves" method is a semi-automatic and computationally simple, and (2) the method is relatively stable when reasonable levels of noise is included in the observed data. The depth and thickness obtained by present method might be used to gain geologic insight concerning the subsurface. Synthetic and field examples illustrated the efficacy of the present method. The disadvantage of the present least-squares second horizontal gradient "s-curves" method is that it cannot be applied in complex geologic situations or areas with large-scale topographic and near-surface density variations.

Acknowledgements. The authors would like to thank the editors and the capable anonymous reviewer for their excellent suggestions and thorough review that improved our original manuscript.

References

Abdelrahman E. M., Bayoumi A. I., El-Araby H. M., 1987: A least-squares approach to depth determination from second derivative gravity anomalies due to two-dimensional faulted and folded structures with application to the Gulf of Suez region, Egypt. J. Afr. Earth Sci., **6**, 6, 857–860, doi: 10.1016/0899-5362(87)90044-3.

Abdelrahman E. M., El-Araby T., 1993: A least-squares minimization approach to depth determination from moving average residual gravity anomalies. Geophysics, **58**, 12, 1779–1784, doi: 10.1190/1.1443392.

Abdelrahman E. M., El-Araby H. M., El-Araby T. M., Abo-Ezz E. R., 2003: A least-squares derivatives analysis of gravity anomalies due to faulted thin slabs. Geophysics, **68**, 2, 535–543, doi: 10.1190/1.1567222.

Abdelrahman E. M., Essa K. S., 2015: Three least-squares minimization approaches to interpret gravity data due to dipping faults. Pure Appl. Geophys., **172**, 2, 427–438, doi: 10.1007/s00024-014-0861-4.

Blakely R. J., Simpson R. W; 1986: Approximating edges of source bodies from magnetic or gravity anomalies. Geophysics, **51**, 7, 1494–1498, doi: 10.1190/1.1442197.

Cordell L., Henderson R. G., 1968: Iterative three-dimensional solution of gravity anomaly data using a digital computer. Geophysics, **33**, 4, 596–601, doi: 10.1190/1.1439955.

Garland G. D.,l970: The earth's shape and gravity. Pergamon Press, 183 p.

Geldart L. P., Gill D. E., Sharma B.,1966: Gravity anomalies of two-dimensional faults. Geophysics, **31**, 2, 372–397, doi: 10.1190/1.1439781.

Gendzwill D. J., l970: The gradational density contrast as a gravity interpretation model. Geophysics, **35**, 2, 270–278, doi: 10.1190/1.1440090.

Grant F. S., West G. F., l965: Interpretation theory in applied geophysics. McGraw-Hill Book Co.

Gupta O. P., l983: A least-squares approach to depth determination from gravity data. Geophysics, **48**, 3, 357–360, doi: 10.1190/1.1441473.

Hammer S., l977: Graticule spacing versus depth discrimination in gravity interpretation. Geophysics, **42**, 1, 60–65, doi: 10.1190/1.1440714.

Klingelé E. E., Marson I., Kahle H.-G., 1991: Automatic interpretation of gravity gradimetric data in two dimensions: vertical gradient. Geophys. Prospect., **39**, 3, 407–434, doi: 10.1111/j.1365-2478.1991.tb00319.x.

Levy D., 2010: Introduction to numerical analysis. Maryland: Center for ScientificComputation and Mathematical Modeling, University of Maryland, p. 121.

Lomnitz C., l959: Gravimetric investigations in the Chillán region (Investigaciones gravimétricas en la región de Chillán). Boletín (Instituto de Investigaciones Geológicas (Chile)), **4**, Santiago de Chile, 19 p. (in Spanish).

Mathworks, 2018: MATLAB. http://mathworks.com/products/matlab/, accessed 27 February 2018.

Naidu P. S., Mathew M. P., 1998 : Analysis of geophysical potential fields, A digital signal processing approach. Advances in Exploration Geophysics, **5**, Elsevier Science, 8–9, eBook ISBN: 9780080527123, 297 p.

Nettleton L. L., 1942: Gravity and magnetic calculations. Geophysics, **7**, 3, 293–310, doi: 10.1190/1.1445015.

Parasins D. S., l973: Mining geophysics. Elsveier Scientific Publishing Co., ISBN: 9780444 601858.

Sharma B., Vyas M. P., 1970: Gravity anomalies of a fault cutting a series of beds. Geophysics, **35**, 4, 708–712, doi: 10.1190/1.1440124.

Talwani M., Worzel J. L., Landisman M., 1959: Rapid gravity computations for two-dimensional bodies with applications to the Mendocino submarine fracture zone. J. Geophys. Res., **64**, 1, 49–59, doi: 10.1029/JZ064i001p00049.

Tanner J. G., 1967: An automated method of gravity interpretation. Geophys. J. R. Astron. Soc., **13**, 1-3, 339–347, doi: 10.1111/j.1365-246X.1967.tb02164.x.

Telford W. M., Geldart L. P., Sheriff R. E., Key D. A., 1976: Applied Geophysics. Cambridge Univ. Press, London.

sciendo

Contributions to Geophysics and Geodesy Vol. 49/3, 2019 (249–263)

Understanding the hydrocarbon prospect of Buzdar block, Southern Indus basin, Pakistan, by using 2-D seismic data: A case study

Hamid HUSSAIN[1,*], Zhang SHUANGXI[1,2,3], Muhammad ABID[4]

[1] Department of Geophysics, School of Geodesy and Geomatics, Wuhan University, Wuhan, Hubei, 430079, P.R. China

[2] Key Laboratory of Geospace Environment and Geodesy of Ministry of Education, Wuhan University, Wuhan, Hubei, 430079,P.R. China

[3] Collaborative Innovation Center of Geospace Information Science, Wuhan University, Wuhan, Hubei, 430079, P.R. China

[4] School of Ocean and Earth Science Tongji University, Shanghai, P.R. China

Abstract: The sub-surface structural analysis to understand the geology and tectonics of an area is always useful to locate the hydrocarbon resources. Oil and gas based energy supplies have become a vital source for Pakistan, which is passing through an era of severe energy crisis. The study area, Buzdar block, in the southern Indus Basin is tectonically an extensional regime and is expected to have a huge hydrocarbon potential. In this study, we did the interpretation of the migrated seismic lines of the 872-SGR-527, 872-SGR-529, 872-SGR-531, 872-SGR-532 of Buzdar block, District TandoAllahyar, Sindh. The lines 872-SGR-529, 872-SGR-531, 872-SGR-532 were oriented W–E whereas the line 872-SGR-527 was oriented NW–SE. The obtained data was analysed and three reflectors were marked named top Khadro Formation, top lower Goru formation and top Chiltan limestone (probable). Through this study faults have been also marked on seismic lines which are normal faults by nature; collectively form horsts and grabens which is the evidence of effect of extensional tectonics in the area. Time contour maps were also generated. After that, time was converted into depth with the help of well velocity from VSP data for lower Goru formation and average velocity for Chiltan limestone (probable) from regression analysis. Finally, depth contour maps were generated which helped to know the basic mechanism of tectonic movement in the area. On the basis of present analysis we propose that a well may be drilled at Lower Goru formation near fault F1 on western side at a depth of 1370 meters and at 1290 meters near fault F4 on eastern side.

Key words: Buzdar block, 2-D seismic data, time-depth analysis, probable well location, hydrocarbon potential

*corresponding author: e-mail: hamidhussain@whu.edu.cn

doi: 10.2478/congeo-2019-0013

1. Introduction

Geographically, Buzdar block is located in district Tando Allah yar at a location between Mirpurkhas and Hyderabad. Previously this block was known as Sanghar south. The study area lies between 25°15′00″ N to 25°26′00″ N and 68°40′00″ E to 68°48′00″ E. Geologically the area falls in Southern Indus Basin as shown in Fig. 1 (*Kazmi and Rana, 1982*).

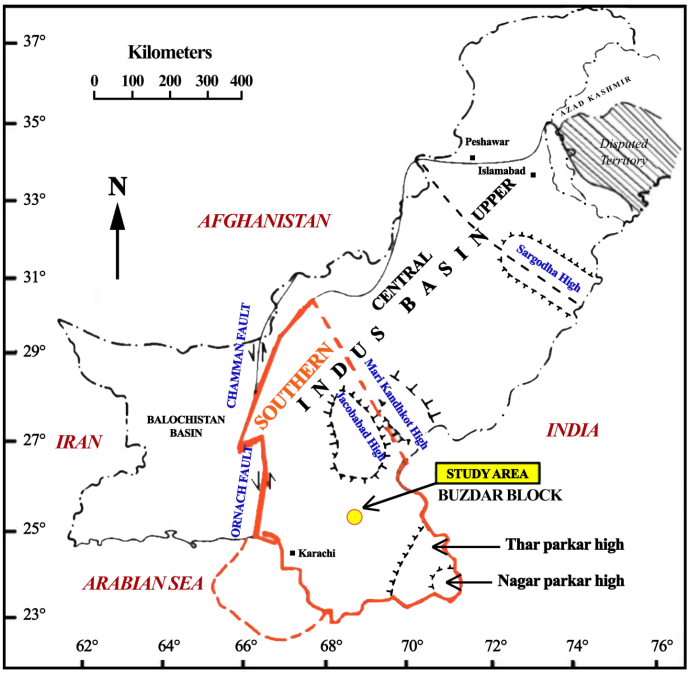

Fig. 1. Location map of the study area (modified *Kazmi and Rana, 1982*).

1.1. Tectonics

Pakistan is divided into three basins upper Indus basin, central Indus basin and southern Indus basin (*Wandrey et al., 2004*). The area under study in southern Indus basin exhibits extensional tectonics and as a consequence, normal faults are generated showing horst and graben structure. The southern Indus basin (550 × 250 km) is characterized by tectonic up warping on the western margin of the Indo-Pakistan subcontinent (i.e. the eastern part

of Pakistan). The southern Indus basin, is characterized by several structural highs (Sibi, Jaccobabad, Khairpur, Mari-Khandkot and Hyderabad) (*Zaigham and Mallick, 2000*).

The proposed geological models also illustrate the potential for appropriate environments for development of hydrocarbon source rocks, sufficient heat for thermal maturity and structures for reservoirs and seals, suggesting more bright prospects in the southern Indus basin (*Zaigham and Mallick, 2000*). The southern Indus basin is located just south of Sukkur Rift – a divide between Central and Southern Indus basins and is bounded by the Indian Shield – to the east and the marginal zone of Indian plate to the west. Its southward extension is confined by off-shore Murray Ridge-Oven Fracture plate boundary (*Kadri, 1995*).

1.2. Stratigraphy and Petroleum play

The stratigraphic property of the study area is shown in Table 1. The southern Indus basin is a broad north-south–trending sedimentary basin having thick Tertiary sequences underlain by Mesozoic rocks and overlain by Quaternary sediments. The sedimentary section of Lower Indus Basin in the South Eastern Pakistan starts from rocks ranging from Triassic age upto recent age (*Kazmi and Jan, 1997*). Stratigraphically, the shale series of the Early Cretaceous Sember Formation and the Lower Goru Formation are the main documented oil and gas source rock units in the southern Indus basin (*Hussain et al., 1991*). Upper Paleocene marine transgressive shales are the secondary source rock series, deeply buried in the western half of the southern Indus basin (*Zaigham and Mallick, 2000*). In the southern Indus basin, the main oil and gas productive reservoir rock units are the Cretaceous Lower Goru sandstones. The basal transgressive sandstones of the Early Cretaceous Sember Formation may be important hydrocarbon targets. Moreover, hydrocarbon targets may also exist in the Jurassic Chiltan Limestone, Paleocene, and Eocene formations. The upper Goru shales are the main reservoir seal in the southern Indus basin. The intra-formational shales of the lower Goru provide regional seal for all of the sand units of the lower Goru formation. Hydrocarbon accumulations in the area are generally confined to the horst and tilted fault block structures. The upper Goru, which drapes over these structures, forms the top and lateral seals for the

Table 1. Stratigraphy of the study area (modified after *Kazmi and Jan, 1997*).

ERA	PERIOD	EPOCH		FORMATION		DESCRIPTION
CENOZOIC	QUARTERNARY	HOLOCENE		ALLUVIUM		Sandstone, clay, shale and conglomerate
	TERTIARY	PLIOCENE-PLEISTOCENE		SIWALIK GROUP		Sandstone, Shale and conglomerate
		MIOCENE		GAJ		Shale, sandstone and limestone
		OLIGOCENE		NARI		Shale, limestone and sandstone
		EOCENE	LATE			
			MIDDLE	KIRTHAR		Shale and limestone
			EARLY	LAKI/GHAZIJ		Laki: Limestone and Shale Ghazij: Shale and sandstone
		PALEOCENE		BARA-LAKHRA		Limestone, shale and sandstone
				KHADRO		Sandstone, basalt and shale
MESOZOIC	CRETACEOUS	LATE		PAB		Sandstone and shale
				MUGHAL KOT		Limestone, shale and minor sand
				PARH		Limestone
		MIDDLE		GORU	UPPER	MAIN SEAL Shale and marl
					LOWER	Sandstone and shale
		EARLY		SEMBAR		MAIN SOURCE Sandstone and shale
	JURASSIC	LATE				
		MIDDLE		CHILTAN/ MAZARDRIK		Chiltan: Limestone MazarDrik: Shale and sandstone
		EARLY		SHIRINAB		Limestone, shale and sandstone
	TRIASSIC	EARLY-LATE		WULGAI		Sandstone and shale

upper sand units of lower Goru formation and also acts as cross-fault seals. The interbedded shale units within the lower Goru formation provide seals for the deeper reservoirs. In general, the transgressive shales of the Cretaceous (Sember Formation) and Tertiary (Bara-Lakhra, Laki-Ghazij, and Kirthar Formations) provide seals to Jurassic and Tertiary reservoirs respectively. The oldest rocks encountered in the area are of Triassic age (Jhat pat and Nabisar wells). Central and Southern Indus basins were undivided until Lower/Middle Cretaceous when Khairpur-Jacobabad High became a prominent positive feature. This is indicated by homogenous lithologies of Chiltan Limestone (Jurassic) and Sembar Formation (Lower Cretaceous) across the High (*Kadri, 1995*).

2. Materials and Methods

Two main approaches for the interpretation of seismic data are adopted; first one is stratigraphic analysis while the other is structural analysis. Stratigraphic analysis involves the subdivision of seismic sections into sequence of reflections that are interpreted as seismic expression of genetically related sedimentary sequences. Application of structural analysis is the search for different structural styles within the subsurface. Seismic stratigraphic analysis is the delineation of individual seismic facies units (*Al-Sadi, 1980; Badley, 1985; Lines and Newrick, 2004*).

Seismic reflection data consist of four lines along with two wells (as shown in Fig. 2) acquired with the special permission from Directorate General of Petroleum Concession (DGPC) and are used for the interpretation of subsurface structures, stratigraphy and depth of basement.

A) seismic data:
- 972-SGR-529 (Strike line)
- 872-SGR-527 (Dip line)
- 872-SGR-532 (Dip line)
- 872-SGR-531 (Dip line)

B) well data:
- Buzdar-01
- Buzdar North-1.

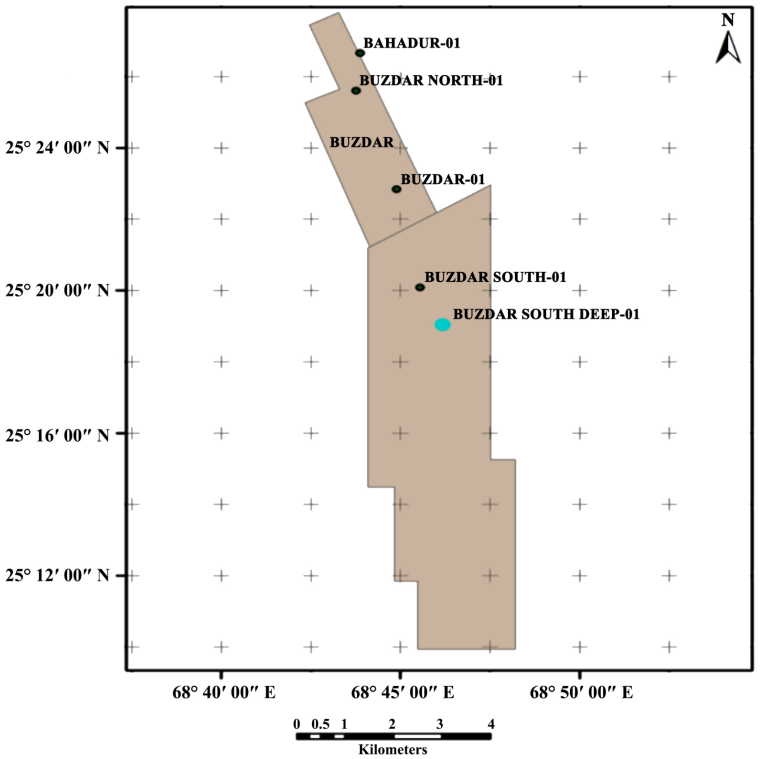

Fig. 2. Block diagram showing the location of wells (Buzdar Block).

Seismic data Interpretation:

One of the initial important things for an interpreter of seismic data is the picking or interpretation of reflectors of horizons. Base map was prepared which typically includes locations of lease or concession boundaries, wells and seismic survey points with geographic references such as latitude and longitude or Universal Transverse Mercator (UTM) grid information.

The Seismic data lines 972-SGR-529 (Strike line), 872-SGR-527 (Dip line), 872-SGR-532 (Dip line), 872-SGR-531 (Dip line) are interpreted by solving velocity windows panels to obtain the average velocity (Figs. 3–6). The LAS files of wells Buzdar-01, Buzdar North-1 and seismic lines were manipulated for calculating the corresponding depth, interval velocity, one way travel time (OWT), two ways travel time (TWT) and average velocity.

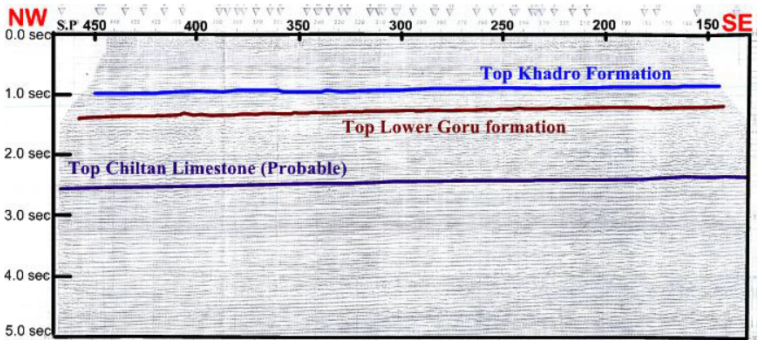

Fig. 3. Interpreted seismic section of seismic line 872-SGR–527.

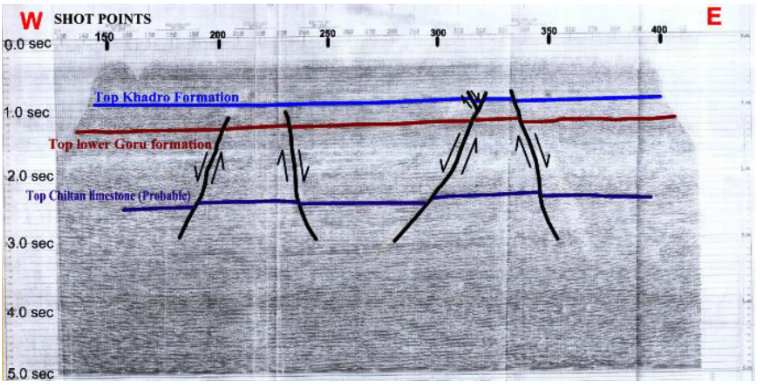

Fig. 4. Interpreted seismic section of seismic line 872-SGR–529.

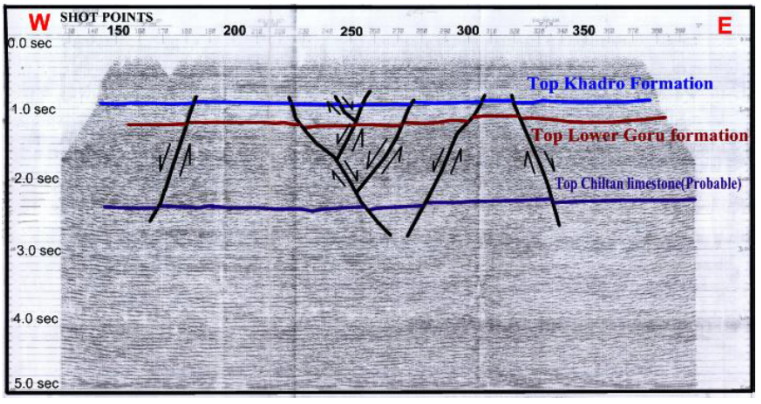

Fig. 5. Interpreted seismic section of seismic line 872-SGR–531.

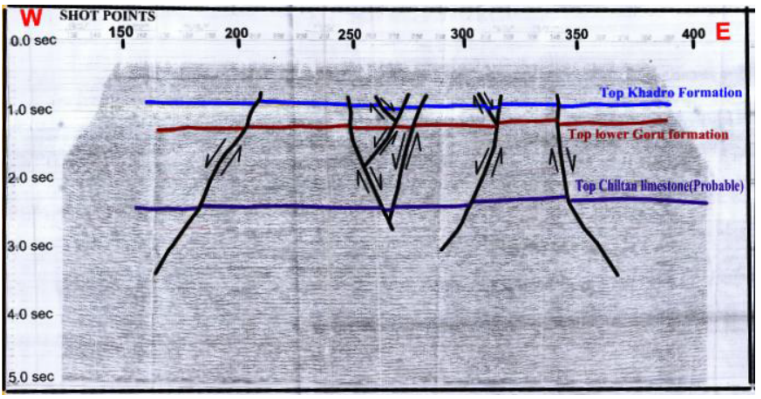

Fig. 6. Interpreted seismic section of seismic line 872-SGR–532.

Velocity windows were solved given on the seismic section to find the average velocity by using the Dix Equation as shown by *Cameron et al. (2008)*.

$$V_{\text{ave},n} = \frac{[(V_{\text{int},n} \cdot (T_n - T_{n-1})) + (V_{\text{ave},n-1} \cdot T_{n-1})]}{T_n}\,, \tag{1}$$

where V_{ave} is the average velocity, T is the two way travel time, and V_{int} is the interval velocity.

On strike line 872-SGR-527 all the three velocities i.e. root mean square velocity, interval velocity and average velocity were given so there was no need to solve the velocity windows to find average velocity.

On the dip lines 872-SGR-529, 872-SGR-531 and 872-SGR-532 only root mean square velocity and interval velocity were given which were transferred into MS Excel worksheet where we utilized them for further working to find out the average velocities (V_{ave}) by using the formula.

Regression analysis is a statistical technique which was used to find the RMS velocity at the times on which we picked our reflector. Regression analysis was used which utilizes the Root Mean Square (rms) velocity and the two way travel time from the velocity windows of the seismic section. In regression analysis we used the velocity windows of the seismic section saved in the MS Excel worksheets to generate a two way travel time vs. RMS velocity graph. Then a best fit line is passed through the graph, which gave us the equation of straight line:

$$y = mx + c\,, \tag{2}$$

where y = RMS velocity, m = slope, x = two way travel time, c = intercept (constant).

Time to depth conversion is necessary because we need to make the depth contour map of the horizon which shows the place of the horizon in subsurface depth wise. These maps are vital to seismic interpretation, as they tell us the physical place of the horizons.

As velocity is required to convert the time into depths; so we got the velocity from well data of Buzdar-01 and Buzdar North-01 for lower Goru formation. While for Chiltan Limestone we used the average velocity calculated from the regression analysis because the wells were not drilled upto Chiltan Limestone. For depth conversion following formula was used:

$$S = V \cdot T/2\,, \tag{3}$$

where, S = depth of the reflector, V = well velocity or average velocity calculated by regression analysis, T = two-way time of the reflector read from the seismic section but here we have taken it as $T/2$ i.e. one way travel time in order to get the depth.

3. Results and Analysis

Following are the graphs got after regression analysis of the lines to get the equation of straight line for finding the RMS velocity. This equation was to find the RMS velocity against the two way time noted for Chiltan limestone and we also calculated the interval and average velocities against those times. This average velocity is required for time to depth conversion. We did not use this procedure to find RMS velocity and then average velocity for top lower Goru formation because we got the well velocity from the VSP data summary sheet of Buzdar-01 and Buzdar North-01 which was utilized in time to depth conversion. The results of regression analysis are shown in Fig. 7.

In order to calculate the depth for lower Goru formation we used the well velocity $V = 2324.5$ m/sec; while for the Chiltan Limestone we have used a mean average velocity calculated from average of four lines regression analysis, namely $V = 3275.7$ m/sec. The depth values of both the reflectors, i.e. lower Goru formation and Chiltan Limestone were used to generate the depth contour map of lower Goru formation and Chiltan Limestone.

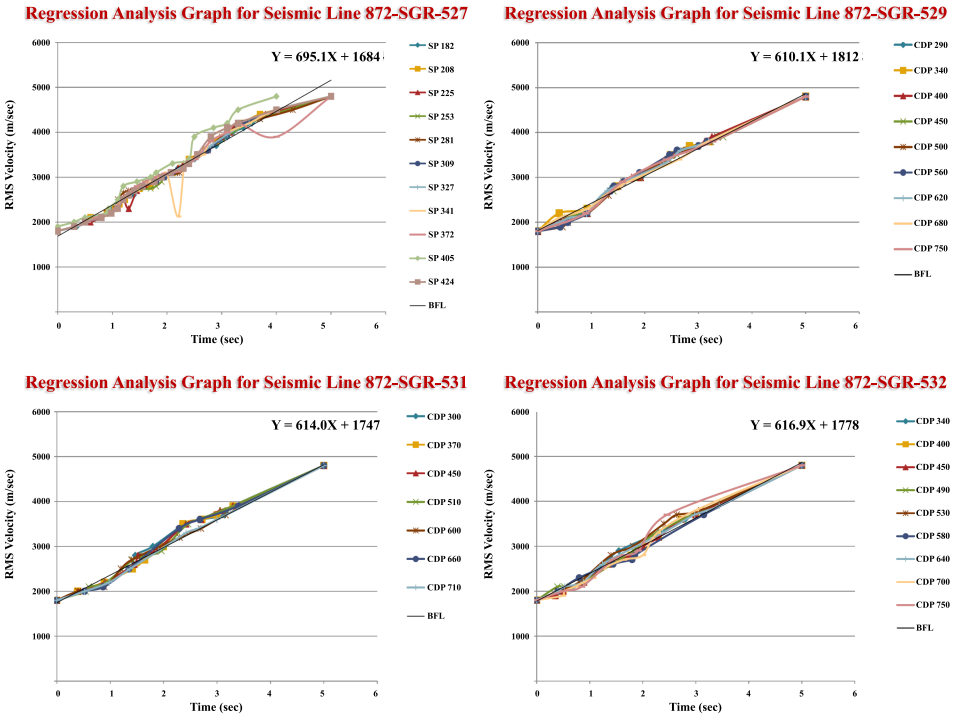

Fig. 7. Results of regression analysis.

Depth of Top lower Goru formation is varying from 1278 meters to 1592 meters while depth of Chiltan Limestone is varying from 3668 meters to 4353 meters. The depth of top lower Goru formation and Chiltan Limestone is decreasing as we move from south to north. Time & Depth contour maps show possible leads (highs) on top lower Goru formation near fault F4 on east side (due to which two wells Buzdar North-01 and Buzdar-01 had been drilled). Time & Depth contour maps also show possible leads (highs) on top lower Goru formation near fault F1 on west side. Time and depth contour maps of Chiltan Limestone also show possible lead (high) near fault F4 on eastern side. The traps have three ways dip closure bounded on one side by a fault. The vertical relief of the closure at top lower Goru formation is 50 milliseconds (40 meters) and Chiltan Limestone is 40 milliseconds (50 meters). As the data quality is poor so it is recommended that the data should be reprocessed. For more detailed study and to define potential sites

in the area, more seismic lines are required. 3D survey may be performed in order to get a detailed subsurface picture of the Buzdar block.

TWT contour map at top lower Goru formation was generated with a contour interval of 10 milli seconds. Lower Goru was cut by faults at four locations. This cutting by faults made horst and graben structures along the formation. The contour map showed two highs in the formation shown in Fig. 8. TWT contour map at top Chiltan Limestone was generated with a contour interval of 10 milli seconds. Chiltan Limestone was cut by faults at four locations. This cutting by faults made horst and graben structures along the formation. The contour map shows one high in the formation (Fig. 9). Depth contour map at top lower Goru formation was generated with a contour interval of 10 meters.The formation shows two important highs which can be possible horst blocks and potential leads. One is located at the eastern side along the dip line 872-SGR-531 at a depth of 1270 m. The second lead is located on the western side along the dip line 872-SGR-531 at a depth of 1370 m (Fig. 10). It is being proved by the depth contour map at lower Goru formation that the depth is increasing while we move from south to north as it is shown by the correlation of depths at top lower Goru formation in the 3 wells present in Buzdar block (Fig. 12). Depth contour map at top Chiltan Limestone was generated with a contour interval of 10 meters. The formation shows one important high located on the eastern side along the dip line 872-SGR-531 near fault F4 at a depth of 3730 m which can be possible horst block and potential lead (Fig. 11).

It is being proved by the depth contour map at lower Goru formation that the depth is increasing while we move from south to north as it is shown by the correlation of depths at top lower Goru formation in the 3 wells present in Buzdar block.

4. Conclusions and Recommendations

The area is an extensional regime, due to which there are normal faults and horst and grabenstructures.The trend of the faults is NW–SE. The throw of the faults at top lower Goru formation level is 25 to 30 milliseconds while at Chiltan Limestone level it is 30 to 35 milliseconds. The Average velocity of Chiltan Limestone calculated by regression analysis is 3275.7 m/sec.

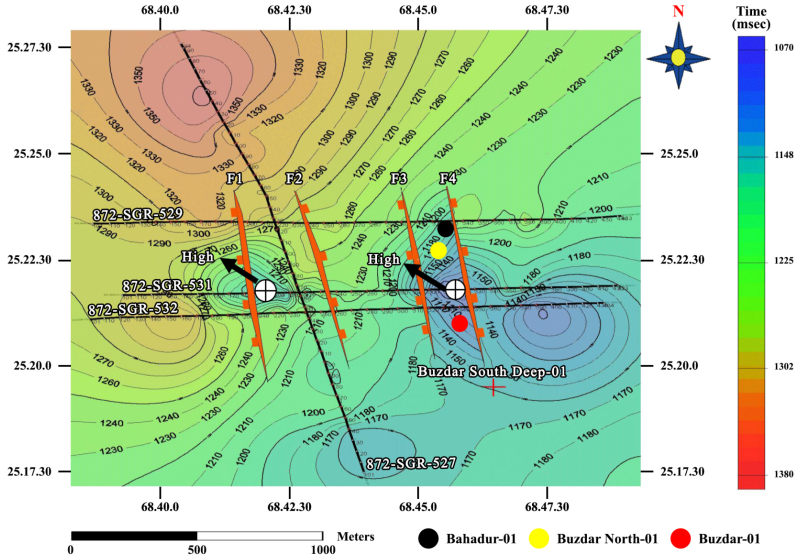

Fig. 8. Two way time contour map at Top lower Goru formation.

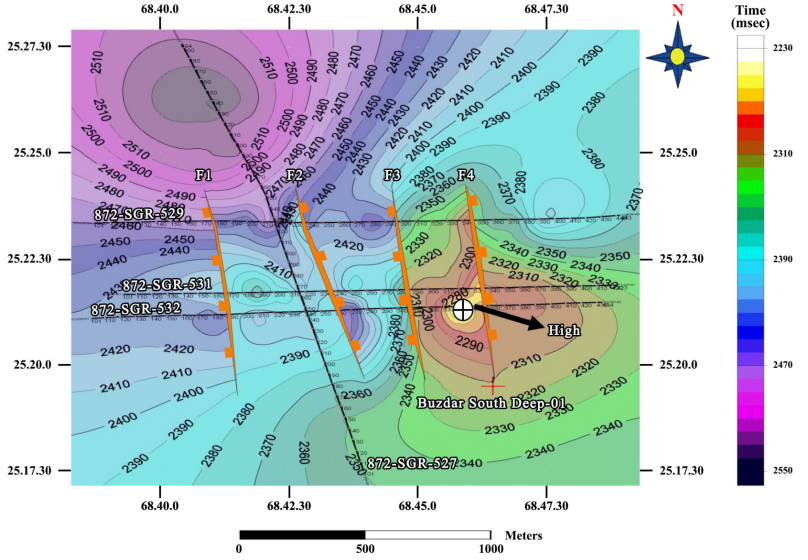

Fig. 9. Two way time contour map at top Chiltan Limestone (probable).

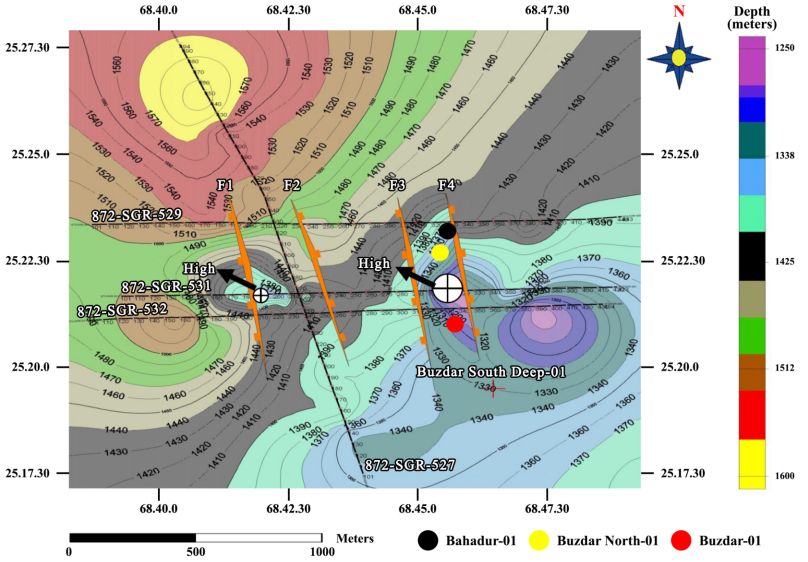

Fig. 10. Depth contour map at top lower Goru formation.

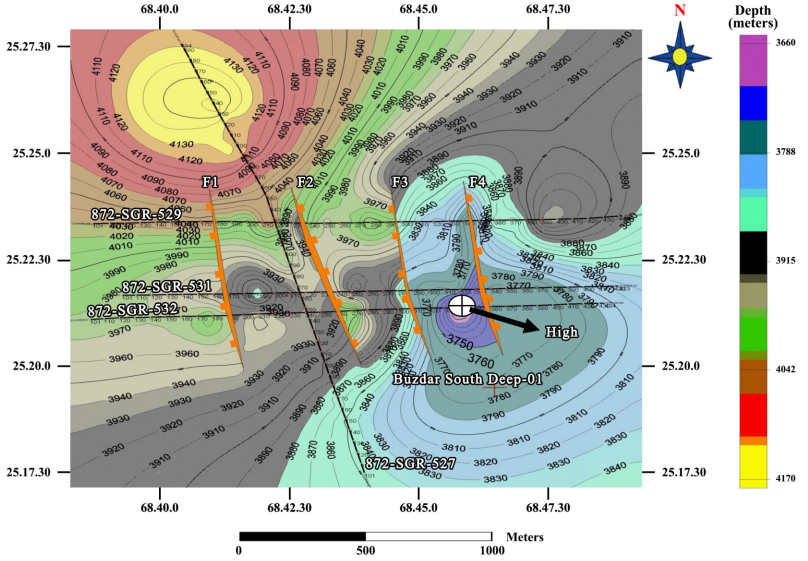

Fig. 11. Depth contour map at top Chiltan Limestone (probable).

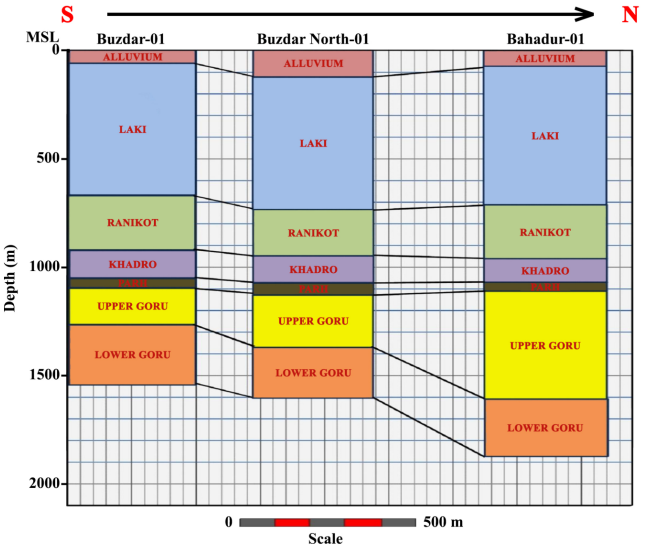

Fig. 12. Depth correlation at top lower Goru formation in 3 wells of Buzdar block.

Well may be drilled at Lower Goru formation near fault F1 on western side at a depth of 1370 meters and at 1290 meters near fault F4 on eastern side.

Detailed studies of petrophysical properties of Chiltan Limestone may be performed in the surrounding concessions located in Thar platform, if the results show reservoir potential of Chiltan Limestone then Buzdar North-01 and Buzdar-01 well may be drilled deeper upto Chiltan Limestone.

Acknowledgements. This study is supported by the NSFC (No. 41174021, No. 41474093) and China's International Education Funding for Chinese-Pakistani students.

References

Al-Sadi H. N., 1980: Seismic Exploration: Technique and Processing. Birkhäuser-Verlag, Boston, 211 p.

Badley M., 1985: Practical Seismic Interpretation. IHRDC publishers Boston, 266 p.

Cameron M., Fomell S., Sethian J., 2008: Time-to-depth conversion and seismic velocity estimation using time migration velocity. Geophysics, **73**, 5, VE205–VE210, doi: 10.1190/1.2967501.

Hussain M., Getz S. L., Oliver R., 1991: Hydrocarbon accumulation parameters in the central portion of the lower Indus of Pakistan. In: Ahmed G., Kamal A., Zaman A. S. H., Humayon M., (Eds.): Proceedings of international petroleum seminar on new directions and strategies for accelerating petroleum exploration and production in Pakistan, Islamabad Nov. 22-24, 13 p.

Kadri I. B., 1995: Petroleum geology of Pakistan. Pakistan Petroleum Ltd., Karachi, 275 p.

Kazmi A. H., Jan Q. M., 1997: Stratigraphic setting. In: Geology and Tectonics of Pakistan, Graphic Publishers Karachi, Pakistan.

Kazmi A. H., Rana R. A., 1982: Tectonic map of Pakistan, scale of 1:2,000,000. Geological Survey of Pakistan, 1 sheet.

Lines L. R., Newrick R. T., 2004: Fundamentals of Geophysical Interpretation. Society of Exploration Geophysicists, 289 p.

Wandrey C. J., Law B. E., Shah H. A., 2004: Sembar Goru/Ghazij Composite Total Petroleum System, Indus and Sulaiman-Kirthar Geologic Provinces, Pakistan and India. U.S. Geological Survey Bulletin 2208-C, available online: `https://pubs.usgs.gov/bul/2208/C/b2208-c.pdf`.

Zaigham N. A., Mallick K. A., 2000: Prospect of hydrocarbon associated with fossil-rift structures of the southern Indus basin, Pakistan. Am. Assoc. Pet. Geol. Bull., **84**, 11, 1833–1848, `doi: 10.1306/8626C3A7-173B-11D7-8645000102C1865D`.

sciendo

Contributions to Geophysics and Geodesy Vol. 49/3, 2019 (265–281)

The seismicity of central and north-east Himalayan region

Susheel KUMAR[1], Nitin SHARMA[1,2,*]

[1] Indian Institute of Geomagnetism, Navi Mumbai 410218, India

[2] CSIR – National Geophysical Research Institute, Hyderabad 500007, India

Abstract: The Himalayan range extends upto 2400 km arc from Indus river valley in the west to Brahmaputra river valley in the east of India. Due to distinct geological structures of Himalayan seismic belt, seismicity in Himalaya is inhomogeneous. The inhomogeneity in seismicity is responsible for a number of seismic gaps in the Himalayan seismic belt. Thus Iin the present study, we proposed the study of spatial and temporal evolution of seismicity in entire central and north-east Himalayan region by using Gutenberg-Richter relationship. A detailed study on the behavior of natural seismicity in and around the seismic gap regions is carried out. The study region is segmented in four meridional regions (A) 80°E to 83.5°E, (B) 83.5°E to 87.5°E, (C) 87.5°E to 90°E and (D) 90°E to 98°E along with a fixed latitude belt. The homogeneous catalogue with $3 \leq M_b \leq 6.5$ is used for the spatial and temporal analysis of seismicity in terms of b-value. It is find out that pockets of lower b-values are coinciding over and around stress accumulated regions. The observed low b-value before occurrence of the Nepal earthquake of 25th April, 2015 supports the argument of impending occurrence of moderate to large magnitude earthquake in Sikkim and north-east Himalayan region in future.

Key words: central and north-east Himalaya, natural seismicity, Gutenberg-Richter relationship, b-value

1. Introduction

The central and north-east Himalayan regions are prone to medium and large magnitude earthquakes. The Kangra earthquake of 1905 (M_s 8.0), Nepal (Bihar) earthquake of 1934 (M_w 8.4), Assam earthquake of 1950 (M_w 8.3), Kashmir earthquake of 2005 (M_w 7.8) and Gorkha, Nepal earthquake of 25th April, 2015 (M_w 7.8), etc. are some examples in this context. The collision of a fast moving Indian continental plate ($\sim$45 mm/year) with the slow Eurasian plate ($\sim$2–3 mm/year) resulted in the formation of the

*corresponding author: e-mail: withnitin@gmail.com

doi: 10.2478/congeo-2019-0014

Himalayas and the attendant seismic belt. This belt currently consists of the Himalayan mountain ranges, Tibet plateau and other highest mountain ranges including the Everest (e.g. *Gansser, 1964; Valdia, 1976*). The first collision between the Indian and Eurasian plates invoked the main central thrust (*Zhao et al., 1993*) (MCT) fault before $\sim$23 Ma and it was active for $\sim$12 Ma. In the process of continuous convergence, the main boundary thrust (MBT) fault was formed before $\sim$11 Ma and was active up to $\sim$3 Ma. The Main frontal thrust (MFT) fault was formed further south of MBT before $\sim$2 Ma and is still active (*Avouac, 2003*). The convergence of the Indian plate across the MFT fault is $\sim$20 mm/year (e.g. *Ader et al., 2012* and references therein). The time evolution of these faults depicts that seismicity has migrated southwards (*Yeats and Thakur, 1998*) in the last $\sim$30 Ma.

The studies like *Thakur (2004)* and *Mukhopadhyay (2011)* have claimed that some geological portions of the region between the MCT and the Suture zone (Indian and Eurasian plate) are reactivated to yield the observed seismicity of this region. The most devastating earthquakes of India occurred near the MBT and MFT regions during last 125 years. This corroborates that these two faults are still active from seismicity point of view. All the three main faults (MCT, MBT and MFT) terminate at the low dipping (5°–16°) plane of detachment or a common mid-crustal decollement known as the main Himalayan thrust (MHT) (*Molnar and Lyon-Ceant, 1989; Schelling and Arita, 1991; Sapkota et al., 2013*). The earthquake sources rupture and propagate southwards along the plane of detachment, MHT (*Sapkota et al., 2013; Sreejith et al., 2016*). Most of the thrust fault motion (*Fitch, 1970; Zhao and Helmberger, 1991*) consists of slip on the main Himalayan thrust (MHT) fault which is a shallow dipping (5°–16°) mid-crustal ramp structure (*Pandey et al., 1995, 1999; Cattin and Avouac, 2000; Caldwell et al., 2013, Sreejith et al., 2016*). It can be seen from the seismological catalogue (*Ni and Barazangi, 1984; Kayal, 2001, 2010*) that most of the decollement earthquakes occur in the depth range $\sim$11–20 km (i.e. within upper crust) which coincides with MHT in the southern Himalaya. While, the MFT is the main surficial visualisation of crustal shortening between the Himalaya and the Indian plate (*Sapkota et al., 2013*).

The natural seismicity of any continental-continental collision zone can be classified as pre-seismic, co/inter-seismic and post-seismic cycles (*Bilham*

et al., 1997 and *Cattin and Avouac, 2000; Avouac, 2003; Jade et al., 2007; Mukul et al., 2010; Jade et al., 2014*). It is generally difficult to demarcate temporal boundaries between these cycles. The advent of digital instrumentation and improved networks World-Wide Standardized Seismological Network (WWSSN) standards under the U.S. Geological Survey (USGS) collaboration) resulted in accurate catalogue data (*Bhattacharya and Dattatrayam, 2000*). It is now possible to identify prolongation of a cycle based on precise information of the current and past cycles. It should be noted here that the nature of these cycles depends on the fault parameters, tectonic slip or locking, geographic and climatic conditions, geological heterogeneity and stress barriers. We attempt to study the nature of the impending seismicity associated with these cycles using the information available from the current and past seismic behaviour of the central and north-eastern Himalayan regions (80°E to 98°E in four meridional regions – Fig. 1).

As the main thrust faults lie in the latitude belt of $\sim$26°N to 30°N, we thus restrict the current study bounded by the above said latitude and longitude intervals. Fig. 1 depicts the selected study area which is again divided into four different longitude sub-regions: (A) 80°E to 83.5°E – Western Nepal region, (B) 83.5°E to 87.5°E – Central Nepal region, (C) 87.5°E to 90°E – Eastern Nepal and Sikkim region and (D) 90°E to 98°E – Bhutan, Assam and Arunachal Pradesh region. These longitudinal bins are made on the basis of disposition of the tectonic and geological structures in the studied region (*Adhikari and Paudyal, 2015*) which indicates scattered seismicity confined to northern part of MCT in western part of Nepal to north-west of Himalayan in India and MBT to MFT in central to eastern part of Nepal. The significantly low seismicity with time is observed in crustal homogeneity and various barriers e.g. faults/ridges/rifts area of Central Nepal (Fig. 1). The segmented A, B, C and D bins shown in Fig. 1 also depict the main tectonic features such as prominent ridges and grabens, important lateral strike-slip and thrust faults, besides other lineaments that lay in the selected study sub-regions. It is to be mentioned that the above said four regions are chosen to exclusively consider the seismicity of the continental-continental collision margins and effective stress/strain rate. The four subdivision are done to analyse the spatio-temporal variations of b-value precisely. Moreover each sub-region comprises seismic gaps (central seismic gap and distinct tectonic features such as fault friction and geometry which might affect the

behaviour of the seismicity and magnitude of earthquake in sub-regions as mentioned in previous studies (*Bilham et al., 2001; Dal Zilio et al., 2019*).

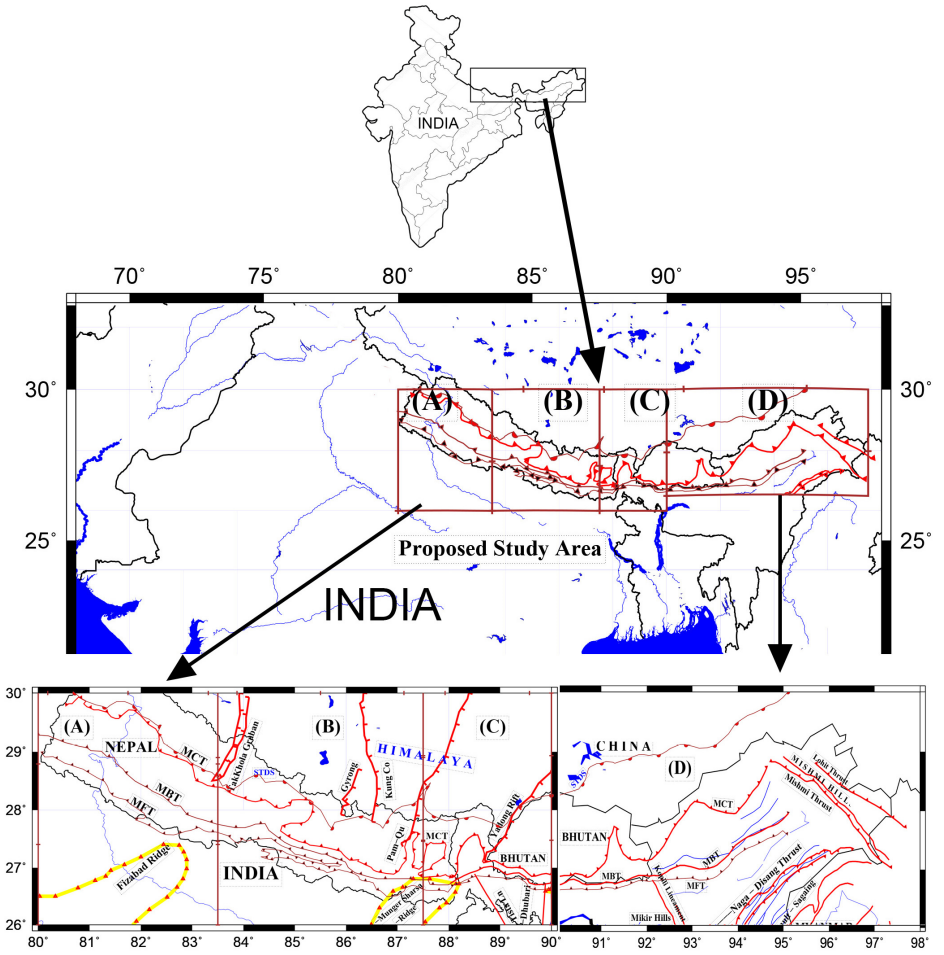

Fig. 1. Segmentations of study area are marked on basis of tectonics as regions A,B,C and D (marked rectangular blocks). STDS (South Tibetan Detachment), MFT is marked half circle and triangles on brown lines. The MBT, MCT major thrust faults marked with triangles on red line and other faults are shown in red lines. Ridges are marked with yellow lines with red triangles. Graban and rift in northern part are shown as red line with tick marks.

The objectives of the present study are to document spatial and temporal changes in frequency-magnitude distribution (FMD) related to the demarcated regions and their association with earthquake occurrence of a certain threshold magnitude (*Pudi et al., 2018; Dal Zilio et al., 2019*). Based on the characteristic features in the seismic rates, specific to the thrust regions of central and north-eastern Himalaya, we attempt to identify the most probable locations of impending earthquakes in tectonically active region associated with spatial b-value < 1.0.

The well-known Gutenberg-Richer law (*Ishimoto and Iida, 1939; Gutenberg and Richer, 1954, 1944*) thus forms the main foundation to the present study. This relation can be formulated as:

$$\log N = a - bM\,. \tag{1}$$

In Eq. (1) a and b are constants, b-value (slope of frequency-magnitude distribution (FMD)) represents tlogarithmic ratio of the number of earthquakes (N) with magnitude of earthquakes (M) while a-value represents the overall seismicity. Various studies have used this equation to depict that, in a stressed region, if the number of small magnitude earthquakes are high then the possibility of occurrence of a large magnitude earthquake will be less. A low b-value indicates that the effective stress in the boundaries of rocks is still in an accumulation phase, and is likely to be released at any point of time by way of a large earthquake or total equivalent energy in multiple moderate size events. While, a high b-value suggests that the regional heterogeneity or crack density is high and is transforming into a low stressed regime (*Wyss, 1973; Tsapanos, 1990; Nuannin et al., 2005; Parsons, 2007*). The spatial and temporal variations of b-value can be used to understand the physical behaviour of stress or strain rate in the tectonically characteristic of theactive region. The high spatial variation of b-value is a meter to say that stress, has already normalized the differential stress. Therefore, the b-value serves as the main parameter in the present study. The studies based on similar concepts have shown promising results for e.g. studies carried out in Taiwan, by *Chan et al. (2012)* and *Prasad and Singh (2015)* in Andaman subduction region, *Pudi et al. (2018)* in western India to central Nepal, *Sreejith, et al. (2016)*; *Sreejith et al. (2018)* Gorkha earthquake (M_b 6.9, M_w 7.6 ISC) in central Nepal region of Nepal.

2. Data and Methodology

The availability of large data is a basic requirement for any systematic scientific study. We use the homogeneous earthquake catalogue of USGS, ISC and ANSS(Advanced National Seismic System), with only body wave magnitude scales ranges from 3 M_b to 6.9 M_b. Though, catalogues are available from 1950 onwards, but public data continuity and accuracy in M_b were observed better after 1974 in the study region (*Bhattacharya and Dattatrayam, 2000*).

To compute b-value, self-similarity of earthquake process which consequently implies a power law in the distribution of earthquakes in terms of magnitude is assumed. An estimate of reasonably accurate b-values can be obtained using equation given below (*Aki, 1965; Bender, 1983; Utsu 1999*):

$$b = \frac{\log_{10} \mathrm{e}}{\langle M \rangle - \left(M_c - \dfrac{\Delta M_{bin}}{2} \right)}, \tag{2}$$

where $\langle M \rangle$ = mean magnitude, M_c = magnitude of completeness, ΔM_{bin} = binning width of magnitude of completeness, i.e. 0.1 or 0.2.

M_c, completeness of Catalogue, is more crucial in b-value study and an important parameter. The high value of M_c will represent to under sampling of events, while low value of M_c will represent erroneous seismicity. The M_c value is computed by normalisation of the ratio between the frequency of earthquake and magnitude of earthquake (*Rydelek and Sack, 1989*). To calculate it we used the Entire Magnitude Range (EMR) method (*Woessner and Wiemer, 2005*, further modified after *Ogata and Katsura, 1993*). In order to maintain the self-similarity of the catalogues for all the regions, we therefore discarded the smaller magnitude earthquakes of $M_b < 3$. Thus body wave magnitude ($3 \geq M_b \leq 6.9$) is considered for the analysis as per available catalogue of this region. In the present study, declustering of aftershocks from the catalogue is accomplished using a moving space and time window (*Uhrhammer, 1986*). The events in regions A, B and C are 350, 777 and 615 respectively and add up to 1732 events, while 1010 events falls in the D region. Using these declustered data from homogenous catalogues for each region, the respective spatial and temporal b-values are estimated. The analysis is performed by making bin of 50 events (minimum number of events

in each node) (*Parsons, 2007*) with an overlap and smoothing of 5 events, adopting bootstrap of 20 realisations and grid spacing of 0.1×0.1. The M_c value for region A is 3.9 ± 0.13, b-value $= 0.73 \pm 0.12$ shown in Fig. 2a, in B region $M_c = 3.9 \pm 0.19$, b-value $= 0.81 \pm 0.12$ shown in Fig. 2b and M_c of C region is 3.9 ± 0.11, b-value $= 0.88 \pm 0.06$, shown in Fig. 2c. The M_c and b-value of combined A, B and C region ($\sim$1110 km segment) i.e. $M_c = 3.9 \pm 0.14$, b-value $= 0.69 \pm 0.06$ are in the similar range of A, B or C. Similarly, M_c value of D region is 3.9 ± 0.1 and b-value $= 0.75 \pm 0.05$ shown in Fig. 2d. The value of M_c in all A, B, C and D regions are significantly same though b-value is varying which signifies different seismicity behaviour in four sub-regions.

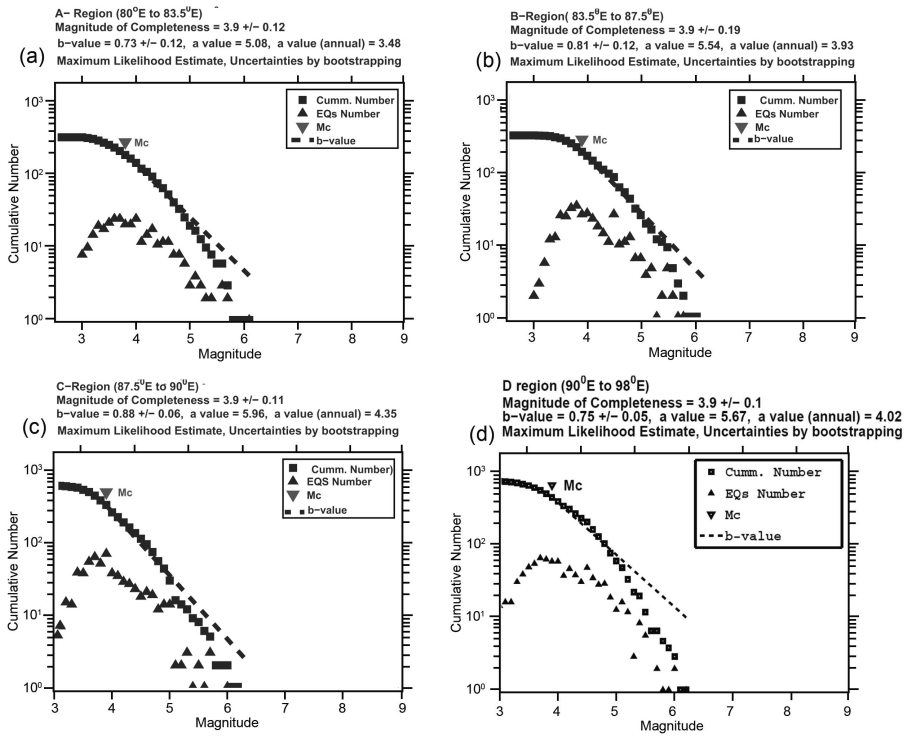

Fig. 2. Computed M_c – magnitude of completeness value (a) for A region (Central-western Nepal), (b) for B region (Central Nepal), (c) for C region (Eastern Nepal, Sikkim and Western Bhutan) and (d) for D region.

3. Results and Discussion

The seismicity and the spatial variations of b-value over latitudes of ∼26° N to 30°N (fixed) and longitudes of 80° to 90°E (A, B and C regions as defined earlier) is shown in Fig. 3a. The variations are presented over a latitude-longitude grid of 1° × 1°. The total temporal span is from 1975 to 2015 (40 years). It could be observed that most of the seismic events ($M_b \geq 5$) have occurred in the areas of low b-value. We suggest that the depletion in b-value depending upon the seismicity of the given region can indicate the occurance of moderate to large magnitude earthquake. For example, the region between 28.25°N – 29°N and 84.5°E – 86.5°E, with a very low b-value, hosts epicentres of the recent large Gorkha earthquake of Nepal on 25 April 2015 and 12 May 2015 (Fig. 3a). The low b-value shown in the spatial variation map (Fig. 3a) clearly suggests that this region is still developing stress which might release (*Sreejith et al., 2016; Sreejith et al., 2018*) in the form of a large earthquake or equivalent few moderate ones.

The b-values around the epicentre (26.77°N, 86.69°E) of the famous 1934 Bihar-Nepal earthquake of ∼8.4 M_w that was followed by an event of ∼6.9 M_w (26.71°N, 86.62°E) on 21 August 1988 are observed to remain high. This indicates that significant amount of differential stress around this area is being due for future earthquake. In further east, the region with a low b-value associated with deformed shape (major swerve) of MCT may spawn a large earthquake in the future. An earthquake of 6.5 M_w 18 September, 2011 (Sikkim earthquake, 27.80°N 88.15°E) in this region has already occurred.

The Assam region including Arunachal Pradesh and Bhutan is covered under D-region in Fig. 3b. This covers latitude belt from 26.5°N to 30°N and longitude belt from 90°E to 98°E. The C and D-regions are separated by Goalpara ridge at 90°E and north-south trending Dhubari fault and Yamuna lineament that extends till the southern part of Himalayan belt. This ridge is sandwiched between the Himalayan belt and Shillong plateau. The northward dipping of east-west extended Oldham fault during the great 1897 Assam earthquake uplifted the land of ∼1 m (*Bilham et al., 2001*) and enhanced the elevation of Shillong plateau. The spatial variability of b-value over this region during 1975 to 2015 is shown in Fig. 3b. We report that low b-value is observed in east of Kopli lineament to Bomdila lineament in

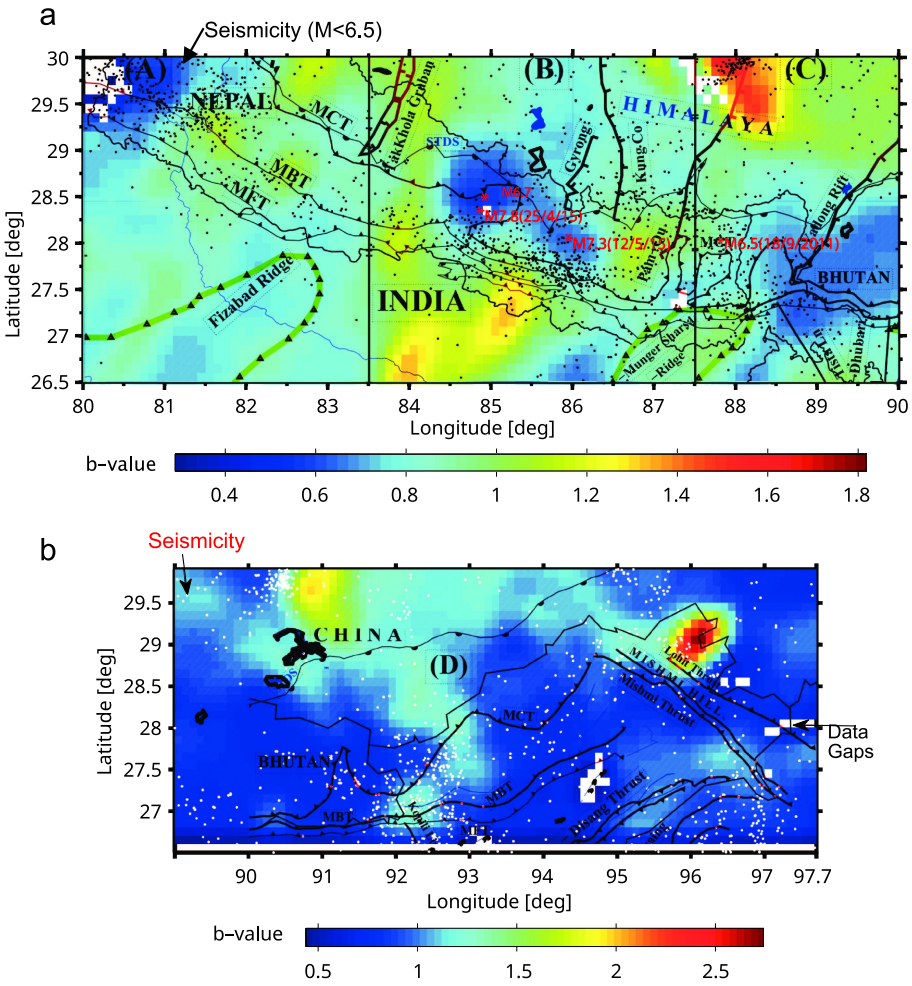

Fig. 3. Spatial variation of the b-value for 2 regions: (a) in Nepal, Sikkim and Bhutan region (A, B and C) shown with tectonic features – low b-value (in light blue colour) coincides with the source region of 25 April and 12 May, 2015 Nepal earthquakes marked as asterisks in red colour; (b) in Bhutan, Assam and Arunachal Pradesh (D region). Black (a) and white (b) dots denote seismicity ($3 < M_b > 6.5$) in the regions, white patches indicates loss of information.

southern part of Assam, Tista and Gangtok lineaments and Dhubari fault in western part of Assam and Sikkim-Bhutan. The low b-values are along

the oblique side of MCT and a region of Mishmi and Lohit thrust in eastern syntaxes zone. The higher b-values in central Bhutan indicates large occurrence of small magnitude earthquakes. Eastern Assam and Arunachal Pradesh hosted the great Assam earthquake (28.5°N, 96.7°E) of August 1950 with $\sim M_w$ 8.7. The northern regime of this event shows large b-values indicating the high heterogeneity due to the complex geological nature of this regime and could also relate to high pore pressure fluid flow with swarms (*Mukhopadhaya, 2015*).

In order to study the temporal variation of seismicity over the projected regions A, B, C and D, the b-values are derived in bins of 5 years. We interpret the temporal variations of b-value and the linear trend to understand the seismicity derived by plate movements in specific sub-divisions. As mentioned earlier, the regions A, B, C and D are segregated on the basis of geological features like faults, ridge, graben and rift structures (*Upreti and LeFort, 1999*) which are known to influence the local as well as regional seismicity with time (e.g. *Arora et al., 2012; Arora et al., 2014*). Regions A and B are separated by the Faizabad ridge in the southern portion of MFT and by Takkhola half graben in the north above MCT. Similarly B and C are separated by the Munger-Sersah ridge towards south of MFT and Pum Qu-Dinggya, Gyrong, Kung Co-Tingri and Xuru Co are graban /normal faults are extended from north of MBT to MCT. Various tectonic forces have further deformed arc shape of MCT into convex shape in this region. The region C and D is segmented on basis of seismically active Yadong-Gulu rift, extending from north to south in Sikkim region. While in Southern side, the Tista lineaments, Dhubari faults and Goalpara ridge are influencing seismicity of Himalayan and Shillong plateau (Fig. 1).

Region A, as shown in Fig. 4a, represents the temporal variation of seismic rate over the western Nepal region since 1975. It could be seen that b-value does not follow any specific cycle during the early years of the catalogue period (1975–2000). The later stage (2000–2010) shows a strong variability in seismicity over a temporal scale of ∼10 years. Earthquakes of $M \geq 5$ occurred mostly with the decreasing trend of b-values variation 1.6 to 0.74 i.e b-values < 1. The moderate to large earthquakes that occurred in the region are also depicted in this Fig. 3a and Fig. 4a–d. One could notice that occurrence of all moderate earthquakes is associated with b-values < 1. As the nature of the b-value variability shows an upward trend (1.02),

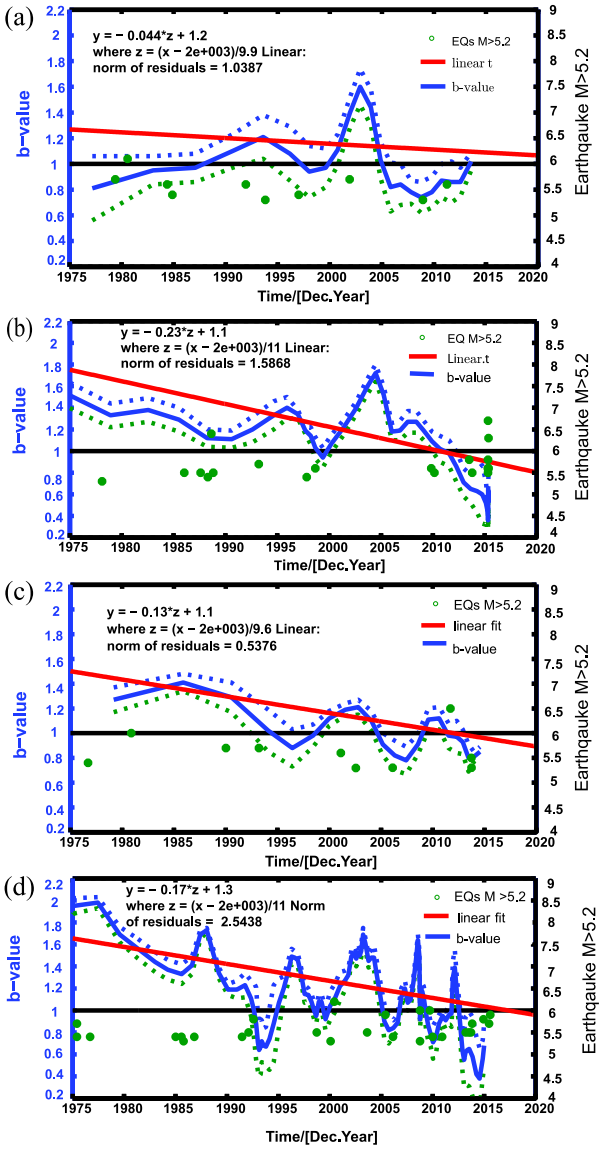

Fig. 4. Temporal variations of b-value (a) in A region i.e. western Nepal, (b) in B region i.e. central Nepal, (c) in C region i.e. eastern Nepal and (d) in D region i.e. northeast India during 1975 to 2015, the earthquakes with $M \geq 5$ are represented by green dots. Solid line indicates the average b-value and dashed line indicates ± 1 sigma. Redline is linear fit of b-value variations and black line is for b-value $= 1.0$.

poised to cross the value of 1 ("inflexion point"), we infer that the region is more prone to smaller magnitude earthquakes with magnitude ≤ 5 in the upcoming periods.

Fig. 4b represents the b-value variations with time over the central region of Nepal, B region. During the observation span the temporal variability of b-value is devoid of any systematic cyclic variations over this region. The positive residuals of b-value between 2003 and 2012 depict that the stress accumulation started in 2003 and continued until ∼2012. A couple of earthquakes $M \geq 5.0$ appeared after 2012. The lower trend in b-value (1.44 to 0.37) variability between 2012 and 2015 hosted the recent large Nepal earthquake or large volume of moderate earthquakes.

Fig. 4c shows the temporal variations of b-value (1.06 to 0.8) over eastern Nepal region including Sikkim. It could be observed that b-values follow cyclic variability over C-region. The cycle period falls ∼10 years e.g. 1980 with M∼6, 1990 with M∼5.7 and 2002 with M∼6.0. The recent major event of Sikkim occurred on 18 September 2011 with M∼6.5. The further down trend of b-value might indicate the occurrence of higher magnitude earthquake ($M > 5$).

The temporal variability of b-values over D-region is shown in Fig. 4d. It could be noticed that the variability is again cyclic with period ∼10 years. The region before 1990 cannot be characterised using b-value, as the recorded events were too few. A period of ∼10 years can be clearly emphasised after 1993. The frequent seismic activity after ∼2007 (b-value 1.07) produced more number of earthquakes ($M > 5$). The further lowering trend in b-value (0.72 to 0.56) may trigger more earthquakes of similar magnitude range in future.

4. Conclusions

The spatial and temporal variations in b-values during 1975 to 2015 is analysed over a broad region consisting the central and north-east Himalayan thrust regions. This study reveals the presence of several high and low stressed sub-regions in terms of low and high b-value respectively on dipping Indian plate. It is also shown that the locales of high b-value indicates the low stressed region and play host to small to moderate earthquakes. While, the regions with low b-value indicates the high stressed accumula-

tion over a period and are likely to spawn moderate to large earthquakes in the following years. The continuous fall of b-value for over a decade just before the Nepal earthquake sets a good example to support our argument.

The temporal variations of b-value provide fresh insight to the occurrence of impending earthquakes ($M > 5$ in the present case) in the demarcated sub-regions. Specifically, in the B region, based on temporal variations of b-value, it is found reasonable to state that decrease in b-value indicates stress build up and culminated with its release in April, 2015 in the form of the recent Nepal earthquake. In C-region, the cyclic nature of b-value variation suggests that moderate to large earthquake occurrence ($\sim M_w \geq 5$) in this region are periodic with an interval of 10 years. The last occurrence of such an event is the Sikkim earthquake 2011 (shown in Fig. 3a). Finally, in D-region, low b-value over Kopli Lineaments and eastern syntax region suggests that the effective stress is accumulating for e.g. in western Bhutan, upper part of Assam & eastern parts of Arunachal Pradesh near Mishmi hills and the region may experience moderate to large magnitude earthquake in future.

The present study can be appreciated in terms of interpreting the temporal and spatial variations in b-value as a tool to depict accumulation of stress in the region (*Scholz, 1968; Scholz, 2015; Sreejith et al., 2016; Sreejithy et al., 2018*). The cyclic behaviour of temporal variation of b-value is representing situation where the subducting Indian plate is locked during inter seismic period and it slips/releases/creeps during co-seismic and post seismic under specific tectonic circumstances. We believe that our study combined with detailed study of the critical geological features and tectonics of strain rate accumulation in the region by combine study of velocity vectors of GPS (Global Position System) and InSAR (Interferometry Synthetic Radar) impending to occurrence of large earthquakes in the the study region.

Acknowledgements. We would like to thank Dr. Stefan Wiemer, of the Swiss Seismological Service, Institute of Geophysics, Swiss Federal Institute of Technology Zurich for ZMAP software (*Wiemer, 2001*). We also thank P. Wessel and W. H. F. Smith for the GMT software. Susheel Kumar would like to acknowledge the support received from project CLAIMS of Indian Institute of Geomagnetism, Navi Mumbai. Nitin Sharma is thankful to receive the support from Earthquake Hazard Studies of CSIR – National Geophysical Research Institute, Hyderabad 500007, India.

References

Ader T., Avouac J.-P., Liu-Zeng J., Lyon-Caen H., Bollinger L., Galetzka J., Genrich J., Thomas M., Chanard K., Sapkota S. N., Rajaure S., Shrestha P., Ding L., Flouzat M., 2012: Convergence rate across the Nepal Himalaya and interseismic coupling on the Main Himalayan Thrust: Implications for seismic hazard. J. Geophys. Res., **117**, B4, B04403, doi: 10.1029/2011JB009071.

Adhikari B. R., Paudyal H., 2015: Spatial Variation of Seismicity in Central Himalayan Region. Himalayan Phys., **5**, 47–50, doi: 10.3126/hj.v5i0.12840.

Aki K., 1965: Maximum likelihood estimate of b in the formula $\log_N = a - bM$ and its confidence limits. Bull. Earthq. Res. Inst. Univ. Tokyo, **43**, 237–239.

Arora B. R., Gahalaut V. K., Kumar N., 2012: Structural control on along-strike variation in the seismicity of the northwest Himalaya. J. Asian Earth Sci., **57**, 15–24, doi: 10.1016/j.jseaes.2012.06.001.

Arora B. R., Prajapati S. K., Reddy C. D., 2014: Geophysical Constraints on the Seismotectonics of the Sikkim Himalaya. Bull. Seismol. Soc. Am., **104**, 5, 2278–2287, doi: 10.1785/0120130254.

Avouac J. P., 2003: Mountain building, erosion and the seismic cycle in the Nepal Himalaya. Adv. Geophys., **46**, 1–80, doi: 10.1016/S0065-2687(03)46001-9.

Bender B., 1983: Maximum likelihood estimation of b-values for magnitude grouped data. Bull. Seismol. Soc. Am., **73**, 3, 831–851.

Bhattacharya S. N., Dattatrayam R. S., 2000: Recent advances in seismic instrumentation and data interpretation in India. Curr. Sci., bf 79, 9, 1347–1358.

Bilham R., Gaur V. K., Molnar P., 2001: Himalayan seismic hazard. Science, **293**, 5534, 1442–1444, doi: 10.1126/science.1062584.

Bilham R., Larson K., Freymueller J., the Project IDYLHIM Members, 1997: GPS measurements of present-day convergence across the Nepal Himalaya. Nature, **386**, 61–64, doi: 10.1038/386061a0.

Caldwell W. B., Klemperer S. L., Lawrence J. F., Rai S. S., Ashish, 2013: Characterizing the Main Himalayan Thrust in the Garhwal Himalaya, India with receiver function CCP stacking. Earth Planet. Sci. Lett., **367**, 15–27, doi: 10.1016/j.epsl.2013.02.009.

Cattin R., Avouac J.-P., 2000: Modeling mountain building and the seismic cycle in the Himalaya of Nepal. J. Geophys. Res., **105**, B6, 13389–13407, doi: 10.1029/2000JB900032.

Chan C. H., Wu Y. M., Tseng T. L., Lin T. L., Chen C. C., 2012: Spatial and temporal evolution of b-values before large earthquakes in Taiwan. Tectonophysics, **532–535**, 215–222, doi: 10.1016/j.tecto.2012.02.004.

Dal Zilio L., Dinther Y., Gerya T., Avouac J.-P., 2019: Bimodal seismicity in the Himalaya controlled by fault friction and geometry. Nat. Commun., **10**, 48, doi: 10.1038/s41467-018-07874-8.

Fitch T. J., 1970: Earthquake mechanisms in the Himalayan, Burmese, and Andaman Regions and continental tectonics in central Asia. J. Geophys. Res., **75**, 4, 2699–2709, doi: 10.1029/JB075i014p02699.

Gansser A., 1964: The Geology of the Himalayas. Wiley Interscience, New York, 289 p.

Gutenberg B., Richter C. F., 1954: Seismicity of the Earth and Associated Phenomena. Princeton University Press, Princeton, N.J., USA, 2nd edn., 310 p.

Gutenberg B., Richter C. F., 1944: Frequency of earthquakes in California. Bull. Seismol. Soc. Am., **34**, 185–188.

Ishimoto M., Iida K., 1939: Observations of earthquakes registered with the recently constructed microseismograph (Observations sur les séismes enregistrés par le microsismographe construit dernièrement). Bull. Earthq. Res. Inst. Univ. Tokyo, **17**, 443–478 (in Japanese with French abstract).

Jade S., Mukul M., Bhattacharyya A. K., Vijayan M. S. M., 2007: Estimates of interseismic deformation in Northeast India from GPS measurements. Earth Planet. Sci. Lett., **263**, 3–4, 221–234, doi: 10.1016/j.epsl.2007.08.031.

Jade S., Mukul M., Gaur V. K., Kumar K., Shrungeshwar T. S., Satyal G. S., Dumka R. K., Jagannathan S., Ananda M. B., Kumar P. D., Banerjee S,, 2014: Contemporary deformation in the Kashmir-Himachal, Garhwal and Kumaon Himalaya: Significant insights from 1995–2008 GPS time series. J. Geodesy., **88**, 6, 539–557, doi: 10.1007/s00190-014-0702-3.

Kayal J. R., 2001: Microearthquake activity in some parts of the Himalaya and tectonic model. Tectonophysics, **339**, 3-4, 331–351, doi: 10.1016/S0040-1951(01)00129-9.

Kayal J. R., 2010: Himalayan tectonic model and the great earthquakes: an appraisal. Geomat. Nat. Haz. Risk, **1**, 1, 51–67, doi: 10.1080/19475701003625752.

Molnar P., Lyon-Caent H., 1989: Fault plane solutions of earthquakes and active tectonics of Tibetan Plateau and its margins. Geophys. J. Int., **99**, 1, 123–153, doi: 10.1111/j.1365-246X.1989.tb02020.x.

Mukhopadhyay B., 2011: Clusters of Moderate Size Earthquakes along Main Central Thrust (MCT) in Himalaya, Int. J. Geosci., **2**, 3, 318–325, doi: 10.4236/ijg.2011.23034.

Mukhopadhyay B., Dasgupta S., 2015: Earthquake swarms near eastern Himalayan Syntaxis along Jiali Fault in Tibet: A seismotectonic appraisal. Geosci. Front., **6**, 5, 715–722, doi: 10.1016/j.gsf.2014.12.009.

Mukul M., Jade S., Bhattacharyya A. K., Bhusan K., 2010: Crustal shortening in convergent orogens: Insights from Global Positioning System (GPS) measurements in India. J. Geol. Soc. India, **75**, 1, 302–312, doi: 10.1007/s12594-010-0017-9.

Ni J., Barazangi M., 1984: Seismotectonics of the Himalayan collision zone: Geometry of the under thrusting Indian Plate beneath the Himalaya. J. Geophys. Res., **89**, B2, 1147–1163, doi: 10.1029/JB089iB02p01147.

Nuannin P., Kulhanek O., Persson L., 2005: Spatial and temporal *b*-value anomalies preceding the devastating off coast of NW Sumatra earthquake of December 26, 2004. Geophys. Res. Lett., **32**, 11, L11307, doi: 10.1029/2005GL022679.

Ogata Y., Katsura K., 1993: Analysis of temporal and spatial heterogeneity of magnitude frequency distribution inferred from earthquake catalogues. Geophys. J. Int., **113**, 3, 727–738, doi: 10.1111/j.1365-246X.1993.tb04663.x.

Pandey M. R., Tandukar R. P., Avouac J. P., Lavé J., Massot J. P., 1995: Interseismic strain accumulation on the Himalaya crustal ramp (Nepal). Geophys. Res. Lett., **22**, 7, 751–754, doi: 10.1029/94GL02971.

Pandey M. R., Tandukar R. P., Avouac J. P., Vergne J., Héritier Th., 1999: Seismotectonics of the Nepal Himalaya from a local seismic network. J. Asian Earth Sci., **17**, 5–6, 703–712, doi: 10.1016/S1367-9120(99)00034-6.

Parsons T., 2007: Forecast experiment: Do temporal and spatial *b*-value variations along the Calaveras fault portend $M \geq 4.0$ earthquakes? J. Geophys. Res., **112**, B3, B03308, doi: 10.1029/2006JB004632.

Prasad S., Singh C., 2015: Evolution of b-values before large earthquakes of mb≥6.0 in the Andaman region. Geol. Acta, **13**, 3, 205–210, doi: 10.1344/GeologicaActa2015.13.3.3.

Pudi R., Roy P., Martha T. R., Kumar K. V., Rao P. R., 2018: Spatial Potential Analysis of Earthquakes in the Western Himalayas Using *b*-value and Thrust Association. J. Geol. Soc. India, **91**, 6, 664–670, doi: 10.1007/s12594-018-0921-y.

Rydelek P. A., Sacks I. S., 1989: Testing the completeness of earthquake catalogues and the hypothesis of self-similarity. Nature, **337**, 251–253, doi: 10.1038/337251a0.

Sapkota S. N., Bollinger L., Klinger Y., Tapponnier P., Gaudemer Y., Tiwari D., 2013: Primary surface rupture of the great Himalayan earthquakes of 1934 and 1255. Nat. Geosci., **6**, 71–76, doi: 10.1038/ngeo1669.

Schelling D., Arita K., 1991: Thrust tectonics, crustal shortening and the structure of the far-eastern Nepal Himalaya. Tectonics, **10**, 5, 851–862, doi: 10.1029/91TC01011.

Scholz C. H., 1968: The frequency-magnitude relation of microfracturing in rock and its relation to earthquakes. Bull. Seism. Soc. Am., **58**, 1, 399–415.

Scholz C. H., 2015: On the stress dependence of the earthquake *b* value. Geophysics Res. Lett., **42**, 5, 1399–1402, doi: 10.1002/2014GL062863.

Sreejith K. M., Sunil P. S., Agrawal R., Saji A. P., Ramesh D. S., Rajawat A. S., 2016: Coseismic and early post seismic deformation due to the 25 April 2015, M_w 7.8 Gorkha, Nepal, earthquake from InSAR and GPS measurements. Geophysical Research Letters, **43**, 7, 3160–3168, doi: 10.1002/2016GL067907.

Sreejith K. M., Sunil P. S., Agrawal R., Saji A. P., Rajawat A. S., Ramesh D. S., 2018: Audit of stored strain energy and extent of future earthquake rupture in central Himalaya. Scientific Reports volume 8, Article number: 16697.

Thakur V. C., 2004: Active tectonics of Himalayan Frontal Thrust and Seismic Hazard to Ganga Plain. Curr. Sci., **86**, 11.

Tsapanos T. M., 1990: b-values of two tectonic parts in the Circum Pacific belt. Pure Appl. Geophys., **134**, 2, 229–242, doi: 10.1007/BF00876999.

Uhrhammer R., 1986: Characteristics of northern and southern California seismicity. Earthquake Notes, **57**, 1, 21.

Upreti B. N., LeFort P., 1999: Lesser Himalayan crystalline nappes of Nepal: Problems their origin. In: Macfarlane A., Sorkhabi R. B., Quade J.: Himalaya and Tibet: Mountain Roots to Mountain Tops, Geol. Soc. Am. Spec. Pap., **328**, 225–238, doi: 10.1130/0-8137-2328-0.225.

Utsu T., 1999: Representation and analysis of the earthquake size distribution: a historical review and some new approaches. Pure Appl. Geophys., **155**, 2–4, 509–535, doi: 10.1007/s000240050276.

Valdia K. S, 1976: Himalayan transverse fault and their parallelism with subsurface structures of north its aftershocks Indian plane. Tectonophysics, **32**, 3–4, 353–386, doi: 10.1016/0040-1951(76)90069-X.

Wyss M., 1973: Towards a physical understanding of the earthquake frequency distribution. Geophys. J. R. Astro. Soc., **31**, 4, 341–359, doi: 10.1111/j.1365-246X.1973.tb06506.x.

Wiemer S., 2001: A software package to analyze seismicity: ZMAP. Seismol. Res. Lett., **72**, 374–383.

Woessner J., Wiemer S., 2005: Assessing the quality of earthquake catalogues: Estimating the magnitude of completeness and its uncertainty. Bull. Seismol. Soc. Am., **95**, doi: 10.1785/012040007.

Yeats R. S., Thakur V. C., 1998: Reassessment of earthquake hazard based on a fault-bend fold model of the Himalayan plate-boundary fault. Curr. Sci., **74**, 3, 230–233.

Zhao L.-S., Helmberger D. V., 1991: Geophysical implications from relocations of Tibetan earthquakes; Hot lithosphere. Geophys. Res. Lett., **18**, 12, 2205–2208, doi: 10.1029/91gl02865.

Zhao W., Nelson K. D., Che J., Quo J., Lu D., Wu C., Liu X., 1993: Deep seismic reflection evidence continental under thrusting beneath southern Tibet. Nature, **366**, 6455, 577–559, doi: 10.1038/366557a0.

sciendo

Contributions to Geophysics and Geodesy Vol. 49/3, 2019 (283–301)

The method of cycle-slip detection and repair GNSS meaturements by using receiver with high stability frequency oscillator

Nikolai S. KOSAREV*, Konstantin M. ANTONOVICH, Leonid A. LIPATNIKOV

Siberian State University of Geosystems and Technologies,
10 Plakhotnogo St., Novosibirsk, 630108 Russia;
e-mail: kosarevnsk@yandex.ru, kaf.astronomy@ssga.ru, lipatnikov_l@mail.ru

Abstract: A method of phase GNSS measurement control is described. The method is based on comparison of geometric range increments which are calculated using measurement data and approximate receiver coordinates and satellite navigation message position taking into account troposphere and ionosphere correction increments. Applicability of moving average for phase GNSS measurement control to detect the cycle slips and outliers is demonstrated. Test results of cycle slip detecting in phase measurements made by the receiver with high stability frequency oscillator are provided.

Key words: GNSS, receiver, measurement, carrier phase, cycle slip, moving average, geometric range

1. Introduction

The main objective of GNSS measurement quality check is to detect cycle slips in carrier phase, to correct them. Also outliers, which may be caused by multipath, and other various types of interference, can be eliminated by replacing measured value with smoothed value.

Carrier phase cycle slips occur when the receiver of the GNSS user loses the signal. Cycle slips may be evident, when the observation pause continues for several epochs, or non-evident when the observation restarts before the next observation epoch occurs. In any case there occurs an error for entire cycles value in phase observation ΔN, but still the fractional part remains

*corresponding author: tel. 8-913-706-9195, e-mail: kosarevnsk@yandex.ru

doi: 10.2478/congeo-2019-0015

the same as if there was no cycle slip (*Rizos, 1997; Seeber, 2003; Xu, 2003; Hofmann-Wellenhof et al., 2008; Joosten and Tiberius, 2000; Antonovich, 2005*).

There are two ways for solving problem of GNSS measurement quality control. The first one is measurement hardware and technique improvement for minimizing the number of cycle slips. The second one is development of mathematical methods for outliers detection and correction of cycle slips (*Kosarev, 2012*).

The improvement of satellite GNSS receivers' hardware includes ongoing receiving antennas design refinement and digital signal processing methods development. The improvement of mathematical GNSS quality control methods involves selection of approximating functions, code and phase pseudorange combination analysis etc. (*Kosarev, 2012*).

The works *Bastos and Landau (1988)*, *Cross and Ahmad (1988)*, *Collin and Warnant (1995)*, *Gao and Li, 1999)*, *Colombo et al. (1999)*, *Bisnath (2000)*, *Bisnath et al. (2001)*, *Banville and Langley (2010)*, *Banville and Langley (2012)* demonstrate cycle slips and outliers detection methods based on dual difference frequency difference analysis. The evident drawback of these methods is that it is impossible to use them for single GNSS receivers. The use of inertial-aided navigation systems (INS) enables to detect carrier phase cycle slips (losses) in kinematic measurements (*Lee et al., 2003; Du and Gao, 2012*). The works *Melbourne (1985)*, *Wübbena (1985)*, *Blewitt (1989)*, *Blewitt (1990)*, *Goad and Yang (1994)* describe outliers detection methods based on code and phase pseudoranges differences, phase pseudorange and iono-free combination differences, and time measurement differences.

The works *Zhalilo (2003, 2007)*, *Zhalilo and Sadanova (2004)* demonstrate the detailed research of Ukrainian scientists devoted to outliers detection methods that were proposed earlier.

There are a number of publications by A. S. Tolstikov and D. V. Stubarev (*Stubarev and Tolstikov, 2004; Stubarev, 2006a,b; Stubarev, 2008a,b*) which devoted to methods of outliers detection based on imitation modelling using measurement data imitator ModBis24, which is developed in Siberian Scientific Research Institute of Metrology.

The algorithm for outlier detection is based on analyzing difference between phase measurements and reference trajectory. Smoothing by Cheby-

shev polynomials, Kalman filtering and robust processing procedures are applied.

For detection and editing cycle slips and outliers authors of the present article developed a technique for GNSS measurements quality control based on computation of geometric range increment using approximate coordinates of the station and orbit of the satellite. The distinction of the proposed technique from the aforementioned ones is that here we use differences between two successive measurements epochs and compare them to their modeled values which can be obtained with higher precision than phase measurements if some conditions are satisfied. Those conditions refer to measurement interval, accuracy of station's position and satellite orbit. The most important condition is that the GNSS receiver is equipped with highly stable atomic frequency standard (*Antonovich and Kosarev, 2011; Antonovich and Kosarev, 2012a,b*).

2. Theory

The code pseudoranges P_i (meters) and carrier phase ϕ_i (cycles) for frequency bands $L1$, $L2$ at moments (measurement epochs) t_i, $i = 1, \ldots, n$ separated by interval Δt. Phase differences $\Delta\phi$ between two successive epochs are determined as follows (*Antonovich and Kosarev, 2011; Antonovich and Kosarev, 2012a,b*):

$$\Delta\phi_{i,i+1}(L1) = \phi_{i+1} - \phi_i = \frac{1}{\lambda_{L1}} \Big[\Delta\rho_{i,i+1} - \Delta I_{i,i+1} + \Delta T_{i,i+1} + \\ + \Delta\delta m_{i,i+1} + (A1(r)_{i,i+1} - A1(s)_{i,i+1}) \cdot \Delta t \Big], \quad (1)$$

where: $\Delta\rho$ – geometric range shift;
ΔI – ionospheric delay shift;
ΔT – tropospheric delay shift;
$\Delta\delta m$ – multipath influence shift on the phase measurement;
$A1(r), A1(s)$ – receiver and satellite clock rate;
λ – wavelength.

Topocentric distance increment (geometric range shift) $\Delta\rho$ is introduced as follows:

$$\Delta\rho_{i,i+1} = \rho_{i+1} - \rho_i \,, \quad (2)$$

where ρ_i calculated as:

$$\rho_i = \sqrt{(X - X_i)^2 + (Y - Y_i)^2 + (Z - Z_i)^2}\,. \tag{3}$$

In equation (3): station position is given in the earth-centered earth-fixed reference system, for example, by ITRS vector $\mathbf{R} = (X, Y, Z)^T$. Satellite position vectors $\mathbf{r_i} = (X_i, Y_i, Z_i)^T$ are calculated at the moments of signal emission t_i in the system time scale. According to definition of pseudorange P_i:

$$P_i = c\,(t_i' - t_i''), \tag{4}$$

where t_i' is the nominal moment in time scale implemented by the user's receiver clock, t_i'' – moments of signal transmission in the timescale of the GNSS satellite, c – speed of light in vacuum. Therefore, the moments t_i can be calculated according to formula:

$$t_i = t_i' - P_i/c + \mathrm{d}t_i^s. \tag{5}$$

Here $\mathrm{d}t_i^s$ is shift of space vehicle (SV) timescale relative to the system timescale at the moment of signal generation.

Algorithm for calculation of vectors $\mathbf{r_i}$ is provided in the Interface Control Document (*ICD-GPS-200C, 1993*). It is important to correct vectors $\mathbf{r_i}$ to take into account influence of rotation of the earth-centered earth-fixed (ECEF) reference frame during signal propagation from satellite to receiver i.e. Sagnac effect (*Rizos, 1997; Seeber, 2003; Xu, 2003*).

In papers *Antonovich and Kosarev (2012a,b)*, *Antonovich and Kosarev (2011)* authors consider using approximate station and satellite positions for calculation of geometric ranges increments. For demonstration of applicability of geometric ranges increments for phase measurements quality control let us introduce a geocentric reference system $\mathrm{O}\xi\eta\zeta$ shown in Fig. 1. For the sake of simplicity fundamental plane $\mathrm{O}\xi\eta$ coincides with orbital plane of the satellite which is in zenith of the station. In Fig. 1:

- O – center of Earth's mass (geocenter);
- ξ axis is aimed along radius vector R to the station A at which observations are made;
- η axis lies in the orbital plane perpendicular to the radius vector of the station;

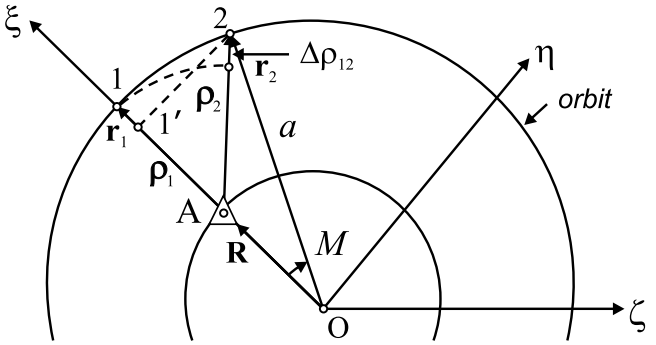

Fig. 1. Differerence of topocentric distances.

– ζ axis is perpendicular to the orbital plane.

Satellite orbit is considered circular, radius equals a. If disturbances are neglected, position $\mathbf{R}$ of the station and position of the satellite $\mathbf{r}_1$ at the moment t_1 can be presented as follows:

$$\mathbf{R} = \begin{bmatrix} R \\ 0 \\ 0 \end{bmatrix}, \quad \mathbf{r}_1 = \begin{bmatrix} a \\ 0 \\ 0 \end{bmatrix}. \tag{6}$$

Position of the satellite at t_2 can be calculated using following expressions:

$$\mathbf{r}_2 = \begin{bmatrix} a \cdot \cos M \\ a \cdot \sin M \\ 0 \end{bmatrix}, \tag{7}$$

$$M = n \cdot \Delta t\,, \tag{8}$$

where n is mean motion, $\Delta t = t_2 - t_1$, M – central angle (analogue of mean anomaly).

Then the topocentric vectors $\boldsymbol{\rho}_1$, $\boldsymbol{\rho}_2$ pointing to satellite at the moments t_1, t_2 are calculated according the formulae:

$$\boldsymbol{\rho}_1 = \mathbf{r}_1 - \mathbf{R} = \begin{bmatrix} a - R \\ 0 \\ 0 \end{bmatrix}, \quad \boldsymbol{\rho}_2 = \mathbf{r}_2 - \mathbf{R} = \begin{bmatrix} a \cdot \cos M - R \\ a \cdot \sin M \\ 0 \end{bmatrix}. \tag{9}$$

Scalars of vectors i.e. geometric ranges:

$$\rho_1 = |a - R|, \quad \rho_2 = \left|[a^2 - 2aR\cos M + R^2]^{1/2}\right|. \tag{10}$$

Topocentric range difference between the two epochs:

$$\Delta\rho = \rho_2 - \rho_1 = [a^2 - 2aR\cos M + R^2]^{1/2} - (a - R)\,. \tag{11}$$

Assume small errors $\mathrm{d}\xi$, $\mathrm{d}\eta$, and $\mathrm{d}\zeta$, such that real position of the station is defined by the formula:

$$\mathbf{R}' = \begin{bmatrix} R + \mathrm{d}\xi \\ \mathrm{d}\eta \\ \mathrm{d}\zeta \end{bmatrix}. \tag{12}$$

New topocentric vectors:

$$\boldsymbol{\rho}_1' = \mathbf{r}_1 - \mathbf{R}' = \begin{bmatrix} a - R - \mathrm{d}\xi \\ -\mathrm{d}\eta \\ -\mathrm{d}\zeta \end{bmatrix}, \tag{13}$$

$$\boldsymbol{\rho}_2' = \mathbf{r}_2 - \mathbf{R}' = \begin{bmatrix} a \cdot \cos M - R - \mathrm{d}\xi \\ a \cdot \sin M - \mathrm{d}\eta \\ -\mathrm{d}\zeta \end{bmatrix}, \tag{14}$$

and correspondingly their scalars are:

$$\rho_1' = |\mathbf{r}_1 - \mathbf{R}'| = \left[(a - R - \mathrm{d}d\xi)^2 + \mathrm{d}\eta^2 + \mathrm{d}\zeta^2\right]^{1/2}, \tag{15}$$

$$\rho_2' = |\mathbf{r}_2 - \mathbf{R}'| = \left\{[a\cos M - R - \mathrm{d}\xi]^2 + (a\sin M - \mathrm{d}\eta)^2 + \mathrm{d}\zeta^2\right\}^{1/2}. \tag{16}$$

Applying first-order Taylor expansion for (15) and (16) by $\mathrm{d}\xi$, $\mathrm{d}\eta$, $\mathrm{d}\zeta$, one may get:

$$\rho_1' = \rho_1 - \mathrm{d}\xi\,, \tag{17}$$

$$\rho_2' = \rho_2 - \mathrm{d}\xi(a\cos M - R)/\rho_2 - \mathrm{d}\eta\, a\sin M/\rho_2\,. \tag{18}$$

Formula (18) shows no influence of $\mathrm{d}\zeta$ error in the first-order approximation. Then the difference of new topocentric distances can be expressed in the following way:

$$\Delta\rho' = \rho'_2 - \rho'_1 = \rho_2 - \rho_1 - \mathrm{d}\xi(a\cos M - R)/\rho_2 + \mathrm{d}\xi - \mathrm{d}\eta\, a\sin M/\rho_2\,, \quad (19)$$

Deviation of this difference from the true value caused by errors in relative position of the stations and in orbit of the satellite equals to:

$$\nabla\Delta\rho = \Delta\rho' - \Delta\rho = -\mathrm{d}\xi(a\cos M - R)/\rho_2 + \mathrm{d}\xi - \mathrm{d}\eta a\sin M/\rho_2\,. \quad (20)$$

Expanding trigonometric functions of angle M to series, using (20), yields:

$$\nabla\Delta\rho = \Delta\rho' - \Delta\rho = -\mathrm{d}\xi\Big(a\Big[1 - (n\Delta t)^2/2\Big] - R\Big)\Big/\rho_2 + \mathrm{d}\xi - \mathrm{d}\eta\, a(n\Delta t)/\rho_2. \quad (21)$$

The Table 1 contains values of topocentric range changes depending on errors $\mathrm{d}\xi$, $\mathrm{d}\eta$, and also on interval Δt. Calculation was carried assuming $a = 26560$ km, R = 6378 km, $n = 30°$/hr.

Table 1. The dependence of the geometric range increments errors on mutual satellite and station positions errors and time interval.

Errors of satellite – station relative position (M)	Geometric range increments error (mm) in time interval Δt (sec)							
	$\Delta t = 1$	$\Delta t = 2$	$\Delta t = 5$	$\Delta t = 10$	$\Delta t = 20$	$\Delta t = 30$	$\Delta t = 60$	$\Delta t = 600$
$\mathrm{d}\xi = \mathrm{d}\eta = 1$	0.2	0.5	1	2	4	6	11	107
$\mathrm{d}\xi = \mathrm{d}\eta = 5$	1	2	5	10	19	29	57	540
$\mathrm{d}\xi = \mathrm{d}\eta = 10$	1.9	3.8	9.5	19	38	57	114	1079

It is evident from Table 1 that in many cases influence of coordinate errors is below the noise level of P-code measurements (nearly 0.3 m).

The change of tropospheric delay between the two epochs can be represented by the formula:

$$\Delta T_{i,i+1} = T_z(\mathrm{cosec}\,\varepsilon_{i+1} - \mathrm{cosec}\,\varepsilon_i)\,, \quad (22)$$

with standard deviation:

$$\sigma_{\Delta T} = \sigma_{T_z}(\mathrm{cosec}\,\varepsilon_{i+1} - \mathrm{cosec}\,\varepsilon_i)\,, \quad (23)$$

with σ_{T_z} of about 0.2–0.4 m (*Antonovich, 2005*).

Changes of ionospheric delay can be calculated using formulae:

$$\Delta I_{L1,i,i+1} = \bar{I}_{L1,v}(F_{i+1} - F_i), \quad \Delta I_{L2,i,i+1} = \bar{I}_{L2,v}(F_{i+1} - F_i)\,. \quad (24)$$

where F – obliquity factor, $\bar{I}_{L1,v}$ and $\bar{I}_{L2,v}$ averaged vertical ionospheric delays $I_{L1,v,i}$, $I_{L2,v,i}$ at some interval between the epochs t_{i_1} and t_{i_2}:

$$\bar{I}_{L1,v} = \frac{1}{i_2 - i_1} \sum_{i_1}^{i_2} I_{L1,v,i}, \quad \bar{I}_{L2,v} = \frac{1}{i_2 - i_1} \sum_{i_1}^{i_2} I_{L2,v,i} \,. \tag{25}$$

Vertical ionospheric delays $I_{L1,v,i}$, $I_{L2,v,i}$ at epochs t_i for frequency bands $L1$ and $L2$ calculated as:

$$I_{L1,v,i} = \frac{I_{L1,i}}{F_i} = k \cdot \frac{P_{L2,i} - P_{L1,i}}{F_i}, \quad I_{L2,v,i} = \frac{f_{L1}^2}{f_{L2}^2} I_{L1,v,i} \,. \tag{26}$$

To minimize vertical ionospheric delays errors one can perform additional averaging through different satellites data. It's especially important in case if there are no P-code measurements.

The formulae for root mean square (RMS) deviations $\sigma_{\Delta I,L1}$, $\sigma_{\Delta I,L2}$ for differential ionospheric delays can be represented by the formula:

$$\begin{aligned} \sigma_{\Delta I,L1,i,i+1} &= \frac{k(F_{i+1} - F_i)}{F_i \sqrt{i_2 - i_1}} \sqrt{2} \sigma_P \,, \\ \sigma_{\Delta I,L2,i,i+1} &= \frac{f_{L1}^2}{f_{L2}^2} \frac{k(F_{i+1} - F_i)}{F_i \sqrt{i_2 - i_1}} \sqrt{2} \sigma_P \,. \end{aligned} \tag{27}$$

The formulae show that ionosphere model errors depend mostly on root mean square error of code pseudorange σ_P, which in its turn depends on equipment-specific noise level and on the type of code measurements (*Leick, 1995*).

Multipath modelling is a complicated issue. It has quasiperiodic nature. Amplitude can reach 5–6 cm and its period is 5 minutes or larger (*Leick, 1995*).

Table 2 contains modelled values of changes in tropospheric and ionospheric delays, multipath effect and their RMS errors $\sigma_{\Delta T}$, $\sigma_{\Delta I}$, $\sigma_{\Delta \delta m}$ calculated given $\varepsilon \approx 15°$, $i_2 - i_1 = 1$.

Additional contribution to variance $\sigma_{\Delta\phi}^2$ is introduced by frequency instability of the satellite clock σ_f^s / f and of the station clock $\sigma_{f,r} / f$. They are random values. Their influence in equation (1) can be evaluated using the following formula:

$$\sigma_{\Delta t} = c \, \Delta t \, \frac{\sqrt{\sigma_{f,r}^2 + (\sigma_f^s)^2}}{f} \,. \tag{28}$$

Table 2. Influence of tropospheric and ionospheric refraction and multipath on phase pseudorange increments (mm).

Time interval	Tropospheric delay		Ionospheric delay			Multipath	
	ΔT	$\sigma_{\Delta T}$	ΔI	$\sigma_{\Delta I}$ (GPS P-code)	$\sigma_{\Delta I}$ (GLONASS C/A code)	$\Delta\delta m$	$\sigma_{\Delta\delta m}$
$\Delta t =$ 1 sec	1.3	0.4	5.2	0.1	1.6	1	1
$\Delta t = 10$ sec	13	4.2	52	1.2	24.5	7	7
$\Delta t = 30$ sec	40	12.4	160	3.6	72	21	21

For GLONASS satellites σ_f^s/f has order of $(1\text{–}5)\cdot 10^{-13}$ (*Xu, 2003*), which adds 1–5mm to $\sigma_{\Delta t}$ if $\Delta t = 30$ sec. Using receivers with highly stable atomic clocks is necessary to reduce the influence of receiver's clock error to a level comparable to satellite clock errors. Such atomic clocks are installed on some stations of International GNSS Service (IGS) and also on the stations of GNSS ground control segment. It is expected that small-scale atomic clocks with relative frequency instability of $5\cdot 10^{-12}$ on one hour interval may appear in field geodetic GNSS receivers soon (*Quantum SA 45s; Shkel, 2011*).

After accounting for all mentioned effects formula (1) may be rewritten as follows:

$$\Delta\phi_{i,i+1}(L1) = \frac{1}{\lambda_{L1}}[(\rho_{i+1}-\rho_i)-\bar{I}_{L1}(F_{i+1}-F_i)+T_z(\operatorname{cosec}\varepsilon_{i+1}-\operatorname{cosec}\varepsilon_i)]. \quad (29)$$

Expression for $L2$ band will have analogous form. Noise of phase measurements in those equations is neglected because it does not exceed 3 mm.

Increments $\Delta\phi_i$ modelled according to formula (29) generally are not equal to increments $\Delta\widetilde{\phi}_i$ calculated using measurements. Let us calculate discrepancies v_i (frequency band designation is omitted):

$$v_i = \Delta\phi_i - \Delta\widetilde{\phi}_i\,. \quad (30)$$

We fill further consider v_i consisting of systematic and random parts:

$$v_i = \Delta d_i + \Delta\varepsilon_i\,, \quad (31)$$

$$\Delta d_i = E(v_i)\,, \quad (32)$$

where Δd_i is increment of systematic error of GNSS phase measurements model equal to mathematical expectation $E(v_i)$; $\Delta\varepsilon_i$ is an estimate of random change of error on the interval with zero mathematical expectation.

Systematic part of the error Δd_i can be found by smoothing discrepancies v_i in the window $[i-k,\, i+k]$:

$$\Delta d_i = \bar{v}_{[i-k,i+k]}\,. \tag{33}$$

Smoothing of discrepancies is proposed to be performed using moving average. The smoothed value will lag by k intervals. Median filtering is applied to avoid influence of outliers on the estimate of mathematical expectation (*Stubarev and Tolstikov, 2004; Stubarev, 2006a,b; Stubarev, 2008a,b; Stubarev, 2010*). Unpredictable effects including both cycle slips and other outliers in GNSS measurements, can emerge in random error part $\Delta\varepsilon_i$:

$$\Delta\varepsilon_i = v_i - \Delta d_i\,. \tag{34}$$

RMS σ_i is calculated using Bessel's formula:

$$\sigma_i = \sqrt{\frac{\sum\limits_{j=i-k}^{i+k} \Delta\varepsilon_j^2}{2k}}\,. \tag{35}$$

Value $\Delta\varepsilon_i$ is considered an outlier if the following conditions are satisfied:

$$|\Delta\varepsilon_i| > 2\cdot\sigma_i\,, \quad |\Delta\varepsilon_i| > \Sigma\,, \tag{36}$$

where Σ is RMS error of measurement increment modelling by formula:

$$\Sigma = \sqrt{\sigma_{\Delta T}^2 + \sigma_{\Delta I}^2 + \sigma_{\Delta\rho}^2 + \sigma_{\Delta t}^2}\,. \tag{37}$$

If an outlier is identified, it can be corrected. If $\Delta\varepsilon_i$ magnitude is larger than the wavelength, it means that a cycle slip has occurred. It is well-known that in case of cycle slip all further phase measurements are biased by integer number of cycles but its fractional part is unaffected. Therefore, one can calculate corrected measurement $\bar{\phi}_i$ using formula:

$$\bar{\phi}_i = \mathrm{int}(\phi_i) + \mathrm{frac}(\widetilde{\phi}_i)\,, \tag{38}$$

where 'int' is an operator for separation of integer part of the value, a 'frac' – extraction of fractional part.

If the cycle slip has occurred previously, restoring can be performed according to formula:

$$\bar{\phi}_{i+1} = \widetilde{\phi}_i + \Delta\phi_{i+1} + \Delta d_{i+1}\,, \tag{39}$$

where $\bar{\phi}_{i+1}$ – smoothed value; $\widetilde{\phi}_i$ – measured value at previous epoch. Systematic part of the error Δd_{i+1} can be extrapolated linearly.

3. Experiment 1

Let us analyze the discrepancies through the GNSS measurement results, obtained at Mendeleevo station on January 1st, 2013. The measurements results files are available on the website of the International GNSS Service (IGS) datacenters. The station is equipped with dual-frequency and double system GNSS-receiver Topcon NetR3, connected to hydrogen frequency standard. The interval of measurements is 30 s. The station coordinates was get from RINEX file, the GPS satellite coordinates errors were estimated by difference between precise and navigational ephemerids of 1.5 m, and GLONASS satellites – about 3 m. Two GPS and two GLONASS satellites were chosen for the experiment. Observation session was nearly one hour. Satellite tracks were in different parts of observer's celestial sphere (see Table 3).

Table 3. Trajectories of the satellites.

GNSS	Satellite	UT time		Elevation of satellite	
		t_{start}	t_{end}	$\varepsilon_{\text{start}}$	ε_{end}
GPS	G1	22^h52^m	23^h46^m	17°	7°
GPS	G13	15^h00^m	16^h00^m	52°	82°
GLONASS	R1	7^h00^m	8^h00^m	15°	48°
GLONASS	R19	$0^h00.5^m$	$0^h55.5^m$	68°	40°

The calculations were performed using MATLAB 6.5 software. To calculate discrepancies we used the moving average with averaging window covering 7 epochs. Fig. 2 shows results for GPS G1 satellite ($L1$ frequency), Fig. 3 – for GLONASS R9 satellite ($L1$ frequency).

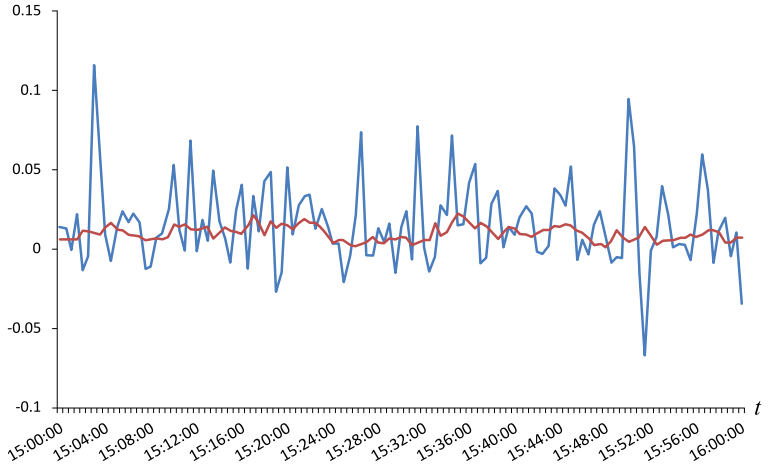

Fig. 2. Result of GPS G13 phase data filtration. Phase discrepancy in meters: blue – measured minus predicted, red – smoothed discrepancy.

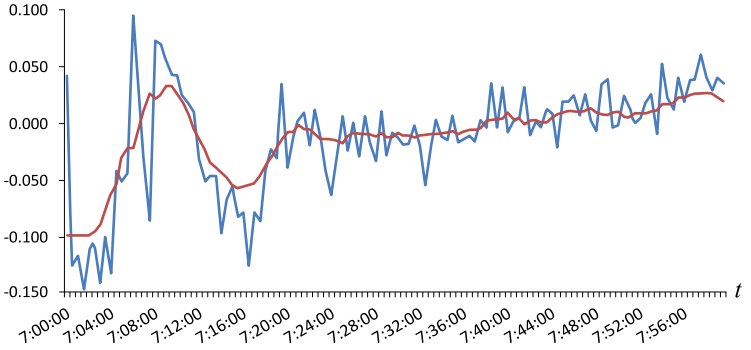

Fig. 3. Result of GLONASS R19 phase data filtration. Phase discrepancy in meters: blue – measured minus predicted, red – smoothed discrepancy.

Then the filtering procedure for cycle slips detection and correction was tested on evident and non-evident cycle slips, which were modeled. To model the evident cycle slip for the satellite G13 a 5-minute data gap was created. Then the slip ΔN was introduced into phase data:

$$\Delta N = \mathrm{int}(P_{\mathrm{end}} - P_{\mathrm{start}})/\lambda\,, \tag{40}$$

where P_{start} and P_{end} are the P-code pseudorange values at the start and at

the end of data gap accordingly (Fig. 4a). To model the non-evident cycle loss the satellite GLONASS R1 data was used. The modeling was performed in the same way, but were chosen the neighboring values (Fig. 4b).

Then the data were restored by formula (39). To take into account the ionospheric delay the code pseudorange values were restored as well. The differences between the restored and initial carrier phase data are shown in Fig. 5.

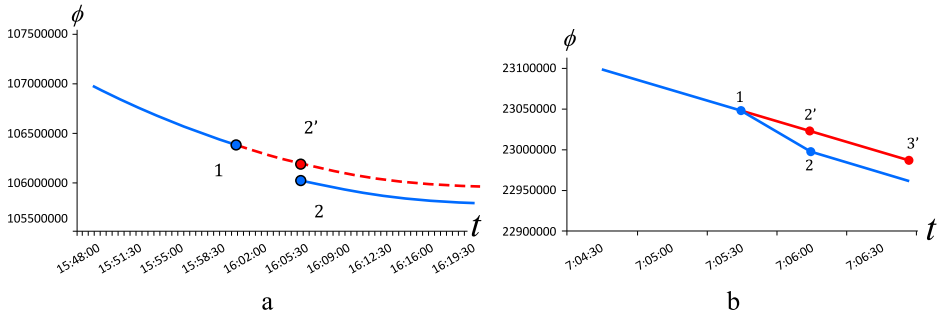

Fig. 4. The modeling of evident and non-evident carrier phase cycle loss: (a) for satellite GPS G13, (b) for satellite GLONASS R1. Where: 1 is the starting gap measurement point, 2 is the restarting measurement point. The blue color shows initial data, the red one is the restored data.

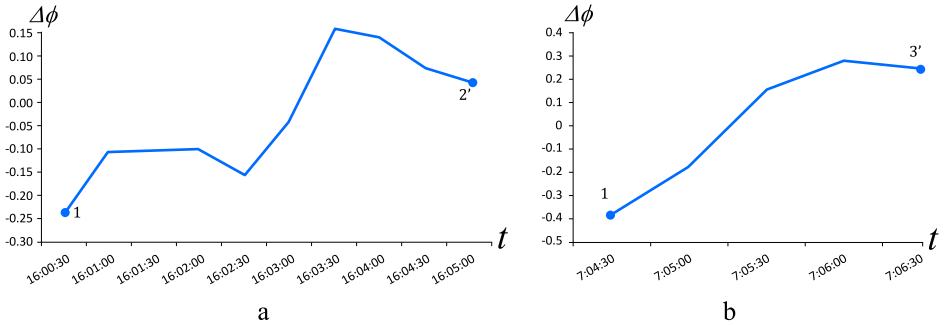

Fig. 5. The Differences between the really measured and modeled carrier phase (in cycles): (a) for satellite GPS G13, (b) for satellite GLONASS R1.

The analysis of Figs. 2–5 obviously shows that the application of median filtering for cycle counting losses detection enables to restore qualitative and reliable measurement data, provided by both GPS and GLONASS satellites. The application of the filter, based on median filtering, enables to definitely

and exactly detect cycle counting losses on the level of 5 cm, which is 1/4 wave length.

4. Experiment 2

Validation of cycle slip and outlier detection based on moving average was conducted. For that purpose a numerical simulation was carried out. Non-evident cycle slips were randomly introduced into RINEX observation data.

Observation session was 6 hours. Measurements were performed using JAVAD Sigma G3T equipment with 1 sec interval. The receiver was connected to highly stable frequency standard Ch1-1006.

The data file obtained during the experiment was preprocessed using OCTAVA_PPA software, developed by Kharkov research group. Available version software allows you to process only GPS measurements. The aim was to eliminate non-modeled cycle slips and multipath effect in the test data (*Zhalilo and Sadanova, 2004*). Thus, etalon observation data were obtained which were not subject to those sources of errors.

Result of precision assessment of $L1$ and $L2$ phase measurements preprocessed using OCTAVA_PPA software is shown in figures 6 and 7 for all observed GPS satellite. Algorithms for preprocessing GPS measurements implemented in the OCTAVA_PPA software are given in the articles (*Zhalilo, 2003, 2007; Zhalilo and Sadanova, 2004*).

Figs. 6 and 7 show absence of cycle slips. It is seen the noise level is mostly within ± 2 cm.

Initial measurements interval was 1 sec. Thinned out datasets with 5 sec, 10 sec, 15 sec, 30 sec intervals were obtained by resampling down the initial dataset. Non-evident cycle slips were introduced into initial dataset and to the thinned out datasets using two approaches. The first approach consisted in introduction of cycle slips with magnitude of 1 cycle at random epochs. The second approach implied introduction of cycle slips (again magnitude was 1 cycle) into selected interval of observations in initial and resampled down datasets. Then the cycle slips were detected using the proposed technique. In Table 4 results of cycle slips detection are provided.

Results in Table 4 show that the technique enables reliable single cycle slips detection. It is important that the per cent of detected cycle slips is large independently on the interval of measurements if it does not exceed

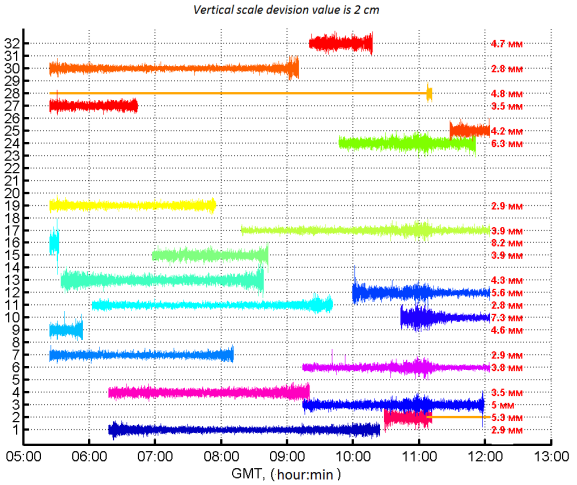

Fig. 6. Precision assessment of preprocessed $L1$ phase measurements for all observed GPS satellites.

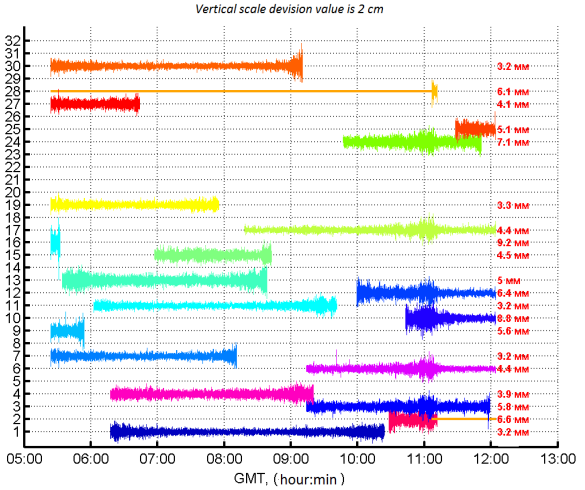

Fig. 7. Precision assessment of preprocessed $L2$ phase measurements for all observed GPS satellites.

30 s.

As it is evidently shown by Table 5 the technique allowed to detect nearly 100 % of single (one cycle) slips on the measurements interval up to 10 min.

Table 4. Results of detection of 1-cycle slips introduced into the etalon and resampled down datasets.

Measurements interval	Number of modeled single cycle slips		Portion of detected cycle slips	
	Totally	By satellite		
1 sec	700	G07 – 200	100 %	100 %
		G01 – 500		100 %
5 sec	400	G24 – 200	99 %	99 %
		G28 – 200		99 %
10 sec	200	G24 – 100	99 %	98 %
		G28 – 100		99 %
15 sec	200	G07 – 50	98 %	100 %
		G15 – 50		95 %
		G28 – 100		98 %
30 sec	100	G07 – 30	100 %	100 %
		G15 – 30		100 %
		G30 – 40		100 %

Table 5. Results of detection of single cycle slips introduced into the specific interval of the etalon datasets.

Measurements interval	Number of modelled single cycle slips introduced into selected time span	Portion of detected cycle slips
1 sec	G07 – 30 (30 sec)	100 %
1 sec	G07 – 60 (60 sec)	100 %
1 sec	G07 – 300 (5 min)	100 %
1 sec	G07 – 600 (10 min)	99 %

5. Conclusion

Application of GNSS receivers equipped with highly stable frequency generators opens new prospects for phase measurements quality control. The developed technique allows detection and correction of cycle slips and outliers. Unlike other techniques of phase measurements quality control based on search in observation space the proposed technique relies on calculation of geometric range and atmospheric effects increments. Those increments may be calculated using approximate coordinates of the station and the satellite

(the obtained using navigation message data). Increments of tropospheric and ionospheric delays are calculated using simple mapping functions. As a result of phase measurements quality control a file containing corrected values free of cycle slips and outliers can be obtained. Additionally an estimate of noise level for the dataset is provided which is necessary for quality assessment of measurements. This information can further be used for shaping measurements covariance matrix and improvement of solution accuracy in geodesy and navigation.

References

Antonovich K. I., 2005: The application of satellite radio-navigation systems in geodesy. Moscow, Kartgeocenter, Novosibirsk, Science, 334 p. (in Russian).

Antonovich K. I., Kosarev N. S., 2011: About one possibility of nonstop carrier phase control in GNSS observations. Interexpo GEO-Siberia – 2011, 19–29 April 2011, Novosibirsk, **1**, 2, SSGA, 2011, 164–168.

Antonovich K. I., Kosarev N. S., 2012a: Geometric range application for GNSS measurement control. Interexpo GEO-Siberia – 2012, **1**, 2, Geodesy, cartography, mine surveying: information package of scientific congress Interexpo GEO-Siberia – 2012, 10–20 April 2012, Novosibirsk, SSGA, 2012, 245–250.

Antonovich K. I., Kosarev N. S., 2012b: Method of code and phase pseudorange control in coordinate. High School publisher Geodesy and aerial photo survey, 2/1, 11–15 (in Russian).

Banville S., Langley R. B., 2010: Instantaneous cycle-slip correction for real-time PPP application. NAVIGATION, Journal of the Institute of Navigation, **57**, 4, 325–334.

Banville S., Langley R. B., 2012: Cycle slips correction for single-frequency PPP. In: Proceedings of the 25th International Technical Meeting of the Satellite Division of The Institute of Navigation (ION GNSS 2012), Nashville, TN, September 17–21, 2012, 3753–3761.

Bastos L., Landau H., 1988: Fixing cycle slips in dual-frequency kinematic GPS-applications using Kalman filtering. Manuscr. Geod., **13**, 4, 249–256.

Bisnath S. B., 2000: Efficient, automated cycle-slip correction of dual frequency kinematic GPS data. In: Proceedings of ION GPS 2000, Salt Lake City, Utah, 145–154.

Bisnath S. B., Kim D., Langley R. B., 2001: A new approach to an old problem: Carrier-phase cycle slips. GPS World, **12**, 5, 46–51.

Blewitt G., 1989: Carrier phase ambiguity resolution for the Global Positioning System applied to geodetic baselines up to 2000 km. J. Geophys. Res., **94**, B8, 10187–10203, doi: 10.1029/JB094iB08p10187.

Blewitt G., 1990: An automatic editing algorithm for GPS data. J. Geophys. Res., **17**, 3, 199–202, doi: 10.1029/gl017i003p00199.

Collin F., Warnant R., 1995: Application of wavelet transform for GPS cycle slip correction and comparison with Kalman filter. Manuscr. Geod., **20**, 3, 161–172.

Colombo O. L., Bhapkar U. V., Evans A. G., 1999: Inertial-aided cycle-slip detection/correction for precise, long-baseline kinematic GPS. In: Proceedings of the ION GPS, Nashville, TN, USA, September 14–17, 1999, 1915–1921.

Cross P. A., Ahmad N., 1988: Field validation of GPS phase measurements. GPS-Techniques Applied to Geodesy and Surveying, Groten E., Strauß R. (Eds.): Proceedings of the International GPS-Workshop, Darmstadt, April 10–13, 1988, 349–360.

Du S., Gao Y., 2012: Inertial aided cycle slip detection and identification for integrated PPP GPS and INS. Sensors 2012, **12**, 11, 14344–14362, available online: https://www.ncbi.nlm.nih.gov/pmc/articles/PMC3522917/pdf/sensors-12-14344.pdf, doi: 10.3390/s121114344.

Gao Y., Li Z., 1999: Cycle slip detection and ambiguity resolution algorithms for dual-frequency GPS data processing. Mar. Geod., **22**, 3, 169–181, doi: 10.1080/01490419927344 3.

Goad C., Yang M., 1994: On automatic precision airborne GPS positioning. Proceedings of the International Symposium on Kinematic Systems in Geodesy, Geomatics and Navigation KIS'94, Banff, Alberta, Canada, August 30–September 2, 1994, 131–138.

Hofmann-Wellenhof B., Lichtenegger H., Wasle E., 2008: GNSS – Global Navigation Satellite Systems: GPS, GLONASS, Galileo and more. Wien, New-York: Springer, 516 p.

Interface Control Document ICD-GPS-200C, 1993: Navstar GPS Space Segment/Navigation User Interfaces. October 10, 1993–January 14, 2003, available online: https://navcen.uscg.gov/pubs/gps/icd200/ICD200Cw1234.pdf.

Joosten P., Tiberius C. C. J. M., 2000: Fixing the ambiguities. Are you sure they're right? GPS World, **11**, 5, 46-51.

Kosarev N. S., 2012: Restoration of carrier phase: problems and decision ways. Vestnik of the Siberian State University of Geosystems and Technologies (SSUGT), **1**, 17, 53–59 (in Russian).

Lee H.-K., Wang J., Rizos C., 2003: Effective cycle slip detection and identification for high precision GPS/INS integrated systems. J. Navig., **56**, 3, 475–486, doi: 10.1017/S0373463303002443.

Leick A., 1995: GPS Satellite Surveying. New York, Wiley-Interscience; 2nd ed., 560 p.

Melbourne W. G., 1985: The case for ranging in GPS based geodetic systems. In: Proceedings of the 1st International Symposium on Precise Positioning with the Global Positioning System, Goad C. (Ed.), Rockville, MD, USA, April 15–19, 1985, 373–386.

Quantum SA 45s Chip scale atomic clock. Available online: https://www.microsemi.com/document-portal/doc_download/133305-sa-45s-csac-datasheet.

Rizos C., 1997: Principles and Practice of GPS Surveying. Monograph, School of Geomatic Engineering, The University of New South Wales, Sydney, available online: http://www.sage.unsw.edu.au/sites/sage/files/SAGE_collection/MonographSeries/mono17.pdf.

Seeber G., 2003: Satellite Geodesy. Berlin, New York: Walter de Gruyter, 589 p.

Shkel A. M., 2011: Microtechnology Comes of Age. GPS World, **22**, 9, 43–50.

Stubarev D. V., Tolstikov A. S., 2004: Algorithm for preliminary processing of pseudorange measurements. In: Modern Problems of Radio Electronics. An Anthology, Krasnoyarsk State Technological University, Krasnoyarsk, 425–427 (in Russian).

Stubarev D. V., 2006a: Exclusion of outliers in results of trajectory observations. Stubarev D. V., Tolstikov A. S., Vestnik SGGA, **11**, Novosibirsk, SSGA, 25–29.

Stubarev D. V., 2006b: Smooth replenishment of missing trajectory observation data. Vestnik SGGA, **11**, Novosibirsk, SSGA, 33–38.

Stubarev D. V., 2008a: Study on algorithms for preliminary data processing using imitation modelling methods. Electronic resource: `http://www.jurnal.org/articles/2008/izmer11.html`.

Stubarev D. V., 2008b: Tasks of data preprocessing for requestless measurements (Zadachi predvaritel'noy obrabotki dannykh bezzaprosnykh izmereniy) Stubarev D. V., Tolstikov A. S., Proceedings of the IV International Congress Geo-Siberia 2008. Specialized instrument making, metrology, thermal physics, micromechanics. **4**, part 2., April 22–24 2008, Novosibirsk, SSGA, 150–153.

Stubarev D. V., 2010: Using imitation modelling methods for analysis of algorithms for preliminary processing of trajectory observation data. Stubarev D. V., Tolstikov A. S., Nauchniy vestnik NGTU, **2**, 39, 127–136.

Wübbena G., 1985: Software developments for geodetic positioning with GPS using TI 4100 code and carrier measurements. In: Proceedings of the 1st International Symposium on Precise Positioning with the Global Positioning System, Goad C. (Ed.), Rockville, MD, USA, April 15–19, 1985, 403–412.

Xu G., 2003: GPS Theory, algorithms and applications. Springer-Verlag Berlin Heidelberg New York, 315 p.

Zhalilo A. A., 2003: Carrier-Phase cycle – slip detection and repair of dual-frequency GPS data – new technique using correlation filtering principle. In: Proceedings of the 10th Saint Petersburg International Conference on Integrated Navigation System, St. Petersburg, Russia, May 26–28, 2003, 273–276.

Zhalilo A. A., Sadanova N. V., 2004: Carrier-phase cycle-slip detection, estimation and correction of dual-frequency GPS data – new efficient technique, algorithms and experimental results. Astronomy in Ukraine — Past, Present and Future: Abstract book, MAO-2004 Conference devoted to the 60th anniversary of the Main Astronomical Observatory of the National Academy of Sciences of Ukraine, July,15–17, Kiev, Ukraine, 154.

Zhalilo A. A., 2007: Carrier-phase cycle-slip detection and repair of single/dual-frequency GPS/GNSS observations – New universal technique and algorithms. In: Proceedings of 14th Saint Petersburg International Conference on Integrated Navigation Systems, St. Petersburg, Russia, 28–30 May, 2007, 293–302.

sciendo

Contributions to Geophysics and Geodesy Vol. 49/3, 2019 (303–324)

Multiple-linear regression to best-estimate of gravity parameters related to simple geometrical shaped structures

Mohammed TLAS, Jamal ASFAHANI*

Atomic Energy Commission,
P. O. Box 6091, Damascus, Syria, e-mail: pscientific@aec.org.sy

Abstract: A new interpretative approach is proposed to best-estimate of gravity parameters related to simple geometrical shaped structures such as a semi-infinite vertical cylinder, an infinite horizontal cylinder, and a sphere like structures. The proposed technique is based on the multiple-linear regression oriented towards estimating the model parameters, e.g., the depth from the surface to the center of the buried structure (sphere or infinite horizontal cylinder) or the depth from the surface to the top of the buried object (semi-infinite vertical cylinder), the amplitude coefficient, and the horizontal location from residual gravity anomaly profile. The validity of the proposed approach is firstly demonstrated through testing different synthetic data set corrupted and contaminated by a white Gaussian random noise level. The theoretical synthetic obtained results obviously show that the estimated parameters values, derived by the proposed technique are close to the assumed true parameters values. This approach is applied on five real field residual gravity anomalies taken from Cuba, Sweden, Iran, USA, and Germany, where the efficacy of this new approach is consequently proven. A comparable and acceptable agreement is noticed between the results derived by this proposed approach and those obtained from the real field data information.

Key words: Gravity anomaly, sphere-like structure, semi-infinite vertical cylinder-like structure, infinite horizontal cylinder-like structure, multiple-linear regression

1. Introduction

The geophysical gravity method is largely used in gas and oil exploration. Most of the geological structures in oil and mineral exploration can be approximated by simple geological structures such as a sphere, a semi-infinite vertical cylinder, an infinite horizontal cylinder, a fault, a sheet, and a dike. Several interpretative techniques have been already developed

*corresponding author: e-mail: jasfahani@aec.org.sy

doi: 10.2478/congeo-2019-0016

to interpret gravity field anomalies, due to simple geometric models. The main objective of those techniques utilize the mentioned approximations to best-estimate the gravity parameters values, e.g., the depth to the buried body and the amplitude coefficient. The developed methods include, linear optimization-simplex algorithm (*Asfahani and Tlas, 2015*), neural network modeling (*Abedi et al., 2010*), differential evolution algorithm (*Ekinci et al., 2016*), graphical methods (*Nettleton, 1962; 1976*), ratio methods (*Bowin et al., 1986; Abdelrahman et al., 1989*), Fourier transform (*Odegard and Berg, 1965; Sharma and Geldart, 1968*), Euler deconvolution (*Thompson, 1982*), neural network (*Elawadi et al., 2001*), Mellin transform (*Mohan et al., 1986*), least-squares minimization approaches (*Gupta, 1983; Lines and Treitel, 1984; Abdelrahman, 1990; Abdelrahman et al., 1991; Abdelrahman and El-Araby, 1993; Abdelrahman and Sharafeldin, 1995a*), Werner deconvolution (*Hartmann et al., 1971; Jain, 1976*).

Werner deconvolution technique is extended by *Kilty (1983)* to analyze the gravity data using both the residual anomaly and its first and second horizontal derivatives. *Ku and Sharp (1983)* further refined the method by using iteration for reducing and eliminating the interference field and then applied Marquardt's non-linear least squares method to further refine automatically the first approximation provided by deconvolution. A new automatic technique, called AN-EUL, and based on a combination of the analytic signal and the Euler deconvolution method is introduced by *Salem and Ravat (2003)* to interpret the magnetic data. Both the location and the approximate geometry of a magnetic source can be deduced by the use of the AN-EUL. *Fedi (2007)* proposed a method called depth from extreme points (DEXP) to interpret any potential field through describing the theory for the gravity and magnetic fields and their derivatives for any order. The DEXP technique allows the estimation of the source depths, density and structural index from the extreme points of a 3D field scaled according to specific power laws of the altitude. An alternative method is presented by *Salem and Smith (2005)* to estimate both the depth and model type using the first order local wave number approach, without the need for third order derivatives of the field. A normalization of the first order local wave-number anomalies is achieved in their method, where a generalized equation is constructed to estimate the depth of some 2D magnetic sources regardless of the source structure.

Silva and Barbosa (2003) derived the analytical estimators for the horizontal and vertical source position in 3D Euler deconvolution as a function of the x, y, and z derivatives of the magnetic anomaly within a data window. *Barbosa et al. (1999)* proposed a new criterion, based on the correlation between the total magnetic field anomaly and the estimates of an unknown base level to determine the structural index, *Salem et al. (2008)* developed a new method based on derivatives of the tilt angle to interpret the gridded magnetic data, where a simple linear equation, similar to the 3D Euler equation is obtained. Their approach evaluates both the horizontal location and the depth of magnetic bodies, without specifying prior information about the nature of the sources. *Fedi et al. (2009)* proposed a new method based on a 3D multiridge analysis of potential field. Their method assumes a 3D subset in the harmonic region and analyzes the behavior of the potential field ridges, which are built by joining extreme points of the field computed at different altitudes.

Few techniques only however, have treated the determination of shape of the buried structure. These techniques include, for example, Walsh transform (*Shaw and Agarwal, 1990*), least-squares methods (*Abdelrahman and Sharafeldin, 1995b; Abdelrahman et al., 2001a,b)*, constrained and penalized nonlinear optimization technique (*Tlas et al., 2005*). The determination of the depth, shape factor, and amplitude coefficient of the buried structure is generally achieved by those methods from residual gravity anomaly, where the accuracy of the results, gathered by them, depend on the accuracy in which the residual anomaly can be separated and isolated from the observed gravity anomaly.

A simple and easy interpretative approach based on the multiple-linear regression is proposed to interpret residual gravity field anomalies and to best-estimate the model parameters values, e.g., the depth to the top or to the center of the body, the horizontal location and the amplitude coefficient related to a buried sphere or a semi-infinite vertical cylinder or an infinite horizontal cylinder-like structure.

The validity of the new proposed approach is demonstrated using synthetic data set corrupted and contaminated by white Gaussian random noise levels of 15% and 25%. The theoretical obtained results clearly show that the estimated parameter values derived by this approach are very close to the assumed true values of parameters.

The accuracy of the new proposed approach is also proven through interpreting five real field gravity anomalies, taken from Cuba, Sweden, Iran, USA, and Germany. The obtained results indicate acceptable and comparable agreements between the results derived by the proposed technique and those obtained by other interpretation methods. The depth obtained by the proposed method is moreover found to be in high accordance with that obtained from the real field data information.

2. Theory

A theoretical and synthetic residual gravity anomaly related to various geological models such as a sphere, a semi-infinite vertical cylinder and an infinite horizontal cylinder are treated to demonstrate the validity and the applicability of the new proposed approach.

2.1. Interpretation of residual gravity anomaly due to simple geometrical models

The general expression of the residual gravity anomaly (V) at any point $M(x)$ along the x-axis of a semi-infinite vertical cylinder-like structure, an infinite horizontal cylinder-like structure and a sphere-like structure, in a Cartesian coordinate system (Fig. 1) can be written according to *Gupta (1983)*, and *Asfahani and Tlas (2015)* as:

$$V(x_i) = \frac{k}{\left((x_i - x_0)^2 + z^2\right)^q}\,, \quad i = 1, ..., N\,, \tag{1}$$

where q is the geometrical shape factor of the buried structure given in discrete values as follows: $q = 1.5$ for a sphere, $q = 0.5$ for a semi-infinite vertical cylinder and $q = 1$ for an infinite horizontal cylinder, x_0 is the horizontal location of the buried body, z is the depth from the surface to the center of the buried structure (sphere or infinite horizontal cylinder) or the depth from the surface to the top of the buried object (semi-infinite vertical cylinder), k is the amplitude coefficient given by the following mathematical expression: $k = \frac{4}{3}\pi G\rho r^3 z$ for a sphere, $k = \pi G\rho r^2$ for a semi-infinite vertical cylinder and $k = 2\pi G\rho r^2 z$ for an infinite horizontal cylinder, ρ is the density contrast, G is the universal gravitational constant, r is the radius, and finally $x_i,\ i = 1, ..., N$ is the horizontal position coordinate.

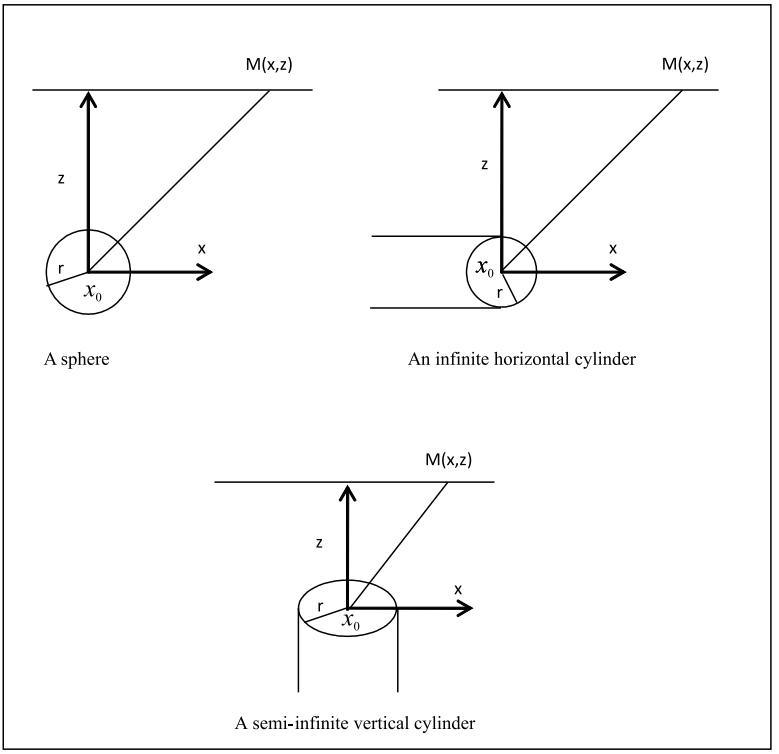

Fig. 1. Diagrams of simple geometrical structures (sphere, infinite horizontal cylinder, and semi-infinite vertical cylinder).

The set of Eq. (1) consists of N nonlinear equations in function of the three independent parameters k, x_0 and z. The term V_i will be used, for simplification, instead of the term $V(x_i)$, $i = 1, ..., N$, in the rest of the paper.

From Eq. (1), it can be easily observed that the sign of the parameter k is similar and coincident to the sign of V_i, $i = 1, ..., N$.

Taking the absolute values of both sides of Eq. (1) we find:

$$|V_i| = \frac{|k|}{\left((x_i - x_0)^2 + z^2\right)^q}, \quad i = 1, ..., N. \tag{2}$$

After the performing of some mathematical manipulation of the Eq. (2) we get:

$$|V_i|^{\frac{1}{q}} x_i^2 = 2x_0 |V_i|^{\frac{1}{q}} x_i - \left(x_0^2 + z^2\right) |V_i|^{\frac{1}{q}} + |k|^{\frac{1}{q}}, \quad i = 1, ..., N. \tag{3}$$

The introduction of the following new variables:

$$A = 2x_0, \tag{4}$$

$$B = -\left(x_0^2 + z^2\right), \tag{5}$$

$$C = |k|^{\frac{1}{q}}, \tag{6}$$

$$\begin{aligned} O_i &= |V_i|^{\frac{1}{q}} x_i^2, \quad i = 1, ..., N, \\ P_i &= |V_i|^{\frac{1}{q}} x_i, \quad i = 1, ..., N, \\ Q_i &= |V_i|^{\frac{1}{q}}, \quad i = 1, ..., N, \end{aligned} \tag{7}$$

into Eq. (3) allows to write the following equation:

$$O_i = AP_i + BQ_i + C, \quad i = 1, ..., N. \tag{8}$$

Eq. (8) being linear between the variables O_i, P_i, Q_i, $i = 1, ..., N$, the unique optimal values of the coefficients A, B, and C for a specific discrete value of $q \in \{0.5, 1, 1.5\}$, a priori assumed, can be easily determined. Such determination is carried out through performing the multiple-linear regression between the dependent variable O_i, $i = 1, ..., N$ and the independent variables P_i, Q_i, $i = 1, ..., N$, with the use of one of the familiar statistical programs as Microsoft Excel or Statistica, and or through solving the following set of simultaneously linear equations by the well-known direct method of Gauss:

$$\begin{aligned} \left(\sum_{i=1}^{N} P_i^2\right) A + \left(\sum_{i=1}^{N} P_i Q_i\right) B + \left(\sum_{i=1}^{N} P_i\right) C &= \sum_{i=1}^{N} O_i P_i, \\ \left(\sum_{i=1}^{N} P_i Q_i\right) A + \left(\sum_{i=1}^{N} Q_i^2\right) B + \left(\sum_{i=1}^{N} Q_i\right) C &= \sum_{i=1}^{N} O_i Q_i, \\ \left(\sum_{i=1}^{N} P_i\right) A + \left(\sum_{i=1}^{N} Q_i\right) B + (N)\, C &= \sum_{i=1}^{N} O_i. \end{aligned} \tag{9}$$

The best-estimate of the horizontal location (x_0) of the buried body can be obtained from Eq. (4), after knowing the unique optimal values of A, B and C for $q \in \{0.5, 1, 1.5\}$ as the following:

$$x_0 = \frac{A}{2}\,. \tag{10}$$

The best-estimate of the depth (z) from the surface to the center of the buried structure (sphere or infinite horizontal cylinder) or the depth from the surface to the top of the buried object (semi-infinite vertical cylinder) can be derived from Eq. (5) as:

$$z = \frac{\sqrt{|4B + A^2|}}{2}\,. \tag{11}$$

The best-estimate of the amplitude coefficient (k) can be also obtained from Eq. (6) as:

$$k = C^q \quad \text{when} \quad V_i \geq 0\,, \quad i = 1, ..., N, \tag{12}$$

$$k = -C^q \quad \text{when} \quad V_i \leq 0\,, \quad i = 1, ..., N. \tag{13}$$

It is useful to mention that there is no loss of generality in assuming the source geometry of the gravity anomaly as a priori known. In addition, there are no imposed restrictions on the generality of the proposed approach.

Before explaining how we can solve this ambiguity and this inconvenience, we will define the statistical criterion of preference called the Root Mean Square Error (*RMSE; Collins, 2003*). *RMSE* is based on the minimal value, between the field gravity data anomaly and the computed gravity one, obtained through using the estimated values of z, x_0 and k resulted from Eqs. (10–13) for a specific discrete value of the geometric shape factor $q \in \{0.5, 1, 1.5\}$. The mathematical formula of this statistical criterion *RMSE* is given as:

$$RMSE = \sqrt{\frac{\sum\limits_{i=1}^{N} \left(V_i\left(Observed\right) - V_i\left(Computed\right)\right)^2}{N}}\,, \tag{14}$$

where $V_i\left(Observed\right)$ and $V_i\left(Computed\right)\,,\ i = 1, ..., N$ are the observed and the computed gravity values at the point $x_i,\ i = 1, ..., N$, respectively.

In the case where the source geometry of the gravity field anomaly is unknown, the following next procedure composed of three steps should be followed:

- First, the gravity field anomaly is interpreted by adapting and assuming the source geometry as a semi-infinite vertical cylinder ($q = 0.5$), where Root Mean Square Error $RMSE\_V$ is computed using Eq. (14) with the estimated values of z, x_0 and k derived from Eqs. (10–13).
- Second, the gravity field anomaly is re-interpreted by adapting the source geometry as an infinite horizontal cylinder ($q = 1$), where the Square Correlation Coefficient $RMSE\_H$ is also computed using Eq. (14) with the estimated values of z, x_0 and k derived from Eqs. (10–13).
- Third, the gravity field anomaly is re-interpreted by assuming the source geometry as a sphere ($q = 1.5$), where the Square Correlation Coefficient $RMSE\_S$ is also computed using Eq. (14) with the estimated values of z, x_0 and k derived from Eqs. (10–13).

The lowest one of the three reached values of $RMSE\_V$, $RMSE\_H$ and $RMSE\_S$ is selected as a convincible solution, which exactly indicates to the suitable source geometry related to the responsible gravity field anomaly.

Another statistical criterion of preference (square of correlation coefficient) can be also used to select the best optimum gravity solution. It is defined through the following mathematical expression:

$$R^2 = \frac{\left(\sum\limits_{i=1}^{N} \left(V_i\left(Obs.\right) - \bar{V}\left(Obs.\right) \right) \times \left(V_i\left(Comp.\right) - \bar{V}\left(Comp.\right) \right) \right)^2}{\sum\limits_{i=1}^{N} \left(V_i\left(Obs.\right) - \bar{V}\left(Obs.\right) \right)^2 \times \sum\limits_{i=1}^{N} \left(V_i\left(Comp.\right) - \bar{V}\left(Comp.\right) \right)^2}, \qquad (15)$$

where $\bar{V}\left(Obs.\right)$ and $\bar{V}\left(Comp.\right)$ are the arithmetic means of $V_i\left(Obs.\right)$ and $V_i\left(Comp.\right)$, $i = 1, ..., N$ respectively. R-squared is computed for the three assumed types of geometric shapes of the buried structure, R^2_V, R^2_H and R^2_S for a semi-infinite vertical cylinder ($q = 0.5$), an infinite horizontal cylinder ($q = 1$), and a sphere ($q = 1.5$) respectively, by using Eq. (15) with the estimated values of z, x_0 and k resulted from Eqs. (10–13).

The highest one of the three reached values of R^2_V, R^2_H and R^2_S is selected as a convincible solution, which directly indicates to the suitable source geometry related to the responsible gravity field anomaly.

2.2. Interpretation of a synthetic gravity anomaly due to a sphere model with Gaussian random noise

A synthetic gravity anomaly $V(x_i),\ i = 1, ..., N$ due to a sphere-like structure is generated from Eq. (1), by using the following values of model parameters: geometric shape factor $q = 1.5$, depth from the surface to the center of the buried spherical structure $z = 35$ m, amplitude coefficient $k = 1500\ \mathrm{mGal\,m^3}$, and the horizontal location $x_0 = 5$ m.

The generated synthetic anomaly is contaminated by white Gaussian random noise of 15% and 25% maximum level using continuous normal distribution, such as new additional gravity anomalies are generated (Fig. 2 and Fig. 3). This regenerated gravity anomalies are consequently interpreted by the new proposed approach. The obtained parameters (z, k, x_0) and the preference criterions $(RMSE, R^2)$ for the three structures a priori assumed; a semi-infinite vertical cylinder, an Infinite horizontal cylinder, and a sphere are summarized in detail in Table 1.

From Table 1, the lowest one of the three reached values of $RMSE\_V$, $RMSE\_H$ and $RMSE\_S$ or the highest one of the three reached values of R^2_V, R^2_H and R^2_S clearly indicates that the suitable source geometry related to the responsible contaminated synthetic gravity anomaly is a sphere.

The results presented in Table 1 show that the estimated parameter values, obtained by the proposed method, are very close to the true assumed

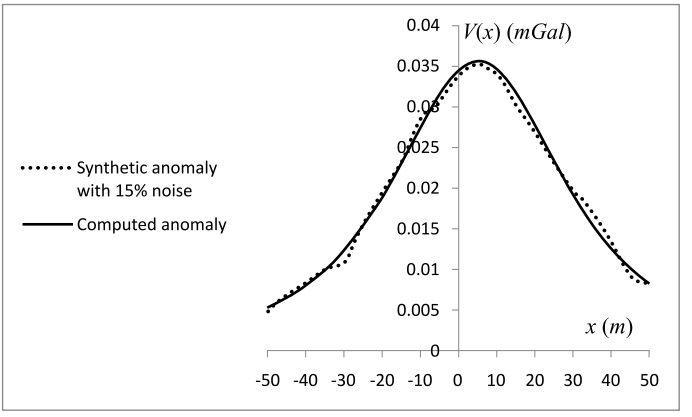

Fig. 2. Diagrams of the computed anomaly and synthetic data set due to a sphere with adding a maximum of 15% random noise.

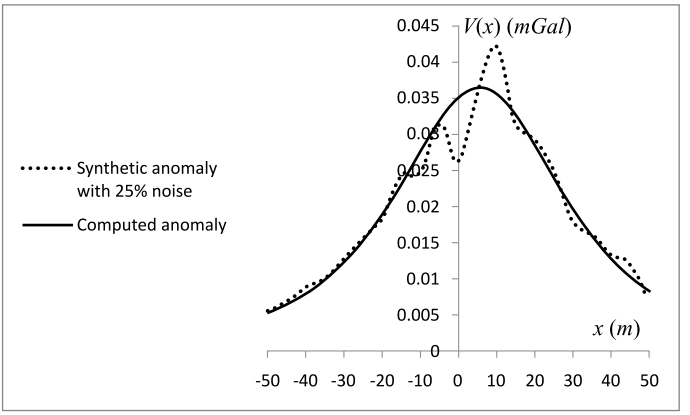

Fig. 3. Diagrams of the computed anomaly and synthetic data set due to a sphere with adding a maximum of 25% random noise.

Table 1. Interpretation of a synthetic gravity anomaly with 15% and 25% maximum level of Gaussian random noise.

Source geometric shape	Model parameters	True values of model parameters	Estimated values of model parameters with maximum 15% random noise	Estimated values of model parameters with maximum 25% random noise
Semi-infinite vertical cylinder ($q = 0.5$)	z (m)	35	9.6802	9.2577
	k (mGal m)	1500	0.4400	0.4402
	x_0 (m)	5	5.7053	6.0398
	$RMSE$ (mGal)	–	0.0040	0.0045
	R^2	–	0.9005	0.8659
Infinite horizontal cylinder ($q = 1$)	z (m)	35	24.1526	23.6664
	k (mGal m^2)	1500	21.9485	21.6798
	x_0 (m)	5	5.5931	5.8338
	$RMSE$ (mGal)	–	0.0025	0.0028
	R^2	–	0.9710	0.9314
Sphere ($q = 1.5$)	z (m)	35	34.8422	34.3145
	k (mGal m^3)	1500	1505	1472
	x_0 (m)	5	5.5.2868	5.4353
	$RMSE$ (mGal)	–	0.0019	0.0027
	R^2	–	0.9753	0.9342

values of parameters. This clearly proves the efficiency of the new proposed approach.

3. Application to field data

The new proposed approach is applied to interpret five field residual gravity anomalies measured over various geological structures. The five field gravity anomalies are interpreted according to the three different geological structures, e.g., a sphere, an infinite horizontal cylinder, and a semi-infinite vertical cylinder. The resulting model with the lowest reached value of *RMSE* and the highest reached value of R^2 is selected as the best and the suitable model solution for estimating the parameters of the field residual gravity anomaly.

3.1. Interpretation of the Chromites filed residual gravity anomaly

Fig. 4 shows a normalized residual field gravity anomaly measured over a chromites deposit in Camaguey province, Cuba (*Robinson and Coruh, 1988*). The gravity anomaly is interpreted by the new proposed approach by assuming a priori the source geometry as a semi-infinite vertical cylinder,

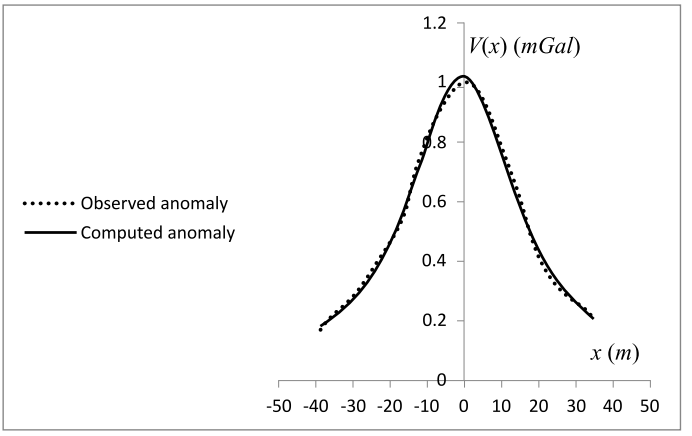

Fig. 4. Normalized residual gravity field anomaly over a chromites deposit, Camaguey province, Cuba. The evaluated curve by the proposed approach is presented for an infinite horizontal cylinder model.

an infinite horizontal cylinder, and a sphere. All acquired results are shown in Table 2.

Table 2. Interpretation of the Chromites field residual gravity anomaly, Cuba.

Model parameters	Semi-infinite vertical cylinder	Infinite horizontal cylinder	Sphere
z (m)	7.2116	17.7302	25.5077
k	8.6920 (mGal m)	321.3769 (mGal m^2)	16 121 (mGal m^3)
x_0 (m)	–0.6609	–0.5827	–0.6541
$RMSE$ (mGal)	0.0742	0.0153	0.0219
R^2	0.9443	0.9971	0.9944

The lowest one of the three reached values of $RMSE\_V$, $RMSE\_H$ and $RMSE\_S$ with the highest one of the three reached values of R^2_V, R^2_H and R^2_S are obtained for the infinite horizontal cylinder, meaning that, the field residual gravity anomaly could be preferably modeled as an infinite horizontal cylinder. The depth obtained in this case ($z = 17.7302$ m) is found to be in a good agreement with that obtained from drill-hole information ($z = 21$ m) (*Robinson and Coruh, 1988*). The computed gravity anomaly is drawn according to the estimated values of infinite horizontal cylinder model parameters as shown in Fig. 4. The comparison between field and computed anomalies shows a close agreement between them, which certainly attests the validity of the new proposed approach.

3.2. Interpretation of the Karrbo field residual gravity anomaly

Fig. 5 shows a field residual gravity anomaly of a profile 25.6 m length obtained over the two-dimensional pyrrhotite ore, Karrbo, Vastmanland, Sweden (*Shaw and Agarwal, 1990*). The field gravity anomaly is also interpreted by the proposed approach for the three different structures a priori assumed, where the gathered results are summarized in Table 3.

The lowest one of the three reached values of $RMSE\_V$, $RMSE\_H$ and $RMSE\_S$ with the highest one of the three reached values of R^2_V, R^2_H and R^2_S are obtained for the infinite horizontal cylinder, meaning that, the field residual gravity anomaly could be preferably modeled as an infinite horizontal cylinder. The depth obtained in this case ($z = 4.7062$ m) is found to be in good agreement with the depth reported by *Tlas et al. (2005)*

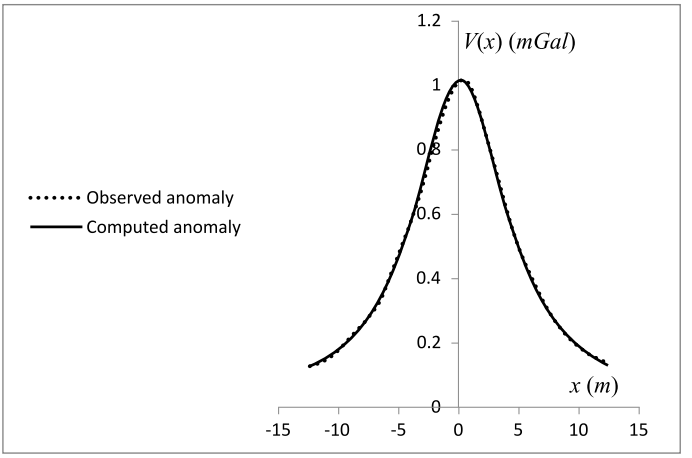

Fig. 5. Residual gravity field anomaly over the two-dimensional pyrrhotite ore, Karrbo, Vastmanland, Sweden. The evaluated curve by the proposed method is presented for an infinite horizontal cylinder model.

Table 3. Interpretation of the Karrbo field residual gravity anomaly, Sweden.

Model parameters	Semi-infinite vertical cylinder	Infinite horizontal cylinder	Sphere
z (m)	1.5839	4.7062	7.057
k	2.1303 (mGal m)	22.5104 (mGal m^2)	331.0846 (mGal m^3)
x_0 (m)	0.1693	0.1772	0.1767
$RMSE$ (mGal)	0.0947	0.0055	0.0279
R^2	0.9252	0.9996	0.9922

($z = 4.82$ m), *Asfahani and Tlas (2015)* ($z = 4.7$ m), *Shaw and Agarwal (1990)* ($z = 5.8$ m), and *El-Araby (2000)* ($z = 5.23$ m). The computed gravity anomaly is drawn according to the estimated values of infinite horizontal cylinder model parameters as shown in Fig. 5. The comparison between field and computed anomalies shows a close agreement between them, which attests the capability and the validity of the new suggested approach.

3.3. Interpretation of the Dehloran field residual gravity anomaly

Fig. 6 shows a field residual gravity anomaly obtained over an area located in West of Iran in the Zagros tectonic zone, Iran (*Abedi et al., 2010*). The

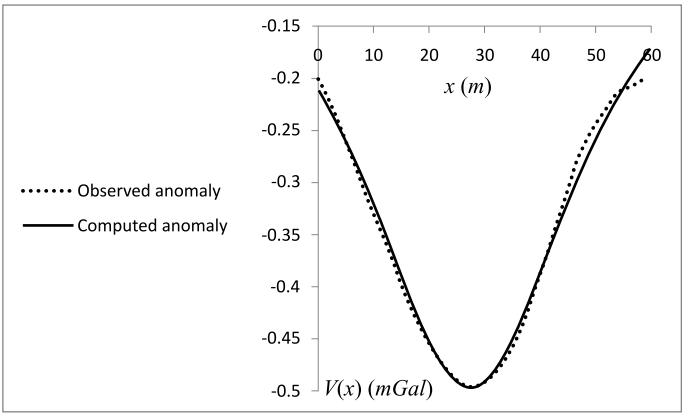

Fig. 6. Residual gravity field anomaly over an area located in West of Iran in the Zagros tectonic zone, Iran. The evaluated curve by the proposed method is presented for an infinite horizontal cylinder model.

field gravity anomaly is interpreted by the proposed approach, where the interpretative results are presented in Table 4.

Table 4. Interpretation of the Dehloran field residual gravity anomaly, Iran.

Model parameters	Semi-infinite vertical cylinder	Infinite horizontal cylinder	Sphere
z (m)	12.7586	23.6345	31.4088
k	–6.657 (mGal m)	–277.2779 (mGal m^2)	–15 142 (mGal m^3)
x_0 (m)	27.1784	27.4276	27.5829
$RMSE$ (mGal)	0.0147	0.0097	0.0122
R^2	0.9814	0.9915	0.9865

The lowest one of the three reached values of $RMSE\_V$, $RMSE\_H$ and $RMSE\_S$ with the highest one of the three reached values of R^2_V, R^2_H and R^2_S are obtained for the infinite horizontal cylinder, meaning that, the field residual gravity anomaly could be preferably modeled as an infinite horizontal cylinder. The depth obtained in this case ($z = 23.6345$ m) is found to be in good agreement with that reported by (*Abedi et al., 2010*), by using three different interpretation methods, the normalized method ($z = 23.73$ m), the least-squares method ($z = 23.3145$ m), the neural network method ($z = 22.8$ m), and also with that obtained from drill-hole information ($z = 23$ m) (*Abedi et al., 2010*).

The computed gravity anomaly is drawn according to the estimated values of infinite horizontal cylinder model parameters as shown in Fig. 6. The comparison between field and computed anomalies shows a close agreement between them, which attests the validity of the suggested approach.

3.4. Interpretation of the Humble field residual gravity anomaly

Fig. 7 shows a field residual gravity anomaly obtained over an area located near the town of Humble in north-eastern Harris County on the Upper Gulf Coast of Texas, USA (*Nettleton, 1962; Abdelrahman and Gobashy, 2017*). The field gravity anomaly is newly reinterpreted by the proposed approach. The results related to this residual gravity anomaly are shown in Table 5.

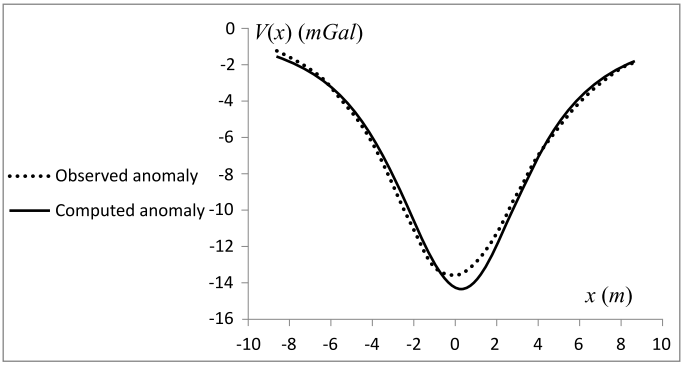

Fig. 7. Residual gravity field anomaly over an area located near the town of Humble in north-eastern Harris County on the Upper Gulf Coast of Texas, USA. The evaluated curve by the proposed method is presented for a sphere model.

Table 5. Interpretation of the Humble field residual gravity anomaly, USA.

Model parameters	Semi-infinite vertical cylinder	Infinite horizontal cylinder	Sphere
z (km)	1.0435	3.2087	4.8192
k	–22.4903 (mGal km)	–159.5463 (mGal km^2)	–1600.2 (mGal km^3)
x_0 (km)	0.1423	0.2517	0.2941
$RMSE$ (mGal)	2.3061	0.7804	0.4319
R^2	0.8329	0.9744	0.9908

The lowest one of the three reached values of $RMSE\_V$, $RMSE\_H$ and $RMSE\_S$ with the highest one of the three reached values of R^2_V, R^2_H

and R^2_S has been obtained for the sphere, meaning that, the field residual gravity anomaly could be preferably modeled as a sphere. The depth obtained in this case ($z = 4.8192$ km) is found to be in a good agreement with that reported by *Nettleton (1962)* and by *Abdelrahman and Gobashy (2017)* ($z = 5.05$ km) using a statistical approach.

The computed gravity anomaly is drawn according to the estimated values of sphere model parameters as shown in Fig. 7. The comparison between field and computed anomalies shows a close agreement between them, which proves the validity of the proposed approach.

3.5. Interpretation of the Wathlingen field residual gravity anomaly

Fig. 8 shows a field residual gravity anomaly obtained over an area situated in the southern part of the North-West German Basin, Germany (*Dubey et al., 2014; Abdelrahman and Gobashy, 2017*). The field gravity anomaly is reinterpreted by the new proposed approach, where the results are shown in Table 6.

The lowest one of the three reached values of $RMSE\_V$, $RMSE\_H$ and $RMSE\_S$ with the highest one of the three reached values of R^2_V, R^2_H and R^2_S are obtained for the semi-infinite vertical cylinder, meaning that,

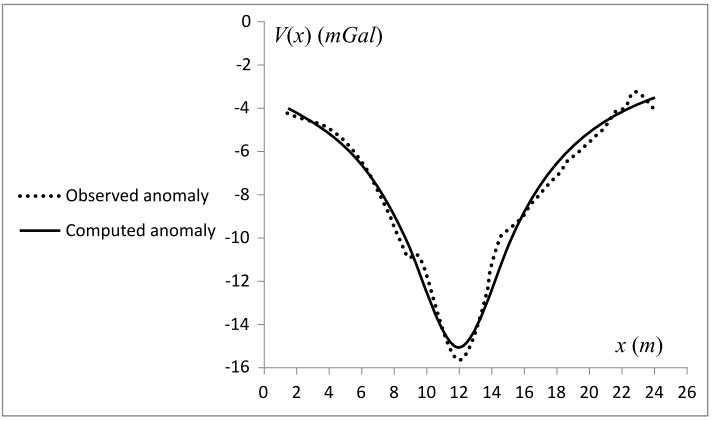

Fig. 8. Residual gravity field anomaly over an area situated in the southern part of the North-West German Basin, Germany. The evaluated curve by the proposed method is presented for a semi-infinite vertical cylinder model.

Table 6. Interpretation of the Wathlingen field residual gravity anomaly, Germany.

Model parameters	Semi-infinite vertical cylinder	Infinite horizontal cylinder	Sphere
z (km)	2.9155	6.2657	8.7195
k	–43.8499 (mGal km)	–541.4824 (mGal km^2)	–8885.5 (mGal km^3)
x_0 (km)	11.9780	12.1696	12.2627
$RMSE$ (mGal)	0.5183	0.9208	1.0871
R^2	0.9828	0.9448	0.9228

the field residual gravity anomaly could be preferably modeled as a semi-infinite vertical cylinder. The depth obtained in this case ($z = 2.9155$ km) is found to be in a good agreement with that reported by *Dubey et al. (2014)* and by *Abdelrahman and Gobashy (2017)* by using a statistical approach ($z = 3.2$ km).

The computed gravity anomaly is drawn according to the estimated values of semi-infinite vertical cylinder model parameters as shown in Fig. 8. The comparison between field and computed anomalies shows a close agreement between them, which proves the validity of the proposed approach.

4. Pseudo-code of the proposed interpretation method

A pseudo-code of the proposed method is explained and illustrated in this section for interpreting residual gravity anomalies related to three different types of structures, e.g., a semi-infinite vertical cylinder, an infinite horizontal cylinder, and a sphere. Such pseudo-code procedure facilitates and aids to put the interpretation method into a computer code.

The statistical criteria of preference Root Mean Square Error ($RMSE$) defined in Eq. (14) and the square of correlation coefficient (R^2) defined in Eq. (15) are used in the proposed method in order to choose the suitable source geometry related to the responsible gravity field anomaly.

The pseudo-code procedure
$V_i\,(Observed)\,,\ i = 1, ..., N$ is the observed data,
q is the shape factor of the buried structure,
$RMSE$ is the root mean square error,
R^2 is the square of correlation coefficient.

begin

for $q = 0.5,\ 1,\ 1.5$ **do**

Find the pair values of $RMSE\_V$, and R^2_V for a semi-infinite vertical cylinder model ($q = 0.5$)
Find the pair values of $(RMSE\_H, R^2\_H)$ for an infinite horizontal cylinder ($q = 1$)
Find the pair values of $(RMSE\_V, R^2\_V)$ for a sphere ($q = 1.5$)
end for
Find the parameters $RMSE = \min\{RMSE\_V, RMSE\_H, RMSE\_S\}$, and $R^2 = \max\{R^2\_V, R^2\_H, R^2\_S\}$
if $RMSE = RMSE\_V$ or $R^2 = R^2\_V$, **then**
the gravity anomaly could be modeled as a semi-infinite vertical cylinder, **end the procedure**
else
the gravity anomaly is not preferably to be modeled as a semi-infinite vertical cylinder, **continue**
end if
if $RMSE = RMSE\_H$ or $R^2 = R^2\_H$, **then**
the gravity anomaly could be modeled as an infinite horizontal cylinder, **end the procedure**
else
the gravity anomaly is not preferably to be modeled as a an infinite horizontal cylinder, **continue**
end if
if $RMSE = RMSE\_S$ or $R^2 = R^2\_S$, **then**
the gravity anomaly could be modeled as a sphere, **end the procedure**
else
the gravity anomaly is not preferably to be modeled as a sphere
end if
end begin
end the pseudo-code

5. Conclusion

The new proposed approach is applied to interpret five real field gravity anomalies from Cuba, Sweden, Iran, USA and Germany, where satisfactory results were obtained.

An acceptable agreement between the results derived by this approach and those obtained by other interpretative methods is shown, which manifests the validity of the proposed approach.

Moreover, the depth obtained by such the new proposed approach is found to be in an acceptable accordance with that obtained by the real field data information.

The new proposed approach could be easily put in MATLAB code or in Excel sheet. It is recommended to apply this method for routine analysis of gravity anomalies for determining the best-estimate values of parameters related to spheres, semi-infinite vertical cylinder and infinite horizontal cylinder-like structures.

Acknowledgements. Authors would like to thank Dr. I. Othman Director General of the Syrian Atomic Energy Commission for his continuous encouragement and guidance to achieve this research. The anonymous reviewers are cordially thanked for their critics, remarks and suggestions that considerably improved the final version of this paper. Dr. Igor Kohut, editor of Contribution to Geophysics and Geodesy Journal is also thanked for his collaboration with the authors during the different stages of publishing this paper.

References

Abdelrahman E. M., Bayoumi A. I., Abdelhady Y. E., Gobash M. M., El-Araby H. M., 1989: Gravity interpretation using correlation factors between successive least-squares residual anomalies. Geophysics, **54**, 12, 1614–1621, doi: 10.1190/1.1442629.

Abdelrahman E. M., 1990: On "A least-squares approach to depth determination from gravity data" by Gupta O. P. (Geophysics, **48**, 357-360, March 1983), discussion. Geophysics, **55**, 3, 376–377, doi: 10.1190/1.1442846.

Abdelrahman E. M., Bayoumi A. I., El-Araby H. M., 1991: A least-squares minimization approach to invert gravity data. Geophysics, **56**, 1, 115–118, doi: 10.1190/1.1442946.

Abdelrahman E. M., El-Araby T. M., 1993: A least-squares minimization approach to depth determination from moving average residual gravity anomalies. Geophysics, **58**, 12, 1779–1784, doi: 10.1190/1.1443392.

Abdelrahman E. M., Sharafeldin S. M., 1995a: A least-squares minimization approach to depth determination from numerical horizontal gravity gradients. Geophysics, **60**, 4, 1259–1260, doi: 10.1190/1.1443857.

Abdelrahman E. M., Sharafeldin S. M., 1995b: A least-squares minimization approach to shape determination from gravity data. Geophysics, **60**, 2, 589–590, doi: 10.1190/1.1443797.

Abdelrahman E. M., El-Araby T. M., El-Araby H. M., Abo-Ezz E. R., 2001a: Three least-squares minimization approaches to depth, shape, and amplitude coefficient determination from gravity data. Geophysics, **66**, 4, 1105–1109, doi: 10.1190/1.1487058.

Abdelrahman E. M., El-Araby T. M., El-Araby H. M., Abo-Ezz E. R., 2001b: A new method for shape and depth determinations from gravity data. Geophysics, **66**, 6, 1774–1780, doi: 10.1190/1.1487119.

Abdelrahman E. S., Gobashy M., 2017: Depth and shape solutions from residual gravity anomalies due to simple geometric structures using a statistical approach. Contrib. Geophys. Geod., **47**, 2, 113–132, doi: 10.1515/congeo-2017-0008.

Abedi M., Afshar A., Ardestani V. E., Norouzi G. H., Lucas C., 2010: Application of various methods for 2D inverse modeling of residual gravity anomalies. Acta Geophys., **58**, 2, 317–336, doi: 10.2478/s11600-009-0053-2.

Asfahani J., Tlas M., 2015: Estimation of gravity parameters related to simple geometrical structures by developing an approach based on deconvolution and linear optimaization techniques. Pure Appl. Geophys., **172**, 10, 2891–2899, doi: 10.1007/s00024-015-1068-z.

Barbosa V. C. F., Silva J. B. C., Medeiros W. E., 1999: Stability analysis and improvement of structural index estimation in Euler deconvolution. Geophysics, **64**, 1, 48–60, doi: 10.1190/1.1444529.

Bowin C., Scheer E., Smith W., 1986: Depth estimates from ratios of gravity, geoid and gravity gradient anomalies. Geophysics, **51**, 1, 123–136, doi: 10.1190/1.1442025.

Collins G. W., 2003: Fundamental numerical methods and data analysis. Case Western Reserve University.

Dubey C. P., Götze H.-J., Schmidt S., Tiwari V. M., 2014: A 3D model of the Wathlingen salt dome in the Northwest Germany Basin from joint modeling of gravity, gravity gradient, and curvature. Interpretation, **2**, 4, SJ103–SJ115, doi: 10.1190/INT-2014-0012.1.

Ekinci Y. L., Balkaya Ç., Göktürkler G., Turan S., 2016: Model parameter estimations from residual gravity anomalies due to simple-shaped sources using Differential Evolution Algorithm. Journal of Applied Geophysics, **129**, 133–147, doi: j.jappgeo.2016.03.040.

El-Araby H. M., 2000: An iterative least-squares minimization approach to depth determination from gravity anomalies. Bull. Fac. Sci., Cairo Univ., **68**, 233–243.

Elawadi E., Salem A., Ushijima K., 2001: Detection of cavities from gravity data using a neural network. Explor. Geophys., **32**, 3-4, 75–79, doi: 10.1071/EG01204.

Fedi M., 2007: DEXP: A fast method to determine the depth and the structural index of potential fields sources. Geophysics, **72**, 1, I1–I11, doi: 10.1190/1.2399452.

Fedi M., Florio G., Quarta T. A. M., 2009: Multiridge analysis of potential fields: Geometric method and reduced Euler deconvolution. Geophysics, **74**, 4, L53–L65, doi: 10.1190/1.3142722.

Gupta O. P., 1983: A least-squares approach to depth determination from gravity data. Geophysics, **48**, 3, 357–360, doi: 10.1190/1.1441473.

Hartmann R. R., Teskey D., Friedberg I., 1971: A system for rapid digital aeromagnetic interpretation. Geophysics, **36**, 5, 891–918, doi: 10.1190/1.1440223.

Jain S., 1976: An automatic method of direct interpretation of magnetic profiles. Geophysics, **41**, 3, 531–541, doi: 10.1190/1.1440631.

Kilty T. K., 1983: Werner deconvolution of profile potential field data. Geophysics, **48**, 2, 234–237, doi: 10.1190/1.1441463.

Ku C. C., Sharp J. A., 1983: Werner deconvolution for automatic magnetic interpretation and its refinement using Marquardt's inverse modeling. Geophysics, **48**, 6, 754–774, doi: 10.1190/1.1441505.

Lines L. R., Treitel S., 1984: A review of least-squares inversion and its application to geophysical problems. Geophys. Prospect., **32**, 2, 159–186, doi: 10.1111/j.1365-2478.1984.tb00726.x.

Mohan N. L., Anandababu L., Roa S. V., 1986: Gravity interpretation using the Melin transform. Geophysics, **51**, 1, 114–122, doi: 10.1190/1.1442024.

Nettleton L. L., 1962: Gravity and magnetics for geologists and seismologists. AAPG Bull., **46**, 10, 1815–1838, doi: 10.1306/BC7438F3-16BE-11D7-8645000102C1865D.

Nettleton L. L., 1976: Gravity and magnetics in oil prospecting. Mc-Grow Hill Book Co., 464 p.

Odegard M. E., Berg J. W., 1965: Gravity interpretation using the Fourier integral. Geophysics, **30**, 3, 424–438, doi: 10.1190/1.1439598.

Robinson E. S., Coruh C., 1988: Basic exploration geophysics. Wiley, New York, NY, 576 p.

Salem A., Ravat D., 2003: A combined analytic signal and Euler method (AN-EUL) for automatic interpretation of magnetic data. Geophysics, **68**, 6, 1952–1961, doi: 10.1190/1.1635049.

Salem A., Smith R., 2005: Depth and structural index from normalized local wavenumber of 2D magnetic anomalies. Geophys. Prospect., **53**, 1, 83–89, doi: 10.1190/1.1635049.

Salem A., Williams S., Fairhead D., Smith R., Ravat D., 2008: Interpretation of magnetic data using tilt angle derivatives. Geophysics, **73**, 1, L1–L10, doi: 10.1190/1.2799992.

Sharma B., Geldart L. P., 1968: Analysis of gravity anomalies of two-dimensional faults using Fourier transforms. Geophysical Prospecting, **16**, 1, 77–93, doi: 10.1111/j.1365-2478.1968.tb01961.x.

Shaw R. K., Agarwal B. N. P., 1990: The application of Walsh transform to interpret gravity anomalies due to some simple geometrically shaped causative sources: A feasibility study. Geophysics, **55**, 7, 843–850, doi: 10.1190/1.1442898.

Silva J. B. C., Barbosa V. C. F., 2003: 3D Euler deconvolution: Theoretical basis for automatically selecting good solution. Geophysics, **68**, 6, 1962–1968, doi: 10.1190/1.1635050.

Thompson D. T., 1982: EULDPH-a new technique for making computer-assisted depth estimates from magnetic data. Geophysics, **47**, 1, 31–37, doi: 10.1190/1.1441278.

Tlas M., Asfahani J., Karmeh H., 2005: A versatile nonlinear inversion to interpret gravity anomaly caused by a simple geometrical structure. Pure Appl. Geophys., **162**, 12, 2557–2571, doi: 10.1007/s00024-005-2775-7.

sciendo

Contributions to Geophysics and Geodesy Vol. 49/3, 2019 (325–354)

Subsurface tectonic characterizations by the use of geo-electrical resistivity technique and their implications on environmental soil and groundwater at Erbil dumpsite, west of Erbil city – Iraqi Kurdistan region

Sirwa Qader Smail GARDI[1,*], Jamal ASFAHANI[2]

[1] Department of Geology, College of Science, University of Salahaddin, Erbil, Kurdistan Region, Iraq

[2] Department of Geology, Atomic Energy Commission of Syria, P. O. Box 6091, Damascus, Syria

Abstract: Twenty seven vertical electrical resistivity soundings (VES), distributed on three profiles, have been carried out around the Erbil city dumpsite location in northern Iraq, by using Schlumberger configuration. The main objective of those VES soundings is to characterize the subsurface structures and to detect the probable soil contamination zones at the dumpsite and the surrounding district. Bai Hassan aquifer in the study region is one of most important natural fresh water in the central sub-basin of Erbil. The 2D Pichgin and Habibulleav technique is applied herein to study and analyse the three VES profiles. Its application in the study region has highly demonstrated the efficacy of such a technique. In fact, the subsurface structures in the study area have been recognized, and the exact position, dip, direction of the faults and groundwater level were also precisely detected. The role of applying this technique together with the available geological information, while carrying out geo-electrical surveys is emphasized to obtain useful, cheap and fast lithological, groundwater table and structural subsurface information.

Key words: VES, Schlumberger, Pichgen and Habibullaev, tectonic, soil, groundwater, dumpsite, Erbil

1. Introduction

Electrical resistivity investigation techniques are widely used for water exploration, to quickly and economically obtain details about the location,

*corresponding author: e-mail: sirwagardi@gmail.com

doi: 10.2478/congeo-2019-0017

depth and resistivity of subsurface formations. Those techniques through making suitable measurements on the surface proved to be very successful in delineating the subsurface geology and structures (*Olasehinde et al., 2013*). Electrical Resistivity techniques are extensively used in the search for suitable groundwater sources, to monitor types of groundwater pollution, in engineering surveys to locate sub-surface cavities, faults and fissures, permafrost, etc., in archaeology for mapping out the areal extent of remnants of buried formations of ancient buildings, amongst many other applications (*Reynolds, 2011*).

The most effective electrical resistivity surveys for groundwater exploration were carried out by applying the traditional Vertical Electrical Sounding (VES), with Schlumberger configuration (*Edwards, 1977; Zohdy et al., 1984*).

The geo-electrical survey has been carried out in the study area to mainly give information concerning the thickness of subsurface layers, geological structures, contributing the groundwater occurrence, lateral and vertical variations of subsurface layers and finally to delineate the contaminated zones which are affected by the wastewater valley.

The study area is characterized by a good potential of groundwater and soil resources. Bai Hassan Formation (formerly Upper Bakhtiari) represents the main water bearing formation in the area. The wastewater valley exists at a lowland area. There is therefore a risk of the soil and wastewater flow to the neighbouring cultivated lands. The wastewater flow may contaminate the shallow subsurface soil. The leakage of water into the underground aquifer also represents serious threats for the population totally dependent on groundwater in this area. The presence of an impermeable layer such as clays fortunately prevents the leakage of wastewater into the underground fresh water aquifer.

The present paper is an important application contribution of the geo-electrical survey together with the use of Schlumberger VES technique, oriented towards clarifying the subsurface structure in the study area, and its implications on environmental aspects (soil and groundwater). The measured VES distributed on three main profiles in the study region, have been integrally qualitatively and quantitatively (in 1D and 2D) interpreted to get the maximum that enable us completing the subsurface pictures for those three profile sections.

The 1D quantitative interpretations aimed at knowing the real resistivities and thicknesses under every studied VES (*Zohdy and Bisdorf, 1989*). The 2D quantitative interpretations include mainly the application of *Pichgin and Habibulleav (1985)* method, enhanced by *Asfahani and Radwan (2007)*. This technique has been successfully applied in Syria for solving different structural subsurface problems related to the groundwater (*Asfahani and Radwan, 2007*), and geo-exploration mining such as phosphate, uranium, sulphur and bitumen (*Asfahani, 2011*). More recently, *Al-Fares and Asfahani (2018)* efficiently applied this 2D technique for solving Abou Barra leakage dam problem in northern Syria, where the results obtained by this technique agree well with those obtained by 2D resistivity tomography.

The 2D *Pichgin and Habibulleav (1985)* technique is considered as the most sophisticated one in determining the subsurface and structural features and oblique contacts between different types of rocks (*Asfahani, 2011*). By using this technique, the interpretation is carried out along a given profile, where a number of VES are distributed along an oriented line.

The traditional 2D interpretations of several VES distributed along a given profile are incapable to give an accurate and integrated subsurface picture. Such a weakness is due to the fact that every VES point is 1D interpreted without considering the effect of other surrounding VES.

The advantages of 2D *Pichgin and Habibulleav (1985)* technique are related to the fact that all the values (resistivity as a function of $AB/2$) of the VES distributed along a given profile are taken into consideration laterally (along the profile) and vertically. This strengthens the interpretation and allows us to determine the subsurface structures and the main tectonic features in the study area.

According to this technique, the non-homogeneity points are laterally and vertically determined, where the analysis of their variations allows determining the main structural features along the studied profile. The results of the quantitative 1D for every interpreted VES existing along the studied profile (True Resistivity and thicknesses) are superimposed on the resulted map of non-homogeneity points. This procedure finally allows getting the complete 2D lithological subsurface model for the study profile.

The main objectives of this paper are therefore constructed to be included (1) carrying out geo-electrical survey in the study area with VES Schlumberger array, (2) interpreting the measured VES points with 1D to

get the real subsurface layers (thickness and resistivity) for every measured VES point in this area, (3) interpreting the VES distributed along a given profile with 2D quantitative interpretation (*Pichgin and Habibulleav, 1985*), (4) determining the subsurface structures in the study area, and (5) examining the probable soil contamination due to the wastewater effect.

2. Location of the study area

The study area is located some 10 km west of Erbil city (Fig. 1). It lies between latitudes 36° 11′ 40.60″ N and longitudes 43° 53′ 05.10″ E, and covers an area of about 7 km^2. The dumpsite is on a hill with an elevation

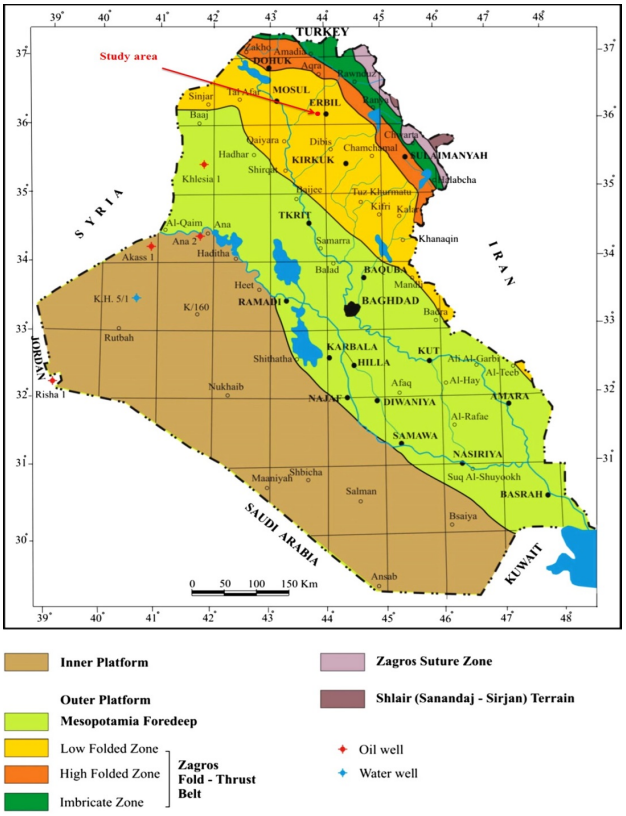

Fig. 1. Main tectonic zones of Iraq (after *Fouad, 2010*).

of ∼435 m above sea level. There are two valleys of septic tank discharge besides of the hill which they intersect at the southern part of the hill which they discharge. The prevailing climatic condition in the area of study is characterized by the diurnal variations, high temperature in summer and cold in winter. The climatic condition is important for waste disposal site, because the wind direction and wind speed have a considerable role in generating storms at these sites. The rate of the rainfall is also one of the most important factors, that runoff on the surface of waste disposal sites, seeping as a leachate through it based on the rate of precipitation, finally contact with the groundwater as a contaminant material.

3. Geological setting

Geomorphologically there are no surface geological features in the study area, except of some hills and valleys, which are controlled by the drainage pattern, reflecting the subsurface structures and the rock unit nature. The Erbil area rises topographically from the flat plains in the west and southwest towards Pimam Mountain in the north and northeast direction (Fig. 2).

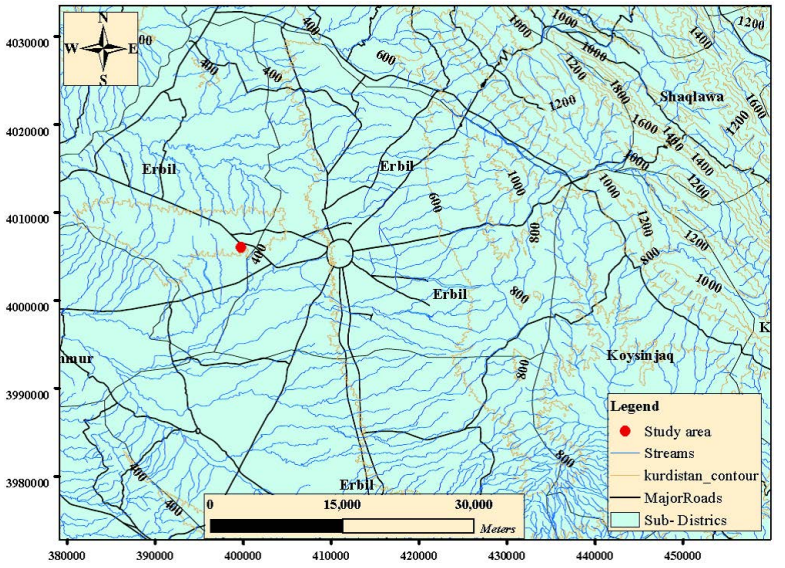

Fig. 2. The study area and topographic map of Erbil province.

The central plain of Erbil slopes gradually from east to west with a slope of $< 3°$ where the local slopes do not exceed 8° (*Hassan, 1998*). The drainage pattern in Erbil area falls into two subdivisions, the whole of the eastern part of the area that drains from the east, and the northeast with a parallel system of streams and valleys toward the central area just west of Erbil city. This is consistent with the general slope of the area west and southwest from the Pirmam Anticlinal Mountain. The western part of Erbil area on the other hand shows dendritic drainage pattern over gentle slopes of the ground (*Ghaib, 2001*).

The geological formations exposed in the study area are Mukdadiya (Lower Bakhtiari) and Bai Hassan (Upper Bakhtiari) formations as well as Quarternary and recent sediments. The Mukdadiya Formation (Pliocene) comprises fining upward cycles of gravely sandstone, sandstone, and red mudstone (*Jassim and Goff, 2006*). The Bai Hassan Formation (Pliocene) which covers most of the study area, consists of molasses sediments represented by alternation of claystones and conglomerates, interbedded with some sandstones and siltstones (*Hassan, 1998*) (Fig. 3). The Quaternary deposits (Pleistocene-Holocene) consists of mixed gravel and clay forming

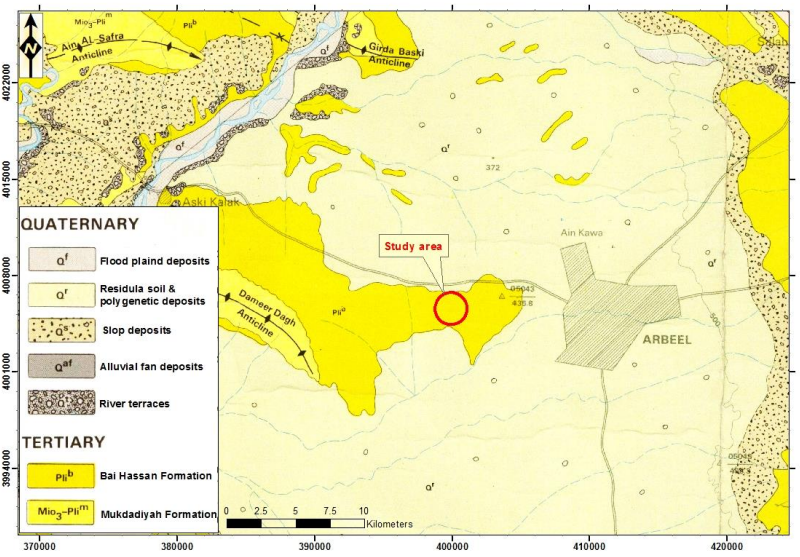

Fig. 3. Geological map showing the study area (after *Sissakian, 1997*).

a sedimentary veneer of polygenetic origin covering large areas in the synclines of the foothill zone (*Jassim and Goff, 2006*).

Structurally, the study area lies within the low folded zone in the stable shelf which is a part of the Arabian Plate, being highly deformed tectonically (*Fouad, 2010*). The deformation intensity normally decreases from northeast towards southwest indicated rom the decrease in the amplitude of the anticlines, with some exceptions in many parts of the involved area. The anticlinal structures in the northeastern part of Iraq have NW–SE trend, which is parallel to the trend of Zagros Fold-Thrust Zone, and extend northwestwards till the Greater Zab River (*Sissakian, 2013*) (Fig. 1). The Erbil area is located on the Kirkuk block (*Ghaib, 2001*). The strata are essentially horizontal with very mild open flexures such as the Erbil trough, and are bounded near the major anticlines by major faults and complicated by many minor faults. The Foothill Zone, especially in the Kirkuk Embayment is characterized by long anticlines with cores of Miocene formations, flanked by very broad and shallow synclines exposing Mio-Pliocene molasse formations along their flanks (*Ghaib, 2001*). The inner parts of the synclines contain Quaternary deposits, referred to here as the polygenetic synclinal fill (*Jassim and Goff, 2006*).

Hydrogeologically, the basin of Erbil is bounded from the north by Greater Zab River and from the south by Lesser Zab River. Erbil basin is a wide depression located between southern limb of Pirmam anticline and Dibaga hill zone which gives a semicircular shape to Erbil basin (*Majeed and Ahmad, 2002*). The Pliocene formations and especially the Bai Hassan, are considered as a major aquifers in the Erbil basin,made up of continental deposit comprising gravel, conglomerate, sand, and clay. The depth of groundwater varies in short distances due to variations in topography. In general, the Erbil Basin is divided into three sub-basins comprising the northern Kapran, the central, and the southern Bashtapa sub-basins (*Habib et al., 1990*). The study area is located in the central sub-basin which covers an area of 1400 km^2. The formations in this sub-basin are the Mukdadiya and Bi Hassan Formations as well as alluvium. According to *Hassan (1998)*, the groundwater table depth ranges between 30 and 50 m in Erbil City, and according to *Al-Ansari et al. (1981)*, the water table is usually 50 m deep. According to *Hassan (1998)*, the groundwater flows from east to west side of the Erbil city, the same flow direction of the regional groundwater.

4. Results

4.1. Geo-electrical resistivity survey

Schlumberger configuration is used in the field with 4 electrodes, two of them A and B are placed to induce an electric current into ground creating a potential field. The other two additional electrodes are used to measure the potential at the same location (Fig. 4). When two current electrodes A and B are used and the potential difference (ΔV) is measured between two measuring electrodes M and N, the apparent resistivity (ρ_a) can be written in the form:

$$\rho_a = K\Delta V/I\,,$$

where K is the geometric factor of Schlumberger electrode configuration, expressed by *Arshad et al. (2007)* as:

$$K = [\pi((AB/2)^2 - (MN/2)^2)/MN]\,.$$

The apparent resistivity (ρ) depends on the geometry of the electrode array used, as defined by the geometric factor (K) (*Reynolds, 2011*).

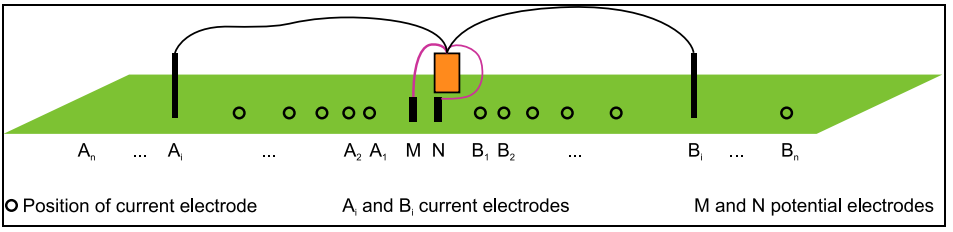

Fig. 4. Sketch of the field setup for a VES in Schlumberger configuration (*Kirsch, 2006*).

The apparent resistivity is a function of the true layers resistivities, their boundaries, and the location of the electrodes. If the substrata are homogeneous, the apparent resistivity is a good approximation of the true resistivity. The interpreted resistivity in terms of various geological formations is based on a resistivity – depth model that reproduces the observed resistivity from a depth sounding (*Asfahani and Radwan, 2007*).

The geoelectrical survey has been adopted in the study area with the purpose of determining the vertical and horizontal distribution of the sedimentary succession, the thickness of the water-bearing layers and detecting

the subsurface geologic structures to clarify their impact on the groundwater and soil. The geo-electrical resistivity survey has been therefore conducted in the study area by applying the conventional Vertical Electrical Sounding method with 27 VES points. The resistivity meters (Terrameter SAS 300C) used for the field measurements directly measures the resistance (R) with high accuracy for each electrode separation.

The current electrode separation (AB) in the Schlumberger configuration applied in the present investigation (Fig. 4) started from 2 m, and increased successively to reach 600–800 m. Such electrode separations were found to be sufficient to reach a reasonable depth range that modelling the aim of the study. Three of these soundings were conducted beside a drilled well in order to parameterize and calibrate the geo-electrical interpretation.

The orientation of the three survey profiles are (Fig. 5):

Profile A–A^{-} extends from NW to SE direction for about 700 m and includes 8 VES points.

Profile B–B^{-} extends from NW to SE direction for about 800 m and includes 9 VES points.

Profile C–C^{-} extends from NE to SW direction for about 900 m and includes 10 VES points.

The sounding spacing was about 100 m; the spreading of electrodes is parallel to the general NW-SE structure direction around the study area, to avoid the influence of dip on the resistivity measurements (*Al-Ane, 1983*).

4.2. Data processing

The geo-electrical sounding curves carried out in the study area have been accurately interpreted using an inverse technique program (*Bobachev et al., 2001*) applied for the 1D qualitative and quantitative interpretation. Fig. 6 shows different examples of field curves along traverses A–A^{-}, B–B^{-} and C–C^{-} interpreted by using this IPI2win (2001) program (*Bobachev et al., 2001*). It is interactive software, graphically oriented, forward and inverses modelling program for interpreting the resistivity curves in terms of a layered earth model.

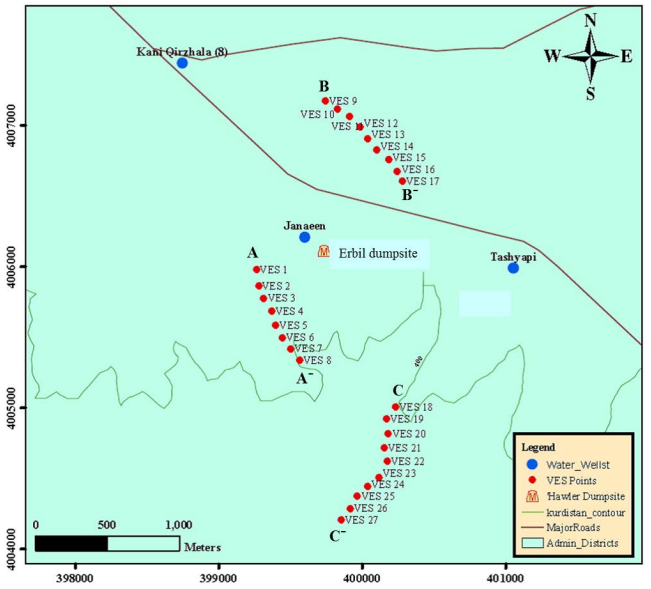

Fig. 5. Map showing the VES points and calibration wells at the study area.

4.3. The Pichgin and Habibullaev technique

This technique is one of the most developed methods used to detect tectonically fractured zones and faults with the determination of their direction and dip amounts through different types of rocks; hence a subsurface 2D tectonic image can be obtained. It can be easily applied to a series of VES points distributed along a given profile. The principle of this technique (Fig. 7) can be summarized as follows: When an electrical current penetrates a planar contact between two different rocks having different resistivities like: ρ_1 and ρ_2, then the electrical field boundary conditions at this contact are characterized as below (*Asfahani, 2011*):

1. If the center point of the vertical electrical sounding is exactly located over a vertical contact between two different formations of different resistivities (ρ_1 and ρ_2), and the electrode array is perpendicular to this contact (Fig. 8a), then the resulting measured resistivity ρ_K is given by the following equation:
   $\rho_K = (\rho_1 + \rho_2)/2\,.$

2. If the array is parallel to such a contact, then the resulting measured resistivity ρ_{IK} is given by the following equation:
$\rho_{IK} = 2(\rho_1\,\rho_2)/(\rho_1 + \rho_2)\,.$

In both of these cases, resistivity is independent of the distances between the two current electrodes, or between the two potential electrodes.

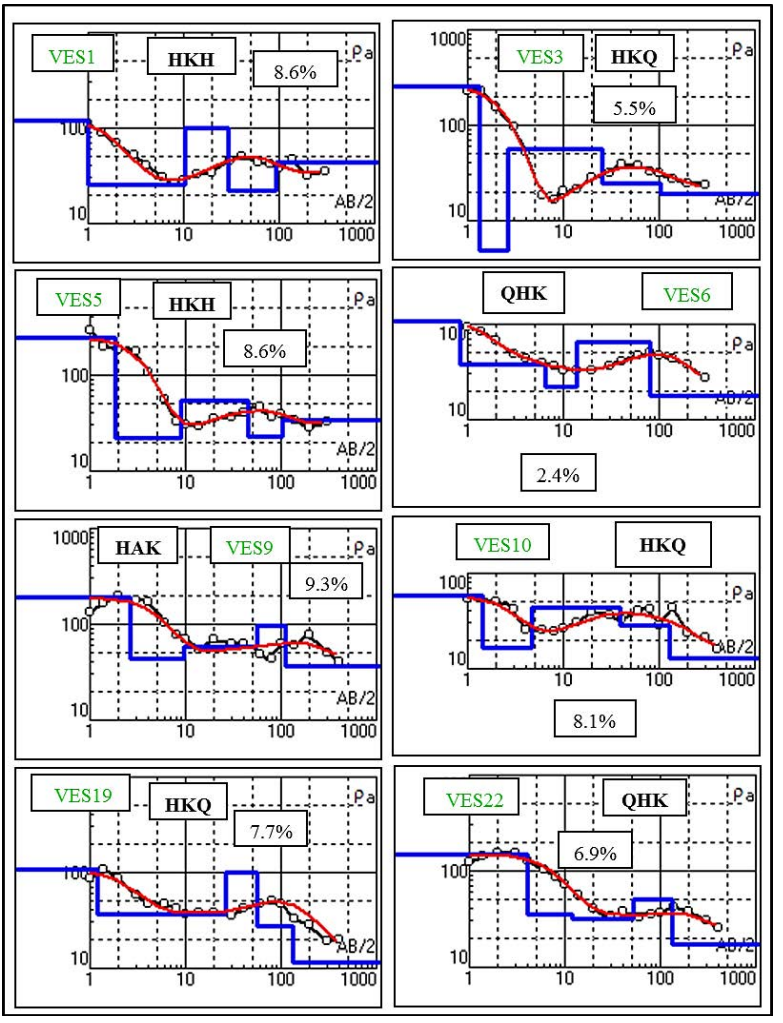

Fig. 6. Examples of field curves along traverses A–A$^-$, B–B$^-$ and C–C$^-$ interpreted by IPI2win (2001) program. VES1: VES point, HKQ: curve type and 8% error percentage.

If two vertical electrical soundings, VES1 and VES2, are performed on either side of a vertical contact, then all profile curves for every given current electrode half-spacing ($AB/2$) will intersect at a point located directly over this vertical contact. The locations of the vertical electrical soundings carried out on a given profile are plotted on the abscissa, and corresponding apparent resistivities (ρ_K or ρ'_K) for each given $AB/2$ are plotted on the ordinate, as shown in Fig. 8.

The intersection points of the curves, that are termed "points of nonhomogeneity" (PNH), are plotted on a 2D (x, y) geological section (Fig. 8c).

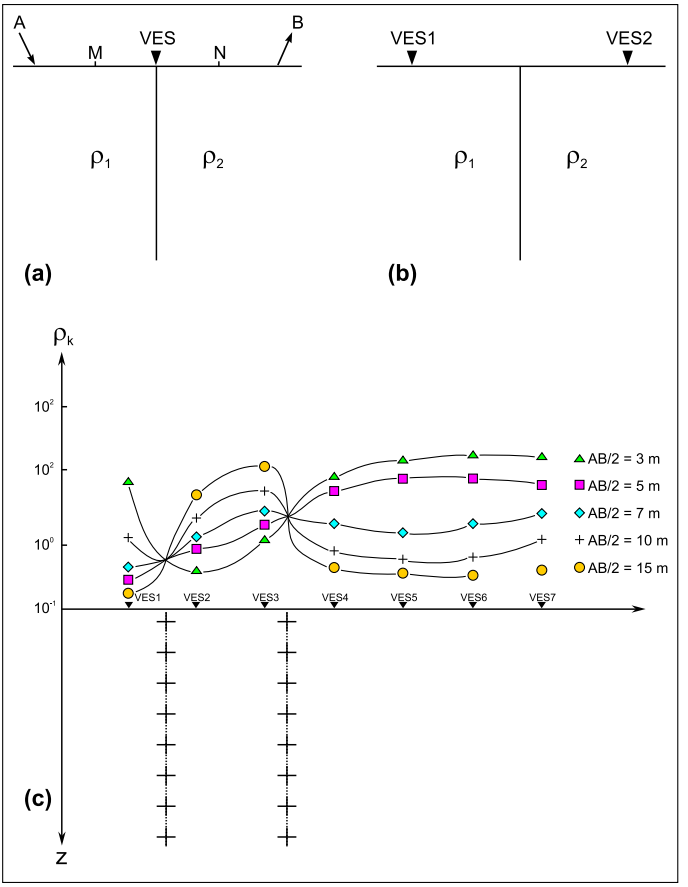

Fig. 7. Principle of Pichgin and Habibullaev method (after *Asfahani, 2011*).

The depth (Z) of each PNH can be determined from to the following equation:

$$Z = [(AB/2)_i + (AB/2)_j]/2\,,$$

where $(AB/2)_i$ and $(AB/2)_j$ are the half-spacings between the electrodes A and B, at which two horizontal curves intersect. The locations of the PNH can be determined using a computer program developed by *Asfahani and Radwan (2007)*. The fractured zones are determined according to the distribution of PNH along the studied profile.

According to the Pichgin-Habibullaev technique, geological interpretation of the PNH is based on the following assumptions:

1. When the PNH are distributed as oblique lines located at shallow depths, they indicate the presence of an inhomogeneous lithological contact.
2. If they are arranged along oblique lines dipping at an angle exceeding 30° at depth, then they represent a fractured zone.
3. If they are scattered randomly near the surface, then they indicate a homogeneous lithology.
4. If they are arranged in regular forms, then they might reflect certain geological structures, such as synclines, anticlines, or horizontally layered strata.

These assumptions have been verified and calibrated through several field tests in Syria involving different lithology and structural architecture (e.g.: *Asfahani and Mohamad, 2002; Asfahani and Radwan, 2007; Asfahani et al., 2010; Al-Fares and Asfahani, 2018*). In particular, *Asfahani and Radwan (2007)* improved this technique to acquire accurate subsurface structural information by taking into consideration the real topographic variations along the studied VES profile.

5. Interpretation of the measured data

The measured data of each VES points have been interpreted qualitatively and quantitatively to delineate the subsurface materials in the study area.

5.1. Quantitative 1D interpretation

The ID quantitative interpretation of the 27 VES curves provided both the true model resistivities and thicknesses of each VES (*Gardi, 2017*). This interpretation has been processed with the use of available calibrated geologic information. The obtained interpretative results are plotted using IPI2win software as shown in figure 6. At the end of data processing and interpretation, the layer parameters (true resistivities and thicknesses or depths) of the various current penetrated layers can be obtained (*El-Sayed, 2010*). The general geologic setting and relevant information have been obtained from three of the generated geo-electrical profiles crossing the study area in different directions (Table 1).

Table 1. The geometry and electrical characteristics of Bai Hassan Formation in the study area.

Layer No.	Ranges of true resistivity (Ω m)	Ranges of thickness (m)	Lithology
1	28–421	0.25–6.19	A thin layer of medium to coarse grained sand and gravel (Top soil)
2	20.3–50.0	22.0–49.0	Sand and silt
3	35.8–99.2	8.0–69	Gravel and sand
4	11.0–50.0	1.0–33.0	Sand silt and clay
5	37.0–322	6.0–96.0	Mixture of gravel, sand, silt and clay
6	11.0–50.0	40.0–101.0	Sand, silt and clay saturated with groundwater
7	10.20–43.7	–	Silt and clay saturated with groundwater

5.2. Quantitative 2D interpretation by *Pichgin and Habibullaev (1985)* technique

Pichgin and Habibullaev (1985) technique is used to get the final subsurface model of each studied profile, where the results of 1D VES interpretations of the VES points distributed along the studied profile are superimposed. The geoelectrical section will show the vertical and lateral distribution of resistivities of subsurface layers. Each layer in the geoelectrical section profile is characterized by its thickness and ranges of true resistivity, that will give an idea of the kind of rock present in the subsurface, and hence, a

model of the subsurface can be prepared (*Oghenekohwo, 2008*).

The resulting geoelectric models are used to produce three geological cross sections: A–A^{-}, B–B^{-}, and C–C^{-}. Each section has its characteristics of true resistivity and depth, its lithology and in structural view, can be interpreted in detail. The generated geo-electric sections reveal that the area is generally characterized by five geo-electric layers.

5.2.1. Pichgin and Habibullaev Profile A–A^{-} (Fig. 8)

The distribution of points of non-homogeneity (PNH) derived by the Pichgin and Habibullaev technique provides information about the subsurface structures and bedded units along the study profile. Three clear faults have been identified in this profile (Fig. 8a); the first one is nearly vertical deep fault which is located almost under VES3 from depth 50 m to 230 m. Another two faults with reverse direction to each other starts from nearly 40 m to 90 m. The non-homogeneity area has been detected which may reflect the burial paleochannel in this section, that is very dominant in the Bai Hassan Formation with a distance of $\sim$200 m and a depth of 60 m which starts from the beginning of the section until VES3.

The pseudo-section showed that at the nearly surface the VES2 and VES7 of this profile are characterized by low apparent electrical resistivity values indicating that this area is affected by the septic tank water. The highly resistive strata under VES3 and VES6 have been noticed (Fig. 8b). There seem to exist a significant fracturing around VES3 and VES6, as these portions have high resistive materials compared to other VES points.

5.2.2. Pichgin and Habibullaev Profile B–B^{-} (Fig. 9)

Nine faults have been detected in the structural view of this section which was interpreted by Pichgin and Habibullaev method. Five of them are deep faults ranging in depth between 20 m to 300 m (Fig. 9a). Seven of these faults start at depth of $\sim$20 m with different lengths and the same direction; the one nearly located under VES9 starts at depth about 180 m to 300 m; while the other one located around VES11 starts from 80 m to 180 m depth. Generally three convex areas have appeared in the beginning, middle and

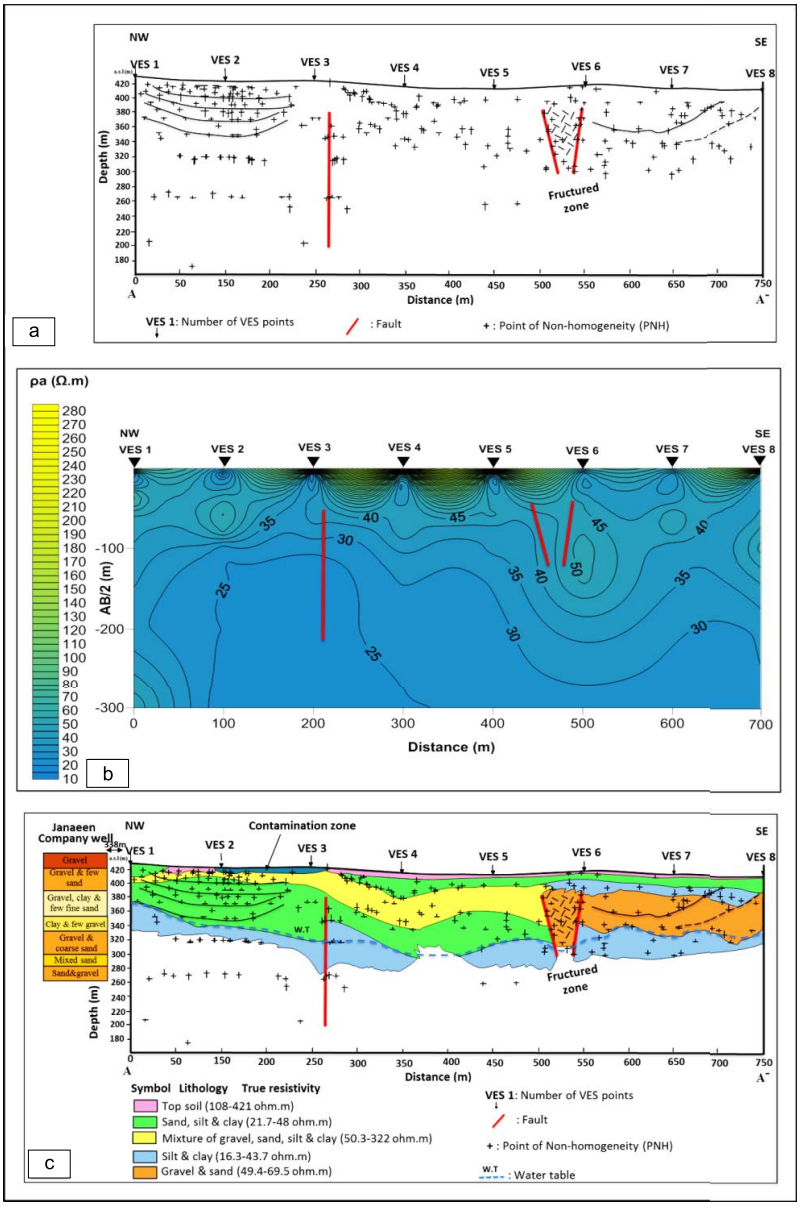

Fig. 8. Three sections along profile A–A˜. (a) Pichgin and Habbullaev non homogeneity points section, (b) pseudo-section, and (c) final geo-electrical section.

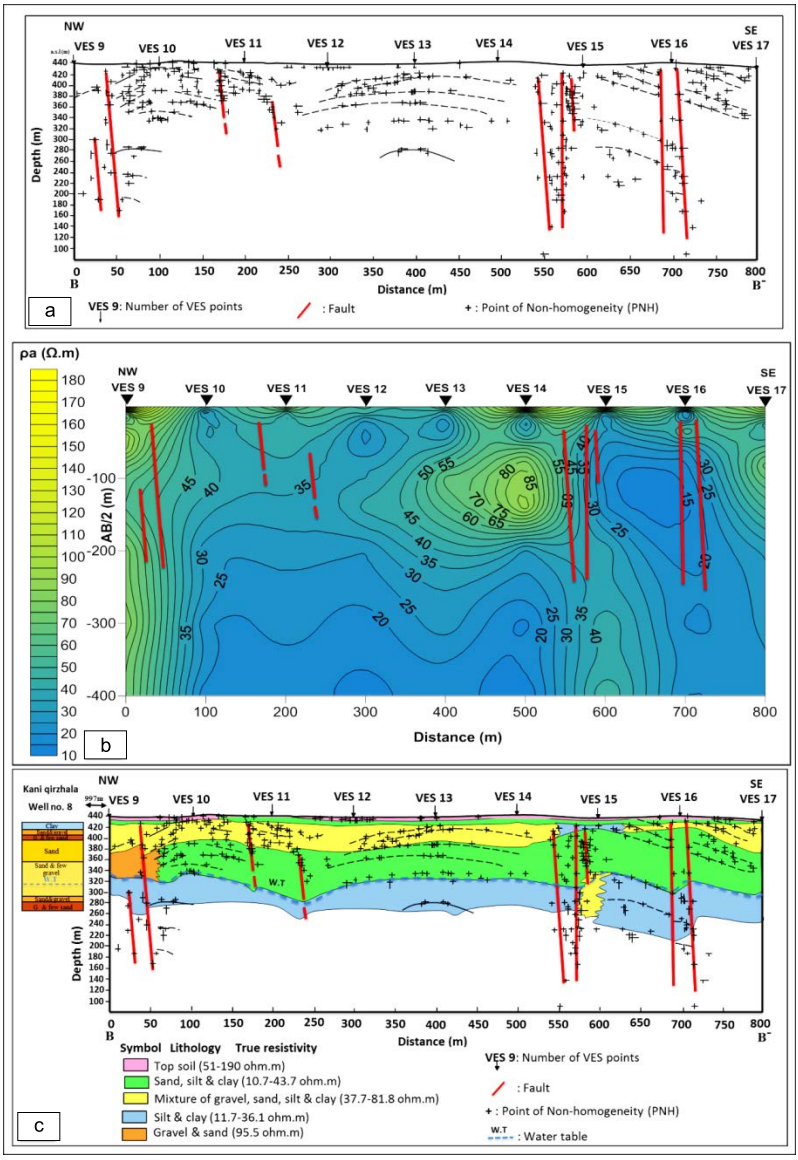

Fig. 9. Three sections along profile B–B-. (a) Pichgin and Habbullaev non homogeneity points section, (b) pseudo-section, and (c) final geo-electrical section.

the last part of the section which have been detected by points of non-homogeneity. These areas mean they are affected during faulting activity and getting bended, which may causes small fractures of the layers.

The pseudo-section has VES points 9, 14, 15 and 17 revealing a uniform increase in resistivity with depth and a comparative medium resistivity throughout the profile too. A slightly closed packing of contour occurs around VES14 and VES7 between 50 m and 150 m depth (Fig. 9b), likely indicating deep fracturing.

5.2.3. Pichgin and Habibullaev Profile C–C^{-} (Fig. 10)

In this profile two different anomalies have been detected at the shallow depth. The first anomaly under VES19 and the second anomaly lie directly under the VES25; they represent the burial paleochannel, which is detected by the points of non-homogeneity with different shapes due to their different lithology. This profile has been affected by the presence of six faults, three of them are located at the left of the section with depth ranging from 130 m to 300, 340 and 380 m respectively, and the other faults are located at the right of the section, which two of them start from 130 m representing and the last one is about 200 m to 360 m (Fig. 10a). The direction of these two set of faults are different otherwise one of them changes its direction with penetrating the depth, under VES20. In the center of this section, the effect of the tectonic activity has been detected (bended), its trace is very clear and not has cut but the faults yet or may affected by the force of the opposite sets of faults.

The pseudo-section showed that faults are also inferred in this profile around VES19, 20 and 26 at depth (Fig. 10b). However, the presence of competent formation at the top to the subsurface and an obvious lack of fracturing may impede percolation of groundwater.

5.2.4. Geological cross sections

Five to seven different geological lithologies have been detected through quantitative interpretation of measured resistivities along three profiles (Table 1).

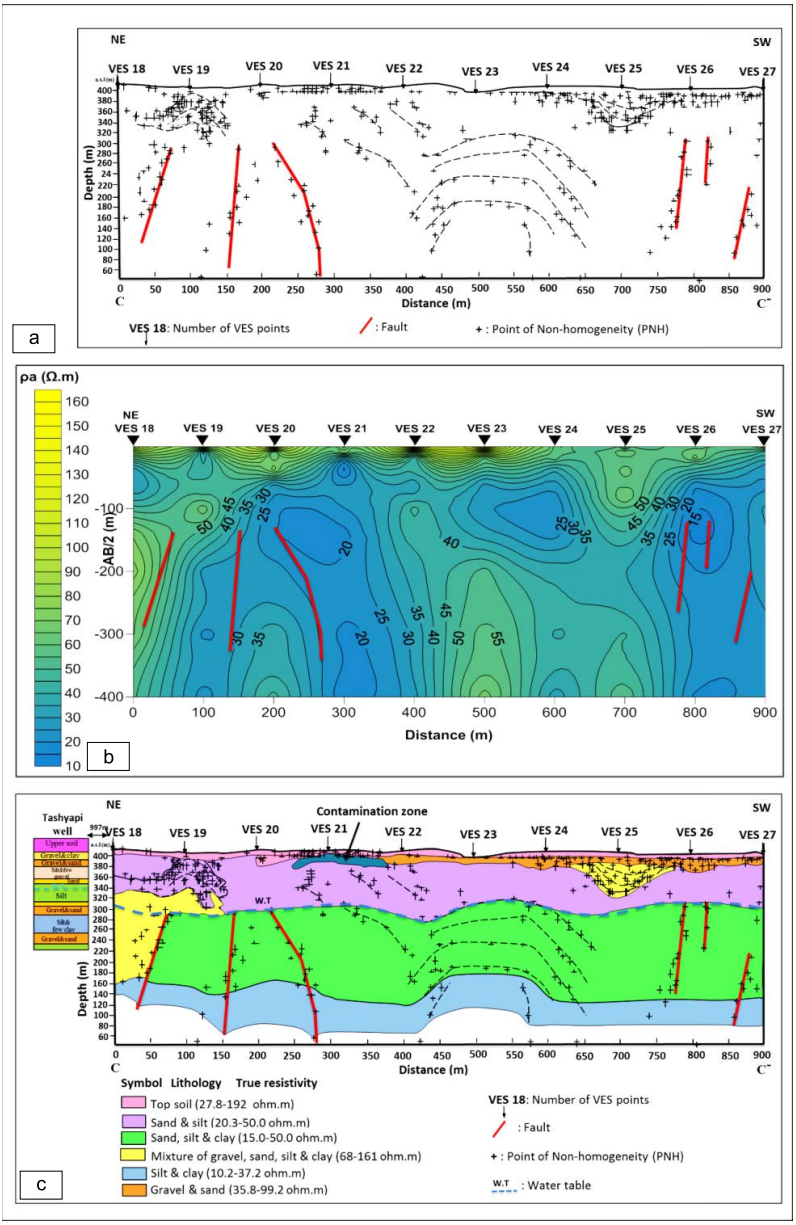

Fig. 10. Three sections along profile C–C⁻. (a) Pichgin and Habbullaev non homogeneity points section, (b) pseudo-section, and (c) final geo-electrical section.

The first layer is a continuous thin surface nearly horizontal geo-electric layer representing the top soil with resistivity ranges of 47–421 Ω m, 51–191 Ω m, and 28–192 Ω m for A–A^{-}, B–B^{-}, and C–C^{-} profiles, respectively. These variations in resistivity value occur due to various types of sediments, fine and medium to coarse grained sand and gravel with variable sizes. The thickness varies from 0.25–1.85 m, 0.5–2.5 m and 0.8–6.0 m (Figs. 8c, 9c, and 10c).

This layer is located in a contaminated area and shows a low resistivity ranging from 3.0–4.0 Ω m under VES2 and VES3 compared to those of the uncontaminated layer outside the disposal site and thickness of 1.0–1.5 m. It is probably contaminated with the septic tanks discharge.

The second geo-electrical layer has resistivity range of 20.3–50.0 Ω m and thickness range of 22.0–49.0 m. It is composed of sand and silt, which was found only in the third profile. A small scale slump folding is identified within this layer under VES19 directly which is detected by the Pichgen and Habibullaev interpretation by NHP representing a style of soft sediment deformation. When sediment on a slope is liquefied, it tends to flow or slide downs the slope even if the slope angle is only few degrees. Various patterns of folding develop; with down slope vergence of the folds takes place, up to few meters in scale. Sometimes these folds are truncated by erosion and overlain by very similar sedimentary material, emphasizing the slight depth of burial of material when it is deformed (*Van Loon, 2009*). The intensity of folding in these narrow zones within otherwise undeformed sequences and the minimum of shearing and fracturing indicate the extreme plasticity, verging on fluidity, of the sediments during deformation (*Gregory, 1969*). A buried paleochannel has been detected within this layer under VES25, which is composed of a mixture of gravel, sand, silt and clay with resistivity range of 67.0–161.0 Ω m and thickness range of 25.0–36.0 m (Fig. 11c).

The third layer has resistivity range of 49.4–69.5 Ω m that represent massive body of highly fractured sand and gravel with thickness range of 50.0–66.0 m toward southeast direction of the study area and was affected by two faults in the reverse direction with each other, from nearly 40–90 m in the first profile (Fig. 8c). The same layer is observed in the second profile under VES9 and has high resistivity value of 95.5 Ω m with ∼69.0 m thickness (Fig. 9c). In the third profile, this third layer is detected as the second

geo-electrical layer having resistivity range of 35.8–99.2 Ω m and thickness range of 8.0–33.0 m from VES22–VES27 (Fig. 10c).

The fourth geo-electrical layer consists of slightly fine grained sediments which have lower resistivity value than the first one ranging from 21.7–48.0 Ω m and 10.7–43.7 Ω m for the A–A$^-$ and B–B$^-$ profiles, respectively. The thickness of this layer ranges from 1.0–18.0 m and 3.0–13.0 m. This thin layer is not identified in the C–C$^-$ profile. The resistivity is diagnostic of fine grained sediments such as sand, silt and clay. In the C–C$^-$ profile a lens with low resistivity value of ∼2.0 Ω m with a thickness of ∼4.5 m beneath VES21 has been detected (Fig. 10c). This lens may represents the contaminated area because it is susceptible to contamination by septic tank discharges.

The resistivity of the fifth geo-electrical layer in the A–A$^-$ profile range from 50.0–322.0 Ω m with a thickness range of 6.0–41.0 m. This layer is composed of a mixture of gravel, sand, silt and clay. The resistivity value under VES2 is too high ∼ 322 Ω m (Fig. 8c), due to increase of the ratio of gravel toward the northwest compared to the other continuous VES points. The resistivity of this geo-electric layer in the B–B$^-$ profile ranges from 37.0–81.8 Ω m and a thickness range of 20.0–58.0 m which thins to ∼20.0–23.0 m under VES16. This layer is composed of a mixture of gravel, sand, silt and clay, and highly fractured due to faulting. It contains a lens of silt and clay of 20.4 Ω m resistivity and ∼ 23 m thickness under VES point 15. Five faults have been noticed within this layer which was also explained in the Pichgen and Habibullaev section (Fig. 10a and c). This geo-electrical layer in the C–C$^-$ profile has a resistivity range of 68.0–161.0 Ω m and a thickness range of 55.0–96.0 m.

The sixth geo-electrical layer of the A–A$^-$ profile has a resistivity range of 21.0–26.0 Ω m and a thickness range of 40.0–76.0 m. This layer consists of sand, silt and clay. The non-homogeneity area has been detected, which may reflect the buried paleochannel within this layer which is very dominant in the Bai Hassan Formation. This paleochannel starts from the beginning of the section until VES3. A fault was detected almost under VES3 from depth 50 m to 230 m. This layer changes laterally in the southeast direction to sand and gravel with sand, silt and clay due to compression process which initiates faulting (Fig. 8c). This layer has been shown also in the beginning of the B–B$^-$ profile (Fig. 9c) with a resistivity range of 11.0–32.0 Ω m and a

thickness of 54.5–101.0 m. It consists of sand, silt and clay which is characterized by highly fractured medium as reflected by non-homogeneity points at the beginning and the middle of the section. While the VES9 has high resistivity value of 95.5 Ω m with ∼69.0 m thickness, may be interpreted as gravel and sand layer. Generally, the tectonic activity that affected this layer is due to its soft sediments. This layer of the C–C^{-} profile is observed with relatively higher resistivity than other geo-electrical sections, ranging from 15–50 Ω m, except under VES point 18 which has 69.0 Ω m resistivity due to change of lithology to a mixture of gravel, sand, silt and clay. This horizon consists of sand, silt and clay which constitute an aquifer of good quality groundwater. The thickness of this aquifer ranges from 55.0–96.0 m depth. This layer has been affected by six faults, three of them are located at the left of the section with depth range of 130 m to 300, 340 and 380 m, respectively; the other three faults are located at the right of the section where two of them start from 130 m and the last one from ∼200 m to 360 m. In the center of this section, the effect of the tectonic activity has been detected (bended), but its trace is very clear and not has cut by the faults yet.

The seventh geo-electrical layer which constitutes an aquifer of groundwater in both profiles A–A^{-} and B–B^{-} has resistivity value ranging from 16.0–43.7 Ω m, 11.7–36.1 Ω m, and 10.2–37.2 Ω m, respectively (Figs 8c and 9c). The thickness of this layer is not defined since it is the last layer. This layer shows lateral lithological variations to coarser material with a resistivity of 61.0 Ω m under VES points 15 representing a mixture of gravel, sand, silt and clay. This layer is also affected by tectonic activity and seven faults have been observed (Fig. 9c).

6. Discussion

The interpretation results of the three geo-electrical sections in the study area indicate the presence of a basin and show successions with variable lithology and thickness. These lithologies reflect the Bai Hassan Formation based on *Buday (1980)* who defined the formation as sediments represented by alternation of clays and conglomerate with some sandstones and siltstones. The successive layers of this formation represent the coarsening upward due to progression processes where many soft structural deformations

were detected and a lot of subsurface structures like faults with different directions and dimensions due to tectonic activity in the study area.

Generally, each studied profile is composed of five layers, the first layer for all those profiles represent the top soil. The second layer represents sand, silt and clay in both first two profiles. Where mixed gravel, sand, silt and clay layer divides this layer. This mixed layer changes to another two layers like silt and clay with a massive body of gravel and sand and very clear two reverse faults in the first profile (Fig. 8c). This layer of gravel and sand was observed in the beginning of the B–B$^-$ profile too (Fig. 9c); while it has shown as a thin layer in the C–C$^-$ profile (Fig. 10c). The gravel and sand layer represent the large paleochannel in such a model. The main layer of sand, silt and clay represents an aquifer in the C–C$^-$ profile which was highly fractured by six faults detected by PNH of *Pichgen and Habibullaev (1985)* method (Fig. 10c).

The last layer composed of silt and clay is representing an aquifer in the study area in both A–A$^-$ and B–B$^-$ profiles (Figs. 8c and 9c). According to *Stevanovic and Iurkiewicz (2009)*, it consists almost entirely of terrigenous clastics made up of silt size to boulder conglomerates eroded and transported from the Zagros Mountains. The successive repetition of the fine-, medium- and coarse- grained textures, and the variation in permeability from one site to another within the same aquifer layer, are typical characteristics of this aquifer. The groundwater level has been detected by the value of resistivity layers and borehole information too, in addition to the *Pichgen and Habibullaev (1985)* method. This gives a clear clue for detecting groundwater level by the absence or discontinuous PNH through the groundwater level (Figs. 8c, 9c and 10c). This technique is very helpful to confirm and detect groundwater level without doubt.

The depth to the top of the aquifer from the surface is approximately ranging from 35.0–129.0 m (Table 2). The deep water table has been detected ranging from 55.0–94.0 m in parts of Erbil city by *Ghaib and Aziz, (2002)*. There is a conducted deeper water table that may be due to the drought condition, which is facing our region since that time.

In this paper, researchers purposely select the mentioned $AB/2$ spacing that are capable to show the effect of contamination, which is related to the environment. We found from the results of geo-electrical resistivity that the contaminated area is characterized by its low resistivity value com-

Table 2. Depth, resistivity and elevation of the top surface of aquifer.

VES No.	Elevation a.s.l. (m)	Depth to the top of aquifer (m)	Elevation of top surface of aquifer a.s.l. (m)	Resistivity of aquifer (Ω m)
VES1	426	94.7	421.3	43.7
VES2	420	75.1	344.9	17.6
VES3	423	102.0	321.0	18.8
VES4	413	102.0	311.0	17.7
VES5	411	102.0	309.0	33.6
VES6	414	80.1	333.9	17.8
VES7	407	83.0	324.0	22.2
VES8	407	83.1	323.9	16.3
VES9	438	111.0	327.0	36.1
VES10	440	127.0	313.0	12.8
VES11	438	127.6	310.4	14.9
VES12	434	127.0	307.0	11.7
VES13	434	128.0	306.0	12.9
VES14	437	116.0	321.0	10.2
VES15	429	131.0	298.0	61.0
VES16	432	126.0	306.0	26.7
VES17	423	129.0	294.0	21.0
VES18	414	76.2	337.8	69.0
VES19	400	56.5	343.5	26.9
VES20	402	53.1	348.9	22.2
VES21	403	42.7	360.3	29.5
VES22	398	52.6	345.4	49.9
VES23	392	58.7	333.3	28.2
VES24	393	43.3	349.7	25.2
VES25	391	35.6	355.4	30.0
VES26	385	41.1	343.9	15.1
VES27	388	36.9	351.1	33.6

pared with the surrounding area. The contamination zone is detected in the geo-electrical sections along A–A^{-} profile under VES points 2 and 3 and C–C^{-} profile under VES21 in the contaminated area by septic tanks. It can flow by infiltration from the surface downward due to the high porosity and permeability of the lithology. If this process is continued, it may come to

contact with groundwater surface and finally contaminate the groundwater. The depth that is subject to contamination from the surface is $\sim$1.0–18.0 m. The contamination zone has not been detected by the geo-electrical section along profile B–B^{-} because it is far away from the dumpsite and septic tank impacts.

Generally, the study area is affected by a number of faults and fractured rock bodies due to the tectonic activity that have been detected by applying Pichgin and Habibuleave technique. 18 faults have been detected, where three faults of them are in the first profile (A–A^{-}), nine faults are in the second profile (B–B^{-}), and the other six faults are in the last profile (C–C^{-}). As it has been seen, the second and third profiles have been more affected than the first one. Most of these faults occur within the fourth layer of the geo-electrical sections that is composed of sand, silt and clay layer saturated with water (aquifer), and extends from the depth of $\sim$50.0–360.0 m. In addition to those areas of non-homogeneity, points were detected in all profiles which may represent the fractured body within the same layer and two clear buried paleochannel in first and third sections with different lithologies and a slump folded structure identified within sand and silt layer in the third profile. These faults and fractured zones have two explanations; one is being a very good area for transmitting groundwater to the main aquifer. They could be at the same time as a passage for percolating contaminated materials and leakages too, coming into contact with groundwater table with time, especially in profiles one and three because they are within the contamination activity and under the great threat for soil too.

7. Conclusions

Based on qualitative and quantitative interpretation of the resistivity data, and constructing 2D section by applying *Pichgen and Habibullaev (1985)* method for three geo-electrical sections in the study area, the following conclusions can be outlined.

1. The presence of a basin and successions distributed alternatively with variable lithology and thickness, vertically and horizontally. The successive layers of these rocks represent the coarsening upward due to

progression processes. This alternation reflects the Bai Hassan formation which is characterized by vertical and lateral variations with good quality of groundwater.

2. Seven layers have been outlined in the study area; these layers are:
   - First layer is a thin surface layer occurs in all profiles representing the top soil with resistivity range of 28–421 Ω m and thickness range of 0.25–6.19 m. The variations in resistivity values are due to various types of materials including fine and medium grained material of sand and gravel.
   - The second layer has a resistivity range of 20.3–50.0Ω m and thickness range of 22.0–49.0 m, comprising fine grained sediments such as silt and sand.
   - Third layer has a resistivity range of 35.8–99.2Ω m and a thickness range of 8.0–69.0 m comprising sand and gravel.
   - Fourth layer has a resistivity range of 11.0–50.0 Ω m and a thickness range of 1.0–33.0 m, comprising sand, silt and clay forming an aquifer for groundwater in profile C–C^{-}.
   - Fifth layer has a resistivity range of 50.0–322.0Ω m and a thickness range 6.0–41.0 m, comprising a mixture of gravel, sand, silt and clay.
   - The sixth geo-electrical layer of the first profile has a resistivity range of 21–26Ω m and a thickness range of 40.0–76.0m comprising sand, silt and clay, and characterized by intense fracturing by many faults in all studied profiles.
   - The seventh layer has a resistivity range of 10.2–61.0 Ω m comprising silt and clay saturated with groundwater in profiles A–A^{-} and B–B^{-} with a lens composed of mixed gravel, sand, silt and clay and has a resistivity of 61 Ω m. The thickness of this layer is not defined since it is the last layer.
3. The septic tank discharges valley has contaminating the soil but no adverse impact on ground water quality is anticipated in the present project. From the results of geo-electrical sections, the contaminated area has very low resistivity compared with the surrounding area. The contamination zone is detected in the geo-electrical section along profile

A–A$^-$ in the region where household septic tanks are discharged. The thickness of this zone is about 1.0–1.5 m with resistivity range of 3.0–4.0 Ω m. In the profile C–C$^-$ a lens is found within the second layer with a resistivity of 2 Ω m and a thickness of 4 m.

4. The detected groundwater tables begins with a sand and clay layer which represents the fifth layer in the first and second geo-electrical sections; while it is composed of sand and silt layer in third section. The average depth from the surface to the top of the aquifer is about 80 m.
5. The application of *Pichgen and Habibullaev (1985)* method played an important role in this study by providing subsurface structures and detecting the exact position, dip and direction of faults and detecting groundwater level. 18 faults have been detected in the study area; most of them are located within the third layer of sand and silt with different lengths and almost at the same direction.
6. A small scale slump folding has been identified within sand and silt layer in the third profile, directly under VES19, which is detected by NHP in Pichgen and Habibullaev section.
7. Based on the points of non-homogeneity (PNH), two buried paleochannels have been identified, which are very dominant in the Bai Hassan Formation. One of them is in the first geo-electrical section and the other is in the third geo-electrical section with different lithologies.
8. Four areas of fractured bodies have been detected as results of Pichgen and Habibullaev interpretation in all sections, due to their effect by tectonic activity within the second and third layers in general.
9. The faults and fractured bodies have a strong disadvantage for percolating contaminations and leakages down reaching the groundwater table in the future in both profiles one and three; however it is still a good aquifer for water.

Acknowledgements. The first author would like to thank Professor Ibrahim Othman, the General Director of Atomic Energy Commission of Syria, for allowing the second author (Professor Jamal Asfahani) to participate in this research. Professor Asfahani has generously shared his experience and thoughts with me throughout this research work to whom I am grateful.

References

Al-Ane J. M. T., 1983: Application of Electrical Resistivity Method for Hydrogeological Problems in Jolak River Basin. Unpublished M.Sc. Thesis, Baghdad University, Iraq, 133 p. (In Arabic).

Al-Ansari N. A., Essaid H. I., Salim Y. N., 1981: Water resources in Iraq. J. Geol. Soc. Iraq, **14**, 1, 35–42.

Al-Fares W., Asfahani J., 2018: Evaluation of the leakage origin in Abu Baara earthen dam using electrical resistivity tomography, northwestern Syria. Geofís. Intl., **57**, 223–237.

Arshad M., Cheema J. M., Ahmed S., 2007: Determination of lithology and groundwater quality using electrical resistivity survey. Int. J. Agric. Biol., **9**, 1, 143–146.

Asfahani J., 2010: Geophysical case study of shallow and deep structures based on traditional and modified interpretation methods: Application to tectonic studies and mineral exploration. Exploration and Mining Geology, **19**, 3-4, 135–152.

Asfahani J., 2011: The Role of Geoelectrical DC Methods in Determining the Subsurface Tectonics Features. Case Studies from Syria, Tectonics, Damien Closson (Ed.), ISBN: 978-953-307-545-7, InTech, Available online: https://www.intechopen.com/books/tectonics/the-role-of-geoelectrical-dc-methods-in-determining-the-subsurface-tectonics-features-case-studies-f, doi: 10.5772/13580.

Asfahani J., Radwan Y., 2007: Tectonic evolution and hydrogeological characteristics of Khanaser Valley, Northern Syria, derived from the interpretation of vertical electrical soundings. Pure Appl. Geophys., **164**, 11, 2291–2311, doi: 10.1007/s00024-007-0274-8.

Asfahani J., Mohamad R., 2002: Geoelectrical Investigation for sulfur prospecting in Techreen structure in northern Syria. Exploration and Mining Geology, **11**, 1-4, 49–59, doi: 10.2113/11.1-4.49.

Asfahani J., Radwan Y., Layyous I., 2010: Integrated Geophysical and Morphotectonic Survey of the Impact of Ghab Extensional Tectonics on the Qastoon Dam, Northwestern Syria. Pure Appl. Geophys., **167**, 3, 323–338, doi: 10.1007/s00024-009-0019-y.

Bobachev A. B., Modin I. N., Shevnin V. A., 2001: IPI2Win Software – user's manual, ver. 2.1. Moscow State University, GeoScan-M Ltd, 25 pp.

Buday T., 1980: The regional geology of Iraq, Vol 1: Stratigraphy and Paleogeography. Publications of Geological Survey of Iraq, Baghdad, 445 p.

Edwards L. S., 1977: A modified pseudosection for resistivity and IP. Geophysics, **42**, 5, 1020–1036, doi: 10.1190/1.1440762.

El-Sayed H. M., 2010: Environmental investigation on Lake Maryut, west of Alexandria, Egypt: geochemical, geophysical and remote sensing studies, M.Sc. Thesis. Alexandria University, Egypt.

Fouad S. F., 2010: Tectonic Map of Iraq, scale 1:1,000,000, 3rd ed. GEOSURV, Baghdad, Iraq.

Gardi S. Q. S, 2017: Integrated Use of Geoelectrical Resistivity and Geochemical Analysis to Assess the Environmental Impact on Soil and Groundwater at Erbil Dumpsite, West of Erbil City – Iraqi Kurdistan Region. ARO-The Scientific Journal of Koya University **5**, 2, 19–31.

Ghaib F. A., 2001: Geophysical Study of the Erbil and Aqra Plains and their Geological Implications. Unpublished Ph.D. Thesis, Salahaddin University, Erbil, 195 p.

Ghaib F. A., Aziz B. K, 2002: A Combination of Electrical Resistivity and Gravity Measurements for Groundwater Prospection in parts of Erbil City. Journal of Duhok University, **6**, 1, 105–111.

Gregory M. R., 1969: Sedimentary features and penecontemporaneous slumping in the Waitemata Group, Whangaparaoa Peninsula, North Auckland, New Zealand. New Zeal. J. Geol. Geoph., **12**, 248–282, doi: 10.1080/00288306.1969.10420236.

Habib H. R., Al-Saigh N. H., Hassan Z. M., 1990: Geochemistry of under groundwater in Erbil City, Iraq. Mosul, Iraq: Mosul University, 173–188.

Hassan E. O., 1998: Urban Hydrogeology of Erbil City Region. Unpublished Ph.D. Thesis, University of Baghdad, Iraq.

Jassim S. Z., Goff J. C., 2006: Geology of Iraq. Published by Dolin, Prague and Moravian Museum, Brno, 341 p.

Kirsch R., 2006: Grounwater Geophysics. A Tool for Hydrogeology. Springer Berlin Heidelberg New York, 493p.

Majeed R. A., Ahmad M. A., 2002: Brief References on Hydrogeological Characters of Erbil Basin. Unpublished Report.

Oghenekohwo F. O., 2008: A comparison of Resistivity and Electromagnetics as Geophysical Techniques. Postgraduate Diploma, 27 p.

Olasehinde P. I., Ejepu S. J., Alabi A. A., 2013: Fracture Detection in a Hard Rock Terrain Using Geoelectric Sounding Techniques. Water Resources Journal, **23**, 1-2, 1–19.

Pichgin N. I., Habibullaev I. K. H., 1985: Methodological Recomendations in studying geo-tectonic conditions of vertical electrical soundings data with application of EC computer for solving hydrogeological and geo-engineering problems, Tashkend (in Russian).

Reynolds J. M., 2011: An Introduction to Applied and Environmental Geophysics. Wiley-Blackwell, 698 p.

Sissakian V., 2013: Geological evolution of the Iraqi Mesopotamia Foredeep, inner platform and near surroundings of the Arabian Plate. J. Asian Earth Sci., **72**, 152–163, doi: 10.1016/j.jseaes.2012.09.032.

Sissakian V. K., 1997: Geological Map of Iraq. 1st edition, Scale 1:250000, Geosurv., Baghdad, Iraq.

Stevanovic Z., Iurkiewicz A., 2009: Groundwater management in Northern Iraq. Hydrogeol. J., **17**, 2, 367–378, doi: 10.1007/s10040-008-0331-0.

Van Loon A. J., 2009: Soft-sediment deformation structures in siliciclastic sediments: an overview. Geologos, **15**, 1, 3–55.

Zohdy A. A. R., Bisdorf R. J., 1989: Schlumberger Sounding Data processing and Interpretation program U. S. Geological Survey, Denver.

Zohdy A. A. R., Eaton G. P., Mabey D. R., 1984: Applications of Surface Geophysics to Groundwater Investigations. Department of Interior U. S. Geological Survey, 3rd Printing. Washington, 116 p., doi: 10.3133/twri02D1.

sciendo

Contributions to Geophysics and Geodesy Vol. 49/3, 2019 (355–371)

Update of the erosive rain factor in Slovakia using data from the period 1961–2009

Milan ONDERKA[1,*], Jozef PECHO[1,2]

[1] Comenius University, Faculty of Mathematics, Physics and Informatics, Department of Astronomy, Physics of the Earth and Meteorology, Mlynská dolina, Bratislava, Slovak Republic SK-823 01

[2] Slovak Hydrometeorological Institute, Jeséniova 12, Bratislava, Slovak Republic SK-831 01

Abstract: An update of the rainfall erosivity factor (R-factor) estimated for 95 locations throughout the entire territory of Slovakia is presented in this paper. We analyzed rainfall time series with 1-minute resolution provided by the Slovak Hydrometeorological Institute. The data cover the period 1961–2009. The rain gauges are located at altitudes ranging from 97 m a.s.l. up to 1322 m a.s.l. and cover the broadest possible range of geographic regions and climatic conditions in Slovakia with reliable rainfall measurements. First, rainfall episodes were isolated by applying the fundamental rule that two subsequent rains are separated by at least six hours of no rainfall. A total of 116,710 rainfall events were identified and analyzed. A rainfall event was classified as erosive if the two following criteria were satisfied: the maximum 15-minute intensity 6.25 mm (i.e. 25 mm hr^{-1}, as originally used in the U.S.L.E. model, and/or rainfall depth was greater than 12.5 mm. The presented estimates of R-factor are based on 18,467 identified erosive rainfall events. Furthermore, the minimum length of rainfall record necessary for reliable estimates of R-factor has been estimated by spectral analysis. The Lomb-Scargle periodogram identified periodic behavior of the total kinetic rainfall energy and rainfall 15-minute intensities. We suggest that these periodicities are attributable mainly to the 11-year Sun spot cycle, the 18.6-year Luni-Solar cycle, and their higher harmonics. The spectral analysis also revealed that in order to capture the temporal variability the minimum length of time-series in calculating R-factors is 14–15 years. We estimate that the long-term mean annual R-factor in Slovakia ranges from 34.8 MJ ha^{-1} cm hr^{-1} (at Gabčíkovo station) to 138 MJ ha^{-1} cm hr^{-1} (at Tatranská Javorina station). The median value of the mean annual R-factors for the whole country is 71.13 MJ ha^{-1} cm hr^{-1}. To our best knowledge, the erosive rain factor has not been updated in Slovakia since the earlier work of Mišík in 1990. This paper is thus an update of the R-factors in Slovakia.

Key words: R-factor, erosive rain, USLE

*corresponding author: e-mail: milan.onderka@posteo.net

doi: 10.2478/congeo-2019-0018

1. Introduction

Soil erosion is considered as one of the major factors disrupting the ability of soil to provide plants with nutrients (*Maderková et al., 2014; Jones et al., 2012; Panagos et al., 2017*). In Europe, the most widespread form of soil degradation is caused by water erosion. It is estimated that some 105 million hectares, which corresponds to 16 % of total Europe's arable land area, are affected by water erosion (*Jones et al., 2012*). According to the recent estimates of soil erosion in the investigated region (*Kročková, 2010*), some 39.65 % (957 173 hectares) are affected by water erosion.

Given the adverse effects of soil loss in agriculture, soil erosion has also other implications for river morphology, siltation of water reservoirs and transport of sediment-bound contaminants (*Onderka et al., 2012*). In central Europe, soil erosion is caused mostly by heavy rainfall episodes. Short-term heavy rains are much more damaging than long-lived and less dramatic rains (*Routschek et al., 2014; Onderka, et al., 2012; Maderková et al., 2014*). *Routschek et al. (2014)* investigated a process-based soil erosion model focusing on changes in erosion rates at high temporal and spatial resolution in three catchments in Germany under simulations of regional climate change using the A1B IPCC-scenario. The outputs from the soil erosion model revealed that, in Germany, the total number of rainstorms is expected to decrease in future while rainfall intensities are likely to increase. *Routschek et al. (2014)* further state that by the year 2050 the number of heavy rainstorms may decrease while rain intensities should increase, and that heavy rainstorms will mostly likely shift from summer to autumn and spring. Updating the R factor is therefore important also in terms of possible effects of climate change on rainfall intensity, volume and incidence.

Wischmeier and Smith (1978) suggested that at least 22 years of record are necessary for reliable estimates of R factors in North America. *Malíšek (1990)* suggested to analyze rainfall time series with a length of at least 15 years, however no explanation supporting this requirement was given. As the rainfall data used in this paper were collected in Slovakia with different climate, the cut-off length of record (22-years) needs to be verified for the local conditions.

As *Prokoph et al. (2012)* reported, the influence of solar irradiance and galactic cosmic ray flux on the precipitation variability has been long considered negligible because of the low power output of the Sun (∼0.1% on

decadal time scales) which can account for a global average temperature change within 0.1 K (*Eddy, 1976*). Sunspot numbers are associated with a change in climate, including severe climatic conditions during the Maunder Minimum characterized by a lack of sunspots that occurred between the years 1640–1705. Terrestrial observations confirm that total solar irradiance increases with the number of sunspots, however, the total solar irradiance is higher at solar maximum even though sunspots are darker (cooler) than the average photosphere. *White and Liu (2008)* explained why the 11-year solar cycle may be viewed as a trigger for El Niño and La Niña events. *Svensmark and Friis-Christensen (1997)* explained that the fluctuation in the cosmic ray flux can be directly related to increases of aerosols and ion-charged raindrops. These mechanisms may be held responsible for the increase in cloud cover and potentially higher precipitation during periods of increased cosmic flux. *Marsh and Svensmark (2000)* found that global cloud cover is negatively correlated with the solar irradiance flux over 11 year sunspot cycles. *Gachari et al. (2014)* claims that the temporal distribution of sunspot numbers indicates that each turning point corresponds to events of severe hydrology in Kenya with a time lag of 5 ± 2 years. Therefore, such events hydrological events can be projected from sunspot forecasts. However, the prediction of sunspots is not an easy task and the current prediction of Cycle 24 appears to be at the end of the Modern Maximum (*Gachari et al., 2014*). *Prokoph et al. (2012)* showed that the 11 year sunspot cycles vary over time (averaging at 10.5 years). Moreover, Sunspot numbers exhibited large variations in their magnitude throughout the second half of the 20th century (*Friis-Christensen and Lassen, 1991*). Also, variability in solar activity such as the 11-year band is not translated linearly into climate functioning but likely through a series of non-linear oceanic-atmospheric responses, such as solar-intensity influence pressure anomaly perturbations and changing wind regimes (e.g. *Hameed and Lee, 2005*). *Nuzhdina (2002)* states that the 11-year and 22-year cycles of solar activity are reflected in the dynamics of many meteorological processes such as atmospheric temperature, pressure and precipitation and that the precipitation in many regions of the Earth correlates with the 22-year cycle better than with the 11-year one. *Prokoph et al. (2012)* investigated the temporal regional influence of 11-year solar radiation periodicities on the maximum annual streamflow in Canada. They found that major runoff extremes are more likely to occur during sunspot

cycles with relatively low sunspot numbers after the last maximum. *Nuzhdina (2002)* found that the 5.3-year oscillation, or the first subharmonic of the 11-year solar cycle is coherent in ENSO and Wolf number data.

To our best knowledge, erosive rain factors have not been updated in Slovakia since the earlier work of *Malíšek (1990)* who processed data from 86 stations. These point-estimates are still used in soil management on the national level using various methods of interpolation (*Šúri et al., 2002*). However, updating Malíšek's estimates of erosive factor in Slovakia requires working with longer rainfall datasets and possibly a denser network of rain gauges (*Šúri et al., 2002*).

We primary goals of this paper ore twofold: (1) to determine the minimum length of rainfall time-series for reliable estimates of R-factors in Slovakia; (2) to update R-factors for the entire territory of Slovakia.

2. Materials and methods

2.1. Climate conditions

The Slovak portion of the Carpathian range exhibits substantial spatial differences in climate. The local climate variability is attributable mainly to rather complex orographic conditions and air circulation patterns. The maritime influence on the local climate is controlled by the Atlantic and Mediterranean Sea. The maritime influence generally decreases from the West towards the East. Cyclones brought by the warm Mediterranean air are responsible for abundant rainfall, particularly in the southwestern and southern parts of the Slovak portion of the Carpathian range. On the other hand, the northwestern and northern parts are affected by cyclones of the Atlantic origin affect (*Melo et al., 2013*). Climatic regions and sub-regions of Slovakia are cold boreal forest climates according to the Köppen's climate classification (*Melo et al., 2013*).

The average yearly rainfall varies from about 520 mm up to 2000 mm in the High Tatras. Rainfall generally increases with altitude at the rate of about 50–60 mm for every 100 meters. About 40 % of the yearly rainfall is observed in summer (June to August); while some 25 % in spring; 20 % in autumn. The remaining 15 % of precipitation falls in winter. The Danube lowlands are among the driest areas of the investigated region with annual precipitation totals of 550 mm.

2.2. Sources of data and Data quality

The rainfall data used in this paper were taken from the national meteorological and climatological databases administered by the Slovak Hydrometeorological Institute. The network of rain gauges consists of 95 stations distributed homogeneously over the investigated area (Table 1). Our input rainfall data cover the "warm" period of the year when precipitation falls in the form as rain (April–October), hence the dormant season (November–March) was not analyzed. Nevertheless, the rain erosion index itself does not account for the erosive forces of thaw and snowmelt anyway (*Wischmeier and Smith, 1978*). The recent effort of the Slovak Hydrometeorological Institute to digitalize older rainfall records, and the subsequent extension of the database, makes it now possible to work with high-resolution data (1-min) from additional stations. The elevations of the meteorological stations range from 97 meters a.s.l. to 1322 meters a.s.l. The length of rainfall time-series used in this study varies between the stations from 14 years up to 49 years (Table 1). Stations with data covering 15 years and less are from the period 1991–2009. Stations with longer time series are based on data from the period 1961–2009.

2.3. Identification of erosive rain episodes

It is known that not every rainfall episode has the potential to cause significant soil erosion – i.e. is not erosive. Several authors discuss the threshold above which a rainfall episode triggers soil erosions (*Hrnčiarová, 2001; Janeček et al., 2012; Kozlovská and Toman, 2016*). A threshold rainfall depth of 12.5 mm was originally introduced for the Universal Soil Loss Erosion model (U.S.L.E.) by *Wischmeier and Smith (1978).* In the Revised U.S.L.E. model, on the other hand, 12.7 mm of total rainfall volume is applied (*Panagos et al., 2017*). Local small-scale field studies conducted by *Hrnčiarová (2001)* suggest that already a 10 mm rainfall may lead to soil erosion. However, for comparative reasons with studies conducted elsewhere in the investigated region (e.g. *Janeček et al., 2012; Kozlovská and Toman, 2016*), and also due to the wide-spread acceptance of the 12.5 mm threshold, we stick to the 12.5 mm threshold in our calculations of R-factors. In terms of maximum intensity of rainfall, we calculate maximum 15-min intensity of 6.25 mm (i.e. 25 mm hr^{-1}), as originally used in the U.S.L.E. model. Erosive

Table 1. List of locations with estimated mean annual R-factors.

Station ID	Location	Elevation [m a.s.l.]	Annual mean of all rainfall episodes [–]	Annual mean of erosive episodes [–]	Annual mean R-factor [MJ/ha cm/h]	Maximum (Annual mean R-factor)	Estimated st. dev. (Annual mean R-factor)	Time-series Length [years]
11020	Tatranská Javorina	1017	75.0	19.0	138.3	319.4	76.7	15
11120	Červený Kláštor	469	68.5	13.0	95.0	188.2	46.8	15
12040	Poprad	693	71.7	10.8	77.8	160.7	46.5	15
12140	Tatranská Lomnica	825	53.9	8.9	60.8	192.3	45.2	15
13100	Podolínec	569	70.8	11.9	79.9	129.0	29.8	15
13220	Plaveč nad Popradom	485	71.6	11.9	108.0	274.7	63.6	14
14050	Holíč	178	65.5	7.8	58.2	141.2	38.1	15
15020	Myjava	348	68.3	9.1	64.3	198.0	42.4	20
15140	Senica	228	61.7	8.4	67.2	159.8	52.3	20
16140	Kuchyňa-Nový Dvor	206	55.8	7.8	53.3	160.4	45.0	17
17100	Bratislava-Mudroňova ul.	205	57.8	8.4	55.2	119.4	25.1	19
17140	Bratislava-Koliba	283	70.1	9.6	68.0	201.5	42.0	15
17300	Komárno	109	56.9	7.9	54.2	146.1	42.0	20
17320	Bratislava-letisko	128	60.9	7.4	43.2	150.4	30.1	20
17400	Malý Javorník	575	53.2	8.6	87.8	459.5	99.1	20
17600	Gabčíkovo	114	47.3	5.7	34.8	117.6	24.3	42
17680	Žihárec	111	62.7	7.9	63.0	153.3	42.7	15
18040	Kráľová pri Senci	121	57.1	6.4	47.5	203.3	47.8	16
18260	Jaslovské Bohunice	176	64.3	8.3	61.9	173.1	42.1	23
18380	Trnava	146	58.8	7.4	60.9	328.3	71.2	18
18560	Sereď	126	49.6	6.9	41.9	151.4	32.3	48
19040	Hurbanovo	115	64.1	8.0	48.1	133.0	30.3	49
20020	Liptovská Teplička	916	64.3	12.3	82.6	179.0	39.3	15
20040	Kráľová Lehota-Čierny Váh	762	62.9	9.3	46.1	126.1	31.4	15
20080	Štrbské Pleso	1322	68.1	12.4	73.4	208.1	34.5	49
20220	Podbanské	978	76.8	13.1	86.1	353.8	79.7	15
20260	Liptovský Hrádok	640	60.6	9.0	48.8	105.1	27.4	43
21130	Liptovský Mikuláš-Ondrašová	570	64.7	8.7	47.0	127.7	31.2	15
21180	Huty	808	52.2	9.6	55.0	101.4	29.5	14
21360	Liptovská Osada	605	63.2	11.6	79.4	138.8	35.1	14
21460	Ľubochňa	444	66.1	11.8	67.6	111.6	29.1	15
22020	Oravská Lesná	785	68.5	13.9	75.5	184.4	32.2	42
22130	Oravské Veselé	754	74.7	10.9	65.5	165.3	41.3	15
23020	Trstená-Ústie nad Priehradou	604	67.3	10.1	57.2	128.8	32.1	14
23060	Vitanová - Oravice	856	66.5	15.3	115.9	312.5	73.0	15
23090	Liesek	690	85.5	14.4	90.2	148.2	29.8	15
23180	Oravský Biely Potok	648	67.5	13.2	81.4	115.2	27.8	15

25040	Žilina	365	72.9	12.1	64.2	137.5	33.0	15
25120	Čadca	432	71.7	11.6	70.0	132.1	31.9	15
25180	Stará Bystrica	478	71.1	14.2	114.3	212.6	56.6	15
25240	Kysucké Nové Mesto	365	66.7	11.1	75.2	174.1	48.6	15
25320	Kunerád	536	74.0	12.5	78.7	194.9	47.2	15
26040	Dolný Hričov	309	72.4	11.2	59.2	116.5	24.6	20
26060	Veľké Rovné	538	64.8	11.1	71.1	156.2	38.3	15
27040	Beluša	253	74.1	11.7	68.7	134.2	31.7	15
28100	Trenčín	295	62.8	9.5	69.2	166.1	40.5	17
28200	Piešťany	161	67.9	9.4	60.3	129.3	25.7	16
30120	Prievidza	256	71.6	9.7	65.6	191.6	40.9	20
30200	Valaská Belá	463	69.0	11.9	86.8	179.2	47.6	15
31040	Topoľčany	176	64.6	8.9	60.8	147.8	32.4	19
31320	Nitra - Velké Janíkovce	132	61.4	8.3	47.4	152.6	34.5	19
31400	Nové Zámky	111	55.0	6.9	46.0	162.7	33.4	48
32200	Mochovce	260	61.5	9.2	57.8	115.4	30.5	20
32280	Podhájska	145	62.3	8.5	51.4	99.4	33.1	16
33020	Telgárt	900	69.8	15.3	93.0	176.6	39.3	15
33200	Brezno	485	71.5	12.0	86.3	257.2	66.3	15
34340	Sliač	310	61.9	8.8	64.0	144.2	36.1	43
35140	Vígľaš Pstruša	365	57.7	9.3	73.8	192.3	48.1	15
36090	Kremnické Bane	763	76.0	11.7	79.3	196.6	44.9	15
36180	Žiar nad Hronom	275	72.4	9.7	61.5	166.3	38.1	15
38120	Boľkovce	210	63.6	10.6	82.5	210.6	60.7	14
39200	Dolné Plachtince	231	63.5	10.7	82.5	175.7	51.9	15
40120	Šahy	145	51.0	8.3	60.6	173.0	50.9	20
40160	Bzovík	351	59.9	9.3	70.7	159.0	41.6	15
40260	Banská Štiavnica	562	68.9	11.4	66.6	166.8	46.7	15
40320	Ladzany	212	66.6	9.9	84.5	200.6	55.4	14
40380	Dudince	137	62.7	10.0	80.4	186.4	52.2	15
43060	Medzilaborce	306	70.7	13.0	89.2	180.8	40.2	15
43100	Čabiny	253	67.4	11.5	84.8	193.2	52.4	15
43160	Osadné	380	64.9	11.3	75.1	177.2	49.7	15
43220	Papin	267	65.3	12.5	87.4	173.7	41.3	15
43360	Snina	211	49.7	9.2	68.2	193.5	51.5	14
43400	Kamenica nad Cirochou	176	72.4	12.2	84.9	157.0	33.3	49
44020	Humenné	145	62.7	10.8	67.3	138.1	33.7	14
46200	Michalovce	110	76.7	10.6	79.0	160.8	40.0	15
48120	Tisinec	208	78.0	12.9	88.0	173.2	40.8	15
49120	Bardejov	312	58.6	8.9	50.1	116.7	25.9	15
49380	Čaklov	140	62.1	10.3	66.0	132.0	39.2	15
50080	Milhostov	102	71.5	10.1	84.7	221.5	62.3	15
51020	Leles	100	62.1	10.0	79.9	195.6	49.6	15
51060	Somotor	97	60.8	8.1	43.1	127.3	32.0	15
52140	Rožňava	311	70.7	11.7	123.2	380.9	89.2	15
53220	Ratková	304	75.5	13.1	126.5	294.9	70.7	15
54120	Lom nad Rimavicou	1018	60.6	11.9	91.4	205.2	51.5	14
54200	Rimavská Sobota	209	66.5	9.1	64.7	127.1	34.4	14
54380	Číž	164	65.3	9.1	67.4	161.4	46.3	15

55020	Štós-Kúpele	599	70.1	12.9	104.8	171.5	40.1	15
55080	Moldava n. Bodvou	206	69.7	10.2	74.3	158.2	36.5	15
56120	Spišská Nová Ves	453	55.5	9.7	73.2	221.8	50.7	15
56200	Spišské Vlachy	382	68.2	11.7	93.6	170.8	41.7	15
57120	Švedlár	477	64.7	12.7	106.3	227.1	54.9	15
57180	Gelnica	357	62.0	11.1	96.0	231.7	56.1	15
58220	Košice-Mesto	207	73.0	10.7	74.1	175.7	44.4	15
59120	Jakubovany	407	72.0	11.3	91.7	184.6	45.0	15
60120	Košice - letisko	229	67.7	10.4	89.9	302.0	54.4	49
	max	1322	85.5	19.0	138.3	459.5	99.1	49
	min	97	47.3	5.7	34.8	99.4	24.3	14
	avrg	389.1	65.6	10.5	73.7	180.3	43.8	19

episodes were identified applying the following criteria: 12.5 mm threshold of total rainfall depth and/or 6.25 mm as maximum 15-min intensity. The separated potentially erosive rain episodes were not divided into segments of equal intensity, as originally proposed by *Wischmeier and Smith (1978)*. Our approach was to consider each measurement interval as a unique rain segment of equal intensity. The database used in this paper consist of time series of rainfall data with 1-minute resolution, hence the length of the rainfall segments equals one minute.

2.4. Calculation of R-factors

For the calculation of the R-factor we used the metric version of the empirical equation developed originally by *Wischmeier and Smith (1978)* and used in its original or modified form i.e. in *Malíšek (1990); Šúri et al. (2002); Janeček et al. (2012); Kozlovská and Toman (2016)*. The R factor was computed from the rainfall measurements collected at 95 locations (Table 1) distributed throughout investigated area.

The erosive factor R is defined as follows:

$$R = \frac{1}{N}\sum_{1}^{N}\left(E_{tot}\, I_{30}\right), \tag{1}$$

where $R\,[\mathrm{MJ\,ha^{-1}\,cm\,h^{-1}}]$ is the rain erosivity factor averaged for a period of length N. The rain erosivity factor is a product of total storm energy E_{tot} (Eq. 2) multiplied by the maximum 30-minute intensity I_{30}. The sum of the storm $E_{tot}\, I_{30}$ values (energy-times-intensity parameter) for a given period is the numerical measure of the erosive potential of the rainfall within that

period. According to *Wischmeier and Smith (1978)*, soil losses are linearly proportional to the $E_{tot}\, I_{30}$ parameter. The product $E_{tot}\, I_{30}$ combines the effects of both the energy and intensity on the erosive potential:

$$E_{tot} = \sum_{i=1}^{n} E_i \,, \tag{2}$$

where E_i is kinetic energy of the i-th rainfall segment. The total kinetic energy of an erosive event is a sum of all rainfall segments n (Eq. 3).

$$E_i = (206 + 87 \log I_S)\, H_S \,, \tag{3}$$

where $I_S\,[\mathrm{mm\,hr^{-1}}]$ and $H_S\,[\mathrm{mm}]$ are the intensity and height of a rainfall segment, respectively.

To answer the question as to how long time series have to be for reliable estimates of erosive factor, we use spectral analysis to decipher the dominant periods in the rain signal. Since rainfall episodes occur isolated in time and are separated by no rain intervals, classical spectral techniques such as the Fast Fourier Transform cannot be used because the treated signal contains gaps. To overcome the problem of unevenly sampled data, we use the Lomb-Scargle periodogram described in *Lomb (1976)* and *VanderPlas (2018)*.

3. Results

Fig. 1 shows how the mean annual occurances of all rain episodes including non-erosive rains are distributed throughout the country. No striking pattern in the geographical distribution of the annual rainfall frequency was observed. On the other hand, as Fig. 2 suggests the least erosive rains fall in the western portion of the country with 5–10 episodes per year. The highest incidence of erosive rains was found to dominate in the central, northern and eastern sections of the country. In terms of the magnitude of R-factors, the highest R-factors were calculated for the mountainous regions (Fig. 3), suggesting a positive correlation between R-factor and altitude.

The summary statistics of erosive events on annual basis is listed in Table 1. We estimate the long-term annual average R-factor to range from $34.8\,\mathrm{MJ\,ha^{-1}\,cm\,hr^{-1}}$ (at Gabčíkovo) to $138\,\mathrm{MJ\,ha^{-1}\,cm\,hr^{-1}}$ (at Tatranská

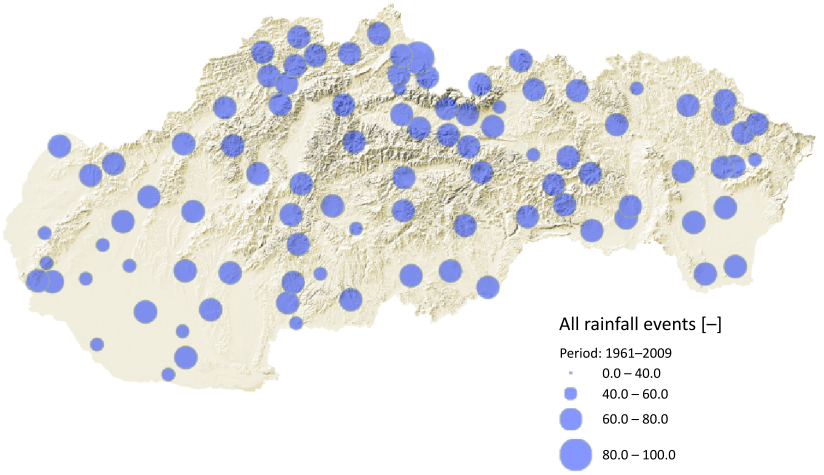

Fig. 1. Long-term mean annual incidence of all rain episodes (including non-erosive rains).

Javorina). As shown in Fig. 4, the point-estimates of the annual mean R-factors are log-normally distributed. The median value of the annual mean R-factors for the whole country is 71.13 MJ ha^{-1} cm hr^{-1}. The mean annual R-factors calculated for the 95 considered locations in Slovakia show a log-normal distribution (Fig. 4).

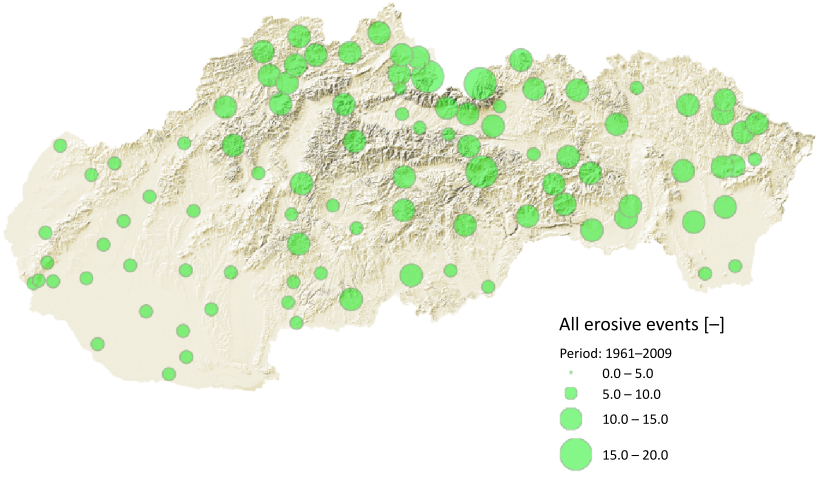

Fig. 2. Long-term mean annual incidence of erosive rain episodes (episodes fulfilling the conditions of 15-min intensity 6.25 mm and/or a total rainfall depth $>$ 12.5 mm).

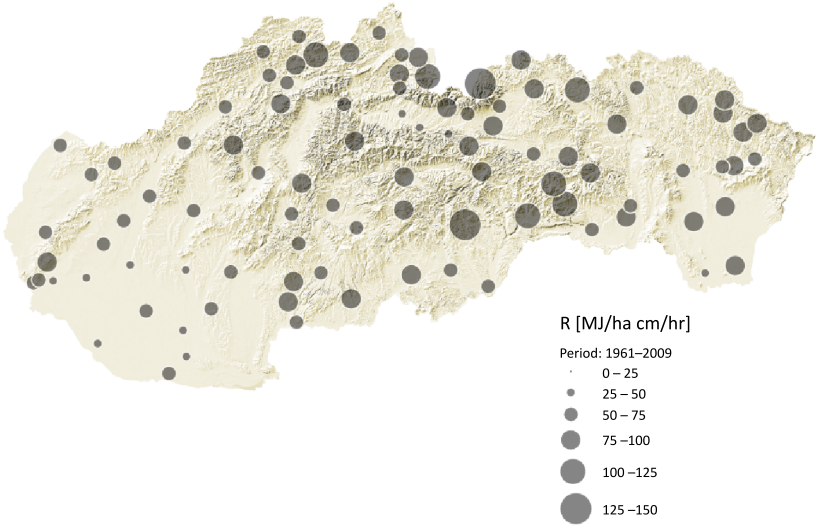

Fig. 3. Long-term mean annual R-factor.

With the Lomb-Scargle periodogram we identified and described six apparent periodicities located at 0.5 year, 1 years, 3–4 years, 7–9 years, 11 years, 22 years in total kinetic energy and maximum 30-minute intensities. This finding is important in terms of choosing the minimum length of

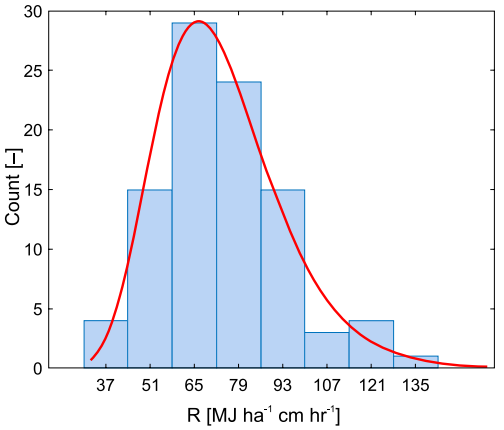

Fig. 4. Histogram of mean annual R-factors estimated for the individual locations listed in Table 1. The R-factors are Log-normally distributed. The median value of the R-factor is 71.13 MJ ha^{-1} cm hr^{-1}.

record when analyzing R factors and their temporal behavior. The individual periodicities (cycles) are labeled in Fig. 5 as letters "A" though "G". Periodicities of 0.5 and 1-year origin in the annual cycle of rainfall and its 0.5-year sub-harmonics (labeled as A–B). Periodicities in the range 3 to 4 years (label C) are probably related to either QBO or the higher harmonics of the 11-year Sunspot cycle at 3.7 years. Periodicities located within the range 7 to 9 years (label D) are probably related to the 7.4 harmonic that result from the combination of the Sun's 11-year and 22-year cycles. Periodicities in the range 10.7 to 11.1 years (label E) originate in the Sun spot cycle. Periodicities in the range 17.9 to 19.6 (label F) are attributed to the 18.6-year Luni-Solar cycle. Periodicities in the range 32 to 34 years (label G) have not been related to any physical phenomena, nevertheless, these periodicities are small compared to top other cycles in the presented spectra in Fig. 5a,c. The spectrogram of maximum 30-min intensities is shown in Fig. 5b, where only the annual and its half-year sub-harmonics are visi-

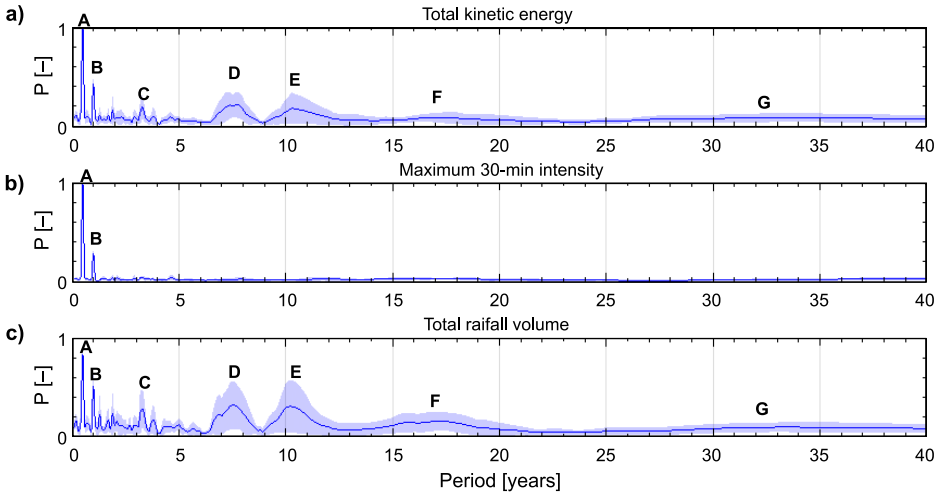

Fig. 5. Normalized power spectra of the Lomb-Scargle periodogram generated for: a) total kinetic energy (Eq. 2) of all registered rainfall episodes; b) maximum 30-minute intensities of all registered rainfall episodes; c) total rainfall volume of all registered rainfall episodes. The bluish areas indicate the spread (upper and lower quartiles) of the spectra generated form 10 station with the longest period of record (>40 years). The solid lines indicate the medians of the processed spectra. The major cycles are indicted as letter A through G at the corresponding periods. The power spectra were normalized to range from 0 to 1 as $[\mathrm{P} - \min(\mathrm{P})]/[\max(\mathrm{P}) - \min(\mathrm{P})]$, where P is the power.

ble. The spectrograms show that the greatest amount of signal variability is located at periods below approximately 13–14 years. This implies that the minimum length of rainfall time-series is approx. 14–15 years. Longer time-series would contain additional signal from the 18.6-year Luni-Solar cycle.

4. Discussion

Erosive rain factors have not been updated in Slovakia since the early 1990s when *Malíšek (1990)* processed data from 86 stations. Our primary objective was to update the estimates of R-factors using more recent data from additional stations. In addition, the results presented in this paper are derived from high resolution 1-minute rainfall data and are published for a total of 95 locations for the first time. *Malíšek (1990)* suggested to analyze rainfall time series with a length of at least 15 years, however no explanation supporting this requirement was given. Our spectral analyses confirm that at least 14 years of rainfall data are needed to capture the 11-year Solar cycle in rainfall data. As *Gusev et al. (2004)* state, the existence of decadal and bi-decadal periods in rainfall data is an evidence of solar activity's effect on the Earth's climate, and that examples of this correlation are short-lived events such as solar flares; up to the 11-year, the 22-year Hale cycle, and possibly even longer solar radiation changes. Further periodicities that have been identified in rainfall, as described in *Ramachandra Rao et al. (2003)*, are located at 4 to 6 years and are attributable to 6-year ENSO cycles, which another 5.5 year sub-harmonic cycle of the Sun spots. *Ramachandra Rao et al. (2003)* described a 6.9-year periodicity and attributed this to the interaction of the 11-year sunspot cycle and the 18.6-year Lunar-Solar cycle. The spectra presented in our paper suggest that the 6.9-year cycle is very small and is detected only in the total rainfall volume series.

The summary statistics of erosive events on annual basis is listed in Table 1. We estimate the long-term annual average R-factor to range from 34.8 MJ ha^{-1} cm hr^{-1} (at Gabčíkovo) to 138 MJ ha^{-1} cm hr^{-1} (at Tatranská Javorina). The median value of the annual mean R-factors for the whole country is 71.13 MJ ha^{-1} cm hr^{-1}.

The Rainfall Erosivity Database at European Scale has been lately published providing maps of R-factors for Europe including the region inves-

tigated in our project *Ballabio et al. (2017)*. The R-factors calculated by *Ballabio et al. (2017)* seem to be within the range of R-factors presented in this paper. The range of annual R-factors calculated for the 95 locations (Table 1) is from 34.8 to 138.3 $\mathrm{MJ\,ha^{-1}\,cm\,hr^{-1}}$ (Table 1). The R-factors calculated in this paper seem to be somewhat higher than the values published in the earlier work of *Malíšek (1990)* who calculated annual mean R-factors within range of 5 and 30 $\mathrm{MJ\,ha^{-1}\,cm\,hr^{-1}}$. One possible explanation of these differences might be the fact that *Mališek (1990)* selected erosive events manually, whereas we deployed an automatic selection procedure. Another explanation is that we used 1-min resolution data. Also *Maderková et al. (2014)* and *Antal et al. (2015)* calculated R-factors for selected sites near the city of Nitra, Slovakia with higher values than those presented in *Malíšek (1990)*.

5. Conclusions

We have identified several dominant periodicities that are attributable to major climatic indices including the Solar activity affecting the long-term behavior of R-factor. This information has implications for reliable estimates of R-factors for stations with short rainfall measurements. We can conclude that the spectral analysis revealed that in order to capture the most of the temporal variability in rainfall signal, the minimum length of time-series for R-factor calculations is 14–15 years. Longer time series might give more precise results as the 22-year Hale's cycle constitutes additional signal variability.

To our best knowledge, erosive rain factors have not been updated in Slovakia since the early 1990s. The results presented in this paper are derived from high resolution 1-minute rainfall data and are published for a total of 95 locations for the first time. For instance, *Malíšek (1990)* processed data from 86 stations. As such, our results have the potential to substantially improve the regional estimates of soil erosion rates in the investigated region and to adjust erosion control measures.

We have updated the estimates of annual R-factors in a climatically and geographically complex region of Slovakia for rainfall data covering the period 1961–2009. We estimated the long-term annual average R-factor to

range from 34.8 MJ ha^{-1} cm hr^{-1} (at Gabčíkovo) to 138 MJ ha^{-1} cm hr^{-1} (at Tatranská Javorina). The median value of the annual mean R-factors for the whole country is 71.13 MJ ha^{-1} cm hr^{-1}.

Finally, we are convinced that the peer researchers and other soil erosion experts will find the updated point-estimates of R-factors in Slovakia interesting to improve soil erosion estimates. As our database cover the years 1961–2009, it would be interesting for the future research to further work on extending the length of time series and focus on potential effects of climate change on the erosive potential of rainfall.

Acknowledgements. This work was supported by the "Science and Research" Operational Program, Project: "Applied research of methods for determination of climatological and hydrological design quantities", ITMS: 26220220132, co-financed by the European Regional Development Fund.

References

Antal J., Maderková L., Eimo J., Drgoňová K., 2015: Analysis of calculation methods for determination of rain erosivity for Slovak Republic. Acta Sci. Pol. Formatio Circumiectus, **14**, 4, 5–14.

Ballabio C., Borrelli P., Spinoni J., Meusburger K., Michaelides S., Beguería S., Klik A., Petan S., Janeček M., Olsen P., Aalto J., Lakatos M., Rymszewicz A., Dumitrescu A., Tadić M. P., Diodato N., Kostalova J., Rousseva S., Banasik K., Alewell C., Panagos P., 2017: Mapping monthly rainfall erosivity in Europe. Sci. Total Environ., **579**, 1298–1315, doi: 10.1016/j.scitotenv.2016.11.123.

Eddy J. A., 1976: The Maunder Minimum. Science, New Series, **192**, 1189–1202.

Friis-Christensen E., Lassen K., 1991: Length of the solar cycle: An indicator of solar activity closely associated with climate. Science, **254**, 5032, 698–700, doi: 10.1126/science.254.5032.698.

Gachari F., Mulati D. M., Mutuku J. N., 2014: Sunspot numbers: Implications on Eastern African rainfall. S. Afr. J. Sci., **110**, 1–5, doi: 10.1590/sajs.2014/20130050.

Gusev A., Martin I., Mello M. G., Pankov V., Pugacheva G., Schuch N., Spjeldvik W., 2004: Bidecadal cycles in liquid precipitations in Brazil. Adv. Sp. Res., **34**, 370–375, doi: 10.1016/j.asr.2003.03.048.

Hameed S., Lee J. N., 2005: A mechanism for sun-climate connection. Geophys. Res. Lett., **32**, 1–3, doi: 10.1029/2005GL024393.

Hrnčiarová T., 2001: Ecological optimization of agricultural landscape (Dolná Malanta model area) (Ekologická optimalizácia poľnohospodárskej krajiny (modelové územie Dolná Malanta)). VEDA, ISBN 80-224-0664-3, pp 134. (in Slovak).

Janeček M., Květoň V., Kubátová E., Kobzová D., 2012: Differentiation and regionalization of rainfall erosivity factor values in the Czech Republic. Soil Water Res., **7**, 1, 1–9, doi: 10.17221/2/2011-SWR.

Jones A., Panagos P., Barcelo S., Bouraoui F., Bosco C., Dewitte O., Gardi C., Erhard M., Hervás J., Hiederer R., Jeffery S., Lükewille A., Marmo L., Montanarella L., Olazábal C., Petersen J.-E., Penizek V., Strassburger T., Tóth G., Van Den Eeckhaut M., Van Liedekerke M., Verheijen F., Viestova E., Yigini Y., 2012: The State of Soil in Europe – a Contribution of the JRC to the European Environment Agency's Environment State and Outlook report SOER 2010. European Environment Agency, Institute for Environment and Sustainability, ISBN 978-92-79-22806-3, doi: 10.2788/77361.

Kozlovská S., Toman F., 2016: Occurrence of erosion-effective rain in the Brno area. Acta Univ. Agric. Silvic. Mendelianae Brun., **64**, 1583–1591, doi: 10.11118/actaun201664051583.

Kročková B., 2010: Soil as an environmental component of the Slovak Republic in 2010 (Pôda ako zložka životného prostredia v Slovenskej republike k roku 2010). Banská Bystrica. Indication Report 2010. Slovenská agentúra životného prostredia Banská Bystrica (Slovak Environmental Protection Agency), pp 45, (in Slovak).

Lomb N. R., 1976: Least-squares frequency analysis of unequally spaced data. Astrophys. Space Sci., **39**, 447–462, doi: 10.1007/BF00648343.

Maderková L., Antal J., Čimo J., 2014: Statistic and probability characteristics of rain factor R in Slovak Republic. Eurasian J. Soil Sci., **3**, 4, 254–259, doi: 10.18393/ejss.15688.

Malíšek A., 1990: Evaluation of the rainstorm erosion efficiency factor (Zhodnotenie faktora eróznej účinnosti prívalovej zrážky). Geogr. časopis, **42**, 4, 410–422 (in Slovak).

Marsh N., Svensmark H., 2000: Cosmic rays, clouds, and climate. Space Sci. Rev., **94**, 1–2, 215–230, doi: 10.1023/A:1026723423896.

Melo M., Lapin M., Kapolková H., Pecho J., Kružicová A., 2013: Climate Trends in the Slovak Part of the Carpathians. In: Kozak J., Ostapowicz K., Bytnerowicz A., Wyzga B. (Eds.): The Carpathians: Integrating Nature and Society Towards Sustainability. Environmental Science and Engineering. Springer, Berlin, Heidelberg, doi: 10.1007/978-3-642-12725-0_10.

Nuzhdina M. A., 2002: Connection between ENSO phenomena and solar and geomagnetic activity. Nat. Hazards Earth Syst. Sci., **2**, 83–89, doi: 10.5194/nhess-2-83-2002.

Onderka M., Krein A., Wrede S., Martínez-Carreras N., Hoffmann L., 2012: Dynamics of storm-driven suspended sediments in a headwater catchment described by multivariable modeling. J. Soils Sediments, **12**, 620–635, doi: 10.1007/s11368-012-0480-6.

Panagos P., Borrelli P., Meusburger K., Yu B., Klik A., Jae Lim K., Yang J. E., Ni J., Miao C., Chattopadhyay N., Sadeghi S. H., Hazbavi Z., Zabihi M., Larionov G. A., Krasnov S. F., Gorobets A. V., Levi Y., Erpul, G., Birkel C., Hoyos N., Naipal V., Oliveira P. T. S., Bonilla C. A., Meddi M., Nel W., Al Dashti H., Boni M., Diodato N., Van Oost K., Nearing M., Ballabio C., 2017: Global rainfall erosivity assessment based on high-temporal resolution rainfall records. Sci. Rep., **7**, 4175, doi: 10.1038/s41598-017-04282-8.

Prokoph A., Adamowski J., Adamowski K., 2012: Influence of the 11 year solar cycle on annual streamflow maxima in Southern Canada. J. Hydrol, **442-443**, 55–62, doi: 10.1016/j.jhydrol.2012.03.038.

Ramachandra Rao A., Hamed K. H., Chen H.-L., 2003: Nonstationarities in Hydrologic and Environmental Time Series. Springer Netherlands.

Routschek A., Schmidt J., Kreienkamp F., 2014: Climate change and soil erosion catena Impact of climate change on soil erosion — A high-resolution projection on catchment scale until 2100 in Saxony/Germany. Catena, **121**, 99–109, doi: 10.1016/j.catena.2014.04.019.

Šúri M., Cebecauer T., Hofierka J., Fulajtár E., 2002: Soil erosion assessment of Slovakia at a regional scale using GIS. Ecology (Bratislava), **21**, 4, 404–422.

Svensmark H., Friis-Christensen E., 1997: Variation of cosmic ray flux and global cloud coverage–a missing link in solar-climate relationships. J. Atmos. Solar-Terrestrial Phys., **59**, 11, 1225–1232, doi: 10.1016/S1364-6826(97)00001-1.

VanderPlas J. T., 2018: Understanding the Lomb-Scargle Periodogram. Astrophys. J. Suppl. Ser., **236**, 1, 16, 28 p., doi: 10.3847/1538-4365/aab766.

White W. B., Liu Z., 2008: Non-linear alignment of El Niño to the 11-yr solar cycle. Geophys Res. Lett., **35**, 19, L19607, doi: 10.1029/2008GL034831.

Wischmeier W. H., Smith D. D., 1978: Predicting Rainfall Erosion Losses: A guide to Conservation Planning. Science, US Department of Agriculture Handbook, No. 537, Washington DC.

sciendo

Contributions to Geophysics and Geodesy Vol. 49/3, 2019 (373–390)

Local tectonic deformations measured by extensometer at the eastern foothills of the Alps at the Sopronbánfalva Geodynamic Observatory, Hungary

Gyula MENTES*, Márta KISZELY

Geodetic and Geophysical Institute, Research Centre for Astronomy and Earth Sciences, Hungarian Academy of Sciences,
Csatkai E. u. 6–8, 9400 Sopron, Hungary

Abstract: In Hungary, at the foot of the Eastern Alps, in the Sopronbánfalva Geodynamic Observatory (SGO), a quartz-tube extensometer has been used for recording the Earth's tides and local tectonic deformations since 1991. The 27-year long strain record (1991–2017) shows a continuous compression of the rock with changing rate. The relations between the measured local deformation and present-day tectonics in the region of the observatory were investigated. The local strain rate variations were also compared with the temporal and spatial distribution as well as with the magnitudes of earthquakes occurred within 200 km from the observatory in two sectors around the azimuth of the extensometer (116°): 116°±15° and 296°±15°. Our investigations show that earthquakes can also influence the strain rate. Earthquakes to the west of SGO generally increase the compressive strain rate, while earthquakes in the Pannonian Basin, with some exceptions, have no significant effect on the local strain rate variations measured in the SGO. It has been found that the recorded compressive strain is in good accordance with the recent tectonic processes in the region of the SGO determined by Global Navigation Satellite System (GNSS) technology and geophysical measurements. From the results it can be concluded that the uplift of the Alps, tectonic processes in the East Alpine region and in the Pannonian Basin play the most important role in the changing local compressive strain rate.

Key words: earthquake; extensometer; tectonic deformation; varying strain rate

1. Introduction

Besides the global deformation measurement techniques as the Very Long Baseline Interferometry (VLBI) measurements (e.g. *Ward, 1994; Krásná et al., 2013, 2015; Plank et al., 2014*), GNSS technology (e.g. *Caporali et al.,*

*corresponding author: tel.: +36-99-508382, e-mail: mentes@ggki.hu

doi: 10.2478/congeo-2019-0019

2008, 2009) and the Persistent Scatterer Interferometry Synthetic Aperture Radar (PSInSAR) technique (e.g. *Massonnet and Feigl, 1998; Burgmann et al., 2000; Hanssen, 2001*) the high resolution extensometric measurements are also used for observation of local tectonic deformations in some observatories (e.g. *Sato and Harrison, 1990; Varga and Varga, 1994; Onoue and Takemoto, 1998; Takemoto et al., 2006*). GNSS and PSInSAR techniques are also suitable for local deformation measurements, but the temporal and deformation resolution of extensometers are much better than that of the PSInSAR and GNSS technologies. In addition to the tectonic deformations extensometers also record short periodic deformations caused by Earth' tides and the recorded data are influenced by different effects depending on the properties of the instruments and the local conditions of the measurement site (*Harrison, 1976; Sato and Harrison, 1990; Venedikov et al., 2006*). A large number of authors deal with the influence of the construction and the surroundings of the instrument's site appearing as cavity, topographic and lithologic effects (e.g. *Farrell, 1972; Harrison, 1976; Brimich et al., 1998; Gebauer et al., 2009, 2010*). The deformations caused by the atmospheric pressure and temperature variations also depend on the properties of the observation site. A lot of publications deal with the effect of atmospheric pressure loading on horizontal deformation measurements (e.g. *Müller and Zürn, 1983; Rabbel and Zschau, 1985; Sun et al., 1995; Dal Moro and Zadro, 1998; Kroner et al., 2005; Steffen et al., 2006; Zürn et al., 2007*). To obtain real tectonic deformations the above mentioned disturbing effects must be corrected.

In the SGO at the foot of the Eastern Alps a quartz-tube extensometer has been recording local tectonic deformations and Earth' tides since 1991. The strain record shows a compression with varying rate. In this paper the relationships between the measured local strain and recent tectonic processes in the Eastern Alps and in the Pannonian Basin as well as the direct effect of earthquakes on the strain rate variations are investigated.

2. Observation site and the instrument

The SGO is located in the Sopron Mountains which belong to the extensions of the Eastern Alps (Alpokalja region). The Sopron Mountains consist of metamorphic rocks of Palaeozoic age such as gneiss and different mica schists

(*Haas, 2001*). The observatory is an artificial gallery driven into an outcrop of the muscovite gneiss (*Kisházi and Ivancsics, 1985*). The rock cover above the observatory is about 60 m. The location of the SGO and the main faults (*Síkhegyi, 2002; Brückl et al., 2010*) in the region of the observatory are shown in the Fig. 1. The coordinates of the SGO are 47° 40' 55" N, 16° 33' 32" E and it is 280 m a.s.l. The observatory and its surroundings are described by *Mentes (2012)* in detail.

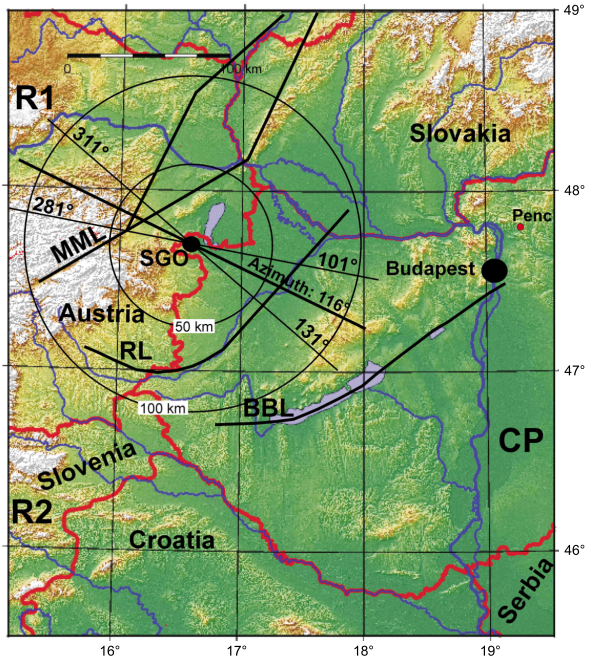

Fig. 1. Location of the SGO and the main faults in its region. MML, RL, BBL are the Mur-Mürz, Rába, and the Balaton-Bodrog lines, respectively. R1, R2 and CP are the regions where the recent tectonic rates were investigated on the basis of GPS data.

The temperature in the gallery, where the extensometer is placed, is very stable. Its yearly mean value is 10.4 °C and the yearly and daily temperature variations are less than 0.5 °C and 0.05 °C, respectively, therefore the direct effect of temperature on the instrument is negligible. Temperature and air pressure variations cause rock strain variations at the site and in the surroundings of the observatory that interfere with tidal and tectonic deformations, and therefore need to be corrected (*Mentes, 2000, 2012*).

The quartz-tube extensometer with a capacitive sensor has a length of 22 m. Its azimuth is 116° so it is nearly perpendicular to the main fault system in its surroundings (Fig. 1). A built-in magnetostrictive actuator is used for regular calibration of the instrument. The soundness of the quartz tube and the stability of the scale factor of the extensometer are checked once a day by the built-in calibrator. Since the parameters of the magnetostrictive actuator may also change, the extensometer is yearly calibrated by means of a portable calibrator which is calibrated by a laser interferometer in the laboratory of the institute before and after of the in-situ calibration of the extensometer in the observatory. The scale factor of the extensometer is $2.093 \pm 0.032\,\mathrm{nm\,mV^{-1}}$ or $0.095 \pm 0.001\,\mathrm{nstr\,mV^{-1}}$ (1 nstr = 10^{-9} relative extension = measured displacement/length of the extensometer). The error of the yearly calibrations and the amplitude variations of the daily calibration impulses are within the error range of the scale factor determination. *Mentes (2010)* describes the construction and calibration of the instrument in detail.

3. Seismicity of the investigated region

The Carpathian Basin is situated in the territory between the Mediterranean area – which is seismically one of the active regions – and the Carpathian Mountains belt. The area is tectonically rather complicated, and the distribution of earthquake epicentres shows a rather scattered pattern (*Bus et al., 2009*). The most active seismic regions near to the SGO are the Mur-Mürz and the Central Pannonian zones (see Fig. 1). The Mur-Mürz zone running from Mura valley to the western Carpathians is the junction of the Eastern Alps and the Pannonian Basin. The tectonics of the Pannonian Basin is caused fundamentally by the northward movement and counter clockwise rotation of the Adria microplate also known as the "Adria-push". Due to ongoing convergence between the European Plate from the north and the Adriatic plate from the south, crustal blocks extrude laterally to the east into the Pannonian Basin (*Brückl et al., 2010; Caporali, 2009; Bada et al., 2007a,b; Decker et al., 2005; Fodor et al., 2005*).

Focal mechanism results in the Pannonian Basin are more diverse although thrust and strike-slip faulting seem to be dominant. NNE–SSW

and NE–SW directions of maximum horizontal stresses are prevailing. The focal mechanism findings in the Eastern Alps show that the majority of the tectonic movements have strike-slip mechanisms with NNW–SSE and N–S directions, but NE–SW directions are nonetheless occasionally observed (*Bada et al., 2007a; Tóth et al., 2008; Olaiz et al., 2009*).

The seismicity of an area can be characterized by the number of earthquakes, their magnitudes and the spatial location of earthquakes and by the released energy. Fig. 2 shows the epicentre map of earthquakes around the SGO between the coordinates 45.5° N, 13.5° E – 49.5° N, 19.5° E from 1991 to 2017

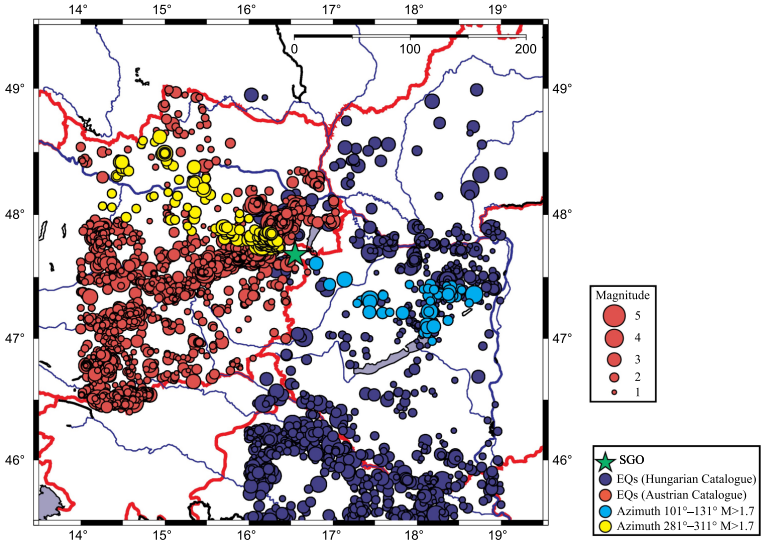

Fig. 2. The seismicity map around the SGO (green star) between the years 1991 and 2017 (*Tóth et al., 1996–2018; Gráczer et al., 2012–2016; ZAMG, 2018*).

4. Methods and data processing

Since the extensometer is also used for tidal monitoring, the stability of the instrument can also be demonstrated by the stability of the measured tidal parameters. Yearly measured extensometric data were corrected for temperature and barometric pressure and then subjected to tidal analysis using the ETERNA 3.40 tidal processing program package (*Wenzel, 1996*). The tidal processing of the data is described by *Mentes (2012)* and *Bán*

et al. (2018) in detail. While the calibration only provides information on the stability of the instrument, the amplitude factors (measured/theoretical amplitudes) for the main lunar diurnal O1 and the semidiurnal M2 waves were used to check the stability of the attachment of the extensometer to the rock and the state of the rock in the vicinity of the instrument. The obtained average value of the yearly determined O1 (0.65 ± 0.07) and M2 (1.08 ± 0.11) tidal factors show clearly that the fixation of the instrument to the rock and the properties of the rock in the vicinity of the observatory did not change during the registration period.

The "drift" remaining after the correction of the extensometric raw data for seasonal effects can be assumed as tectonic movement and deformation. For investigation of the long-term tectonic movements, the annual raw data were concatenated into a 27-year long data series. A polynomial of 9th order was fitted to the long strain data series to eliminate the short periodic and seasonal variations.

The temporal and spatial distribution of seismicity was investigated around the SGO up to 200 km distance. For that purpose, we used the data of the Hungarian Earthquake Bulletins ranging in time from 1995 to 2017 (*Tóth et al., 1996–2018; Gráczer et al., 2012–2016*), which are the most complete catalogues for the smallest events between the 45.5°–49.5° N 16°–23° E territory. For western and northern side of the investigated regions we used the Austrian Earthquake Catalogue (*ZAMG, 2018*). Since the extensometer is sensitive to displacements in its azimuth, firstly we examined the seismicity of this region in two 30° wide sectors around the SGO. The centre azimuths of the sectors were 116° and 296°. The number of earthquakes (EQs), and the released energy for different distances from the SGO were determined. The energy of EQs was calculated according to *Gutenberg and Richter (1942)*. The number of earthquakes and the released energy are both very important features of an area. If energy is only taken into account, the largest few EQs will be only emphasized, without the yearly variation of seismicity. If we ignore the energy, the annual number of the EQs presents mainly the development of the seismological station network or the aftershocks sequences. We have chosen a magnitude threshold $M \geq 1.7$ because earthquakes of this magnitude were already reliably recorded 30 years ago. We expected that the yearly number of these EQs mirrors mainly the changing of the seismicity.

5. Results

5.1. Results of the extensometric measurements

The Fig. 3 shows both the measured "raw" strain data and the fitted polynomial between 1991 and 2017. We also calculated the yearly average strain rates by fitting a line to the yearly extensometric data (Fig. 4a). It can be seen that the compressive strain rate is increasing rapidly between 1993 and 2001, then rate has slowed down and from 2014 it is less than $2\,\mu\,\mathrm{str\,y}^{-1}$.

5.2. Results of the investigation of the earthquakes' effects

The seismicity of the two 30° wide sectors (116°±15°, 296°±15°) around the SGO was different both in activity and yearly variations. The activity is partly reflected by the number of events and the released energy. Table 1 contains the number of EQs, and the released energy for different distances from the SGO. The 116° ±15° sector was more active than the opposite (296° ±15°) since there occurred about twice as many earthquakes of M $\geq$ 0.1. In the sector of 296° ±15° up to 200 km distance there occurred about three times more earthquakes of M $\geq$ 1.7 than in the 116° ±15° sector. But within 100 km from the SGO, there were twelve times more earthquakes of M $\geq$ 1.7 in the 296° ±15° sector than in the opposite. The released

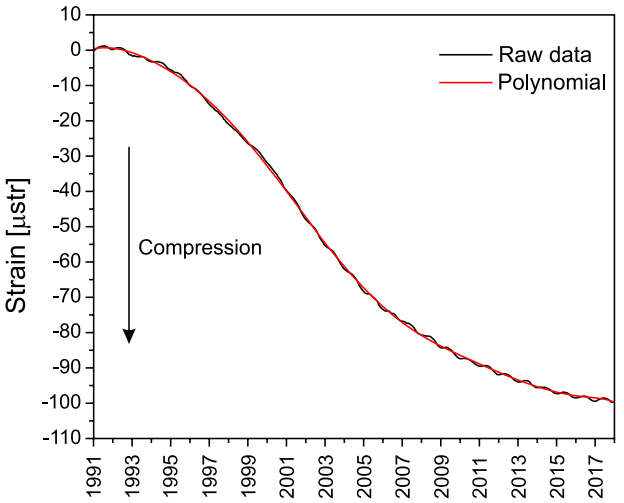

Fig. 3. Rock strain measured in the SGO between 1991 and 2017.

energy by earthquakes was almost four times more up to 200 km distance around the SGO, and within 100 km was ten times more in the 296° ±15° sector than in the opposite. The Figs. 4b–g show the smoothed number and the total and smoothed energy of EQs. The smoothed values are the three year moving average of the number and energy of EQs. The Fig. 4b shows the yearly distribution of EQs M ≥ 1.7 in the sector 116° ±15° and Fig. 4c shows the released energy of EQs M ≥ 1.7 within R = 200 km from the SGO. Figs. 4d–e show the yearly distributions of earthquakes and the released energy for the opposite side. Since the extensometer is sensitive to displacement in its azimuth we also investigated the effect of EQs in a narrow sector around its azimuth (116° ±4° and 296° ±4° and within 30 km distance from the SGO. The Figs. 4f–g show the number of EQs and the released energy. It can be seen that some active years occurred in both sectors in the 27-year observational period. The sector 296° ±4° up to 30 km distance around the SGO was more active than the opposite side.

Table 1. The seismicity of the investigated area around the SGO.

Investigated area	Number of EQs $M \geq 0.1$	Number of EQs $M \geq 1.7$	Max. Richter magnitude	Energy of EQs $M \geq 0.1$ [GJ]
within 200 km from SGO and between azimuths: 101°<116°<131°	558	50	3.7	60.4
within 100 km from SGO and between azimuths: 101°<116°<131°	28	10	3.5	18.4
within 200 km from SGO and between azimuths: 281°<296°<310°	379	168	4.0	229.2
within 100 km from SGO and between azimuths: 281°<296°<310°	282	120	4.0	203.8

For investigation of the effect of EQs on the strain rate variation, the number and the released energy of EQs were compared to the strain rate. Despite the limited number of data (27) in the data series, correlation analysis was performed between strain rate data and the number and energy of EQs in each sector. Results are shown in Table 2. On the one hand the obtained small correlation coefficients cannot be considered to be significant (less than 0.7) due to the small number of data. On the other hand, they suggest that the direct effect of earthquakes on strain rate changes is less

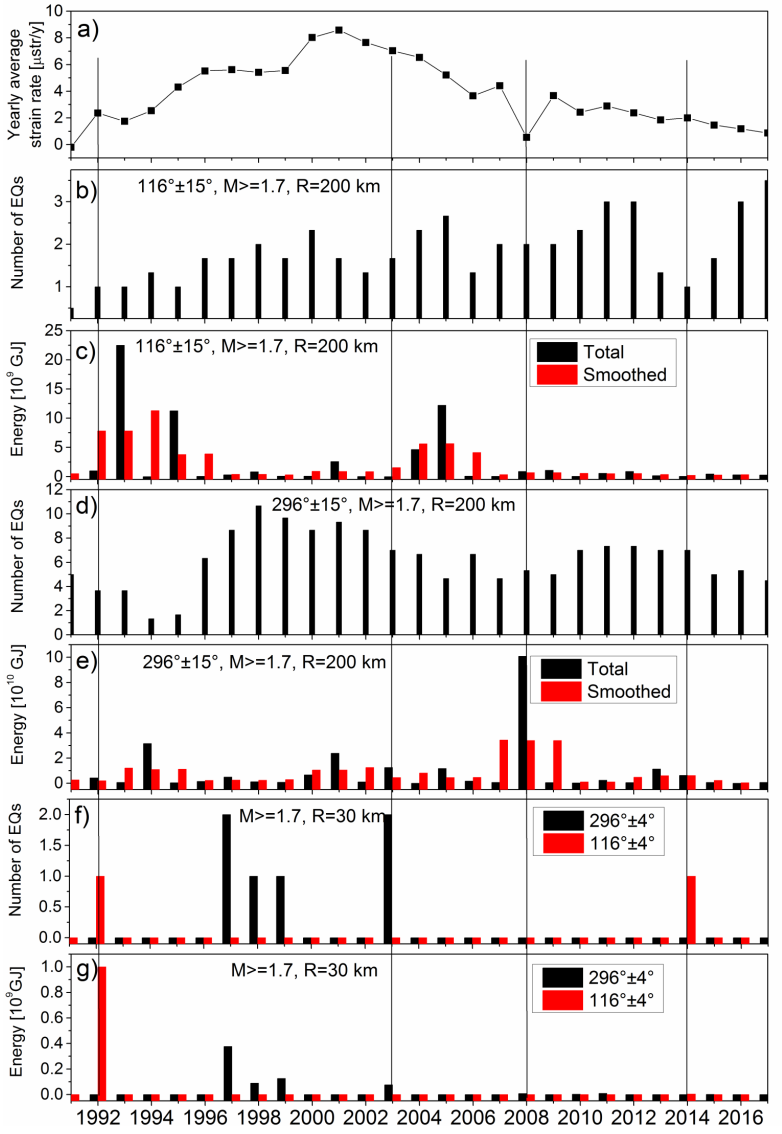

Fig. 4. Yearly strain rates (a), smoothed number (b) and energy of earthquakes (c) within 200 km from the SGO in the sector 116° ±15°, smoothed number (d) and energy of earthquakes (e) within 200 km from the SGO in the sector 296° ±15°, number (f) and energy (g) of earthquakes within 30 km from the SGO in the sectors 116° ±4° and 296° ±4°.

than that of other tectonic processes in the region. The correlation coefficients between the strain rate and the number and energy of EQs in the 296° sector (296 ±15° and 296 ±4°) are only between 0.20 and 0.53. The sign of the coefficients in the 296° sector is positive, while in the 116° sector is negative. Despite the small correlation coefficients, these results suggest that earthquakes in the 296 sector generally increase, while in sector 116 they reduce the rate of compression. Practically the same results were obtained when the numbers and energies of EQs in the sector 116° were subtracted from the same values in the sector 296° and these differences were correlated with the strain rate (see Table 2). However, the Fig. 4 also shows some opposite examples. In these cases, we can assume that the earthquakes had a direct effect on the rate of compression. The number of EQs and the released earthquake energy in the 116° ±15° (116° ±4°) sector increase the strain rate (see years 1992 and 2014 in the Fig. 4a,f–g) while in the opposite sector decrease it (see years 2003, 2008 in the Fig. 4a,f).

Table 2. Correlation coefficients between strain rate and the number (N) and energies (TE = total energy and SE = smoothed energy) of earthquakes in the different sectors.

	Sectors										Differences: S269−S116				
	116±15°			296±15°			116±4°		296±4°		±15°			±4°	
	N	TE	SE	N	TE	SE	N	SE	N	SE	N	TE	SE	N	SE
Corr. coeff.	0.00	−0.02	−0.02	0.53	−0.16	−0.03	−0.19	−0.12	0.36	0.25	0.53	−0.15	0.03	0.40	0.20

6. Discussion

The measured compression in the SGO is in good accordance with the GPS (Global position System) measurements in the Central European GPS Reference Network (CEGRN) (*Grenerczy et al., 2000, 2005; Caporali et al., 2008*). Strain rates from GPS data (from 1994 to 1998) in the CEGRN and in the Hungarian GPS Geodynamic Reference Network (HGRN) were determined in surroundings of the SGO (*Grenerczy et al., 2000*). In the region R1 contraction with a strain rate of –8.6 ±2.5 nstr y^{-1} in the NE–SW direction (see Fig. 1), but in the region R2 a NW–SE compression of −8.0 ± 5.3 nstr y^{-1} was obtained (see also *Tesauro et al., 2006*). *Bus et al. (2009)* determined a principal compressive strain rate –4.1 nstr y^{-1}

with a NEE–SWW direction in the Central Pannonian (CP) area from the HGRN data from 1991 to 2007 (see also *Caporali et al., 2009*). In the Mur-Mürz (MM) zone, parallel with the fault $-12\,\mathrm{nstr\,y^{-1}}$ compression, while perpendicular to it $9.6\,\mathrm{nstr\,y^{-1}}$ extension was obtained (*Fodor et al., 2005*). These directions correspond to forces moving the East Alpine-North Pannonian unit to the east, rotating it clockwise and the anticlockwise motion of the Adria microplate, causing compression in the Eastern Alps (*Caporali and Martin, 2000; Bada et al., 2007a; Caporali et al., 2008; Sánchez et al., 2018*). The results derived from borehole breakout, earthquake focal mechanism (FMS) and overcoring measurements in the vicinity of the MM zone show diverse local maximum compression strain directions (*Bada et al., 2007b; Olaiz et al., 2009; Brückl et al., 2010*). Some of them are parallel with the extensometer in the SGO. Thus we can assume that the direction of the extensometer is near to the direction of the principal compressive strain rate in this local region (see also *Olaiz et al., 2009; Bokelmann et al., 2013*). *Sánchez et al. (2018)* investigated the surface deformation of the Alpine region on the basis of GPS measurements. According to their results the deformation vectors in the Eastern Alps describe a progressive eastward rotation towards Pannonia and a shortening in the order of about $1\,\mathrm{mm\,y^{-1}}$. *Sternai et al. (2019)* found that the uplift rate of the Eastern Alps is about $1\,\mathrm{mm\,y^{-1}}$ characterized by shortening and crustal thickening, which probably can be explained by deglaciation, long-term erosion and dynamic processes related to the sub-lithospheric mantle flow. These processes can cause the ongoing Alpine elevation changes and can be responsible for the high and changing local compressive strain rate measured by the extensometer in the SGO.

The deformation in the Pannonian Basin is not uniform. It is concentrated mostly in the western and central parts of the basin (e.g. *Bada et al., 2007a*). The vertical movements, such as uplift and subsidence (*Horváth and Cloetingh, 1996; Bada et al., 1999*) induce horizontal strain (*Caporali, 2009*). The other reason for the high strain rate measured by the extensometer in the SGO is probably the difference of the vertical velocities in the East Alpine region and in the Pannonian Basin (*Cloetingh et al., 2005; Dombrádi et al., 2010*). The weak lithosphere (folding and compression) absorbs the strain in the Pannonian Basin (*Dombrádi et al., 2010*) while faults and earthquakes in the region relax it (*Bada et al., 2007b; Bus et*

al., 2009). Probably, this is the reason for the much smaller strain rates (in the order of nstr y^{-1}) obtained by GPS measurements in networks with 50–100 km base lines than strain rates (in the order of μstr y^{-1}) measured on short base lines (1–100 m) by extensometers. Similarly, in other observatories, local strain rates measured by extensometers are also in order of μstr y^{-1} (e.g. *Sato and Harrison, 1990; Braitenberg et al., 2001; Brimich, 2006; Takemoto et al., 2006*).

Time series measured at individual GPS stations show also daily and seasonal changes, which are also corrected (e.g. *Pellegrinelli et al., 2005; Serpelloni et al., 2005; Kontny et al., 2006; Tesauro et al., 2006; Hackl et al., 2011; Bogusz et al., 2012; Rajner and Liwosz, 2017; Sánchez et al., 2018; Sternai et al., 2019*) but the change of the rate of tectonic deformations are within the measurement uncertainty of this measurement technology. Therefore, extensometric measurements are still useful in the study of local tectonic deformations.

According to our results the rate of the compression is also affected by EQs in the investigated region of the observatory. A possible explanation that EQs in the sector $116° \pm 15°$ decrease or do not influence the rate of compression may be that the energy emitted by earthquakes are absorbed by the folding in the Pannonian Basin (*Cloetingh et al., 1999; Caporali, 2009; Dombrádi et al., 2010*). The released energy by the EQs in the sector $296° \pm 15°$ contributes to the compressive forces (*Bada et al., 2007b; Olaiz et al., 2009; Brückl et al., 2010; Salcher et al., 2012; Bokelmann et al., 2013*) in this region of the SGO, increasing the compressive strain rate. In some years, we found that earthquakes had a direct effect on the strain rate changes. However, in these cases their effect on the strain rate is in contrast to what was obtained by the correlation analysis described above.

7. Conclusions

The 27-year long strain measurements showed a compressive strain with varying rate at the foot of the Eastern Alps. The measured compressive strain is in good accordance with the GPS and geophysical strain measurements in the region of the SGO. We can assume that the uplift of the Alps, tectonic processes in the East Alpine region and in the Pannonian Basin

play the most important role in the varying strain rate. This assumption can be proven in the future by measurements in GPS networks with short baselines or by PSInSAR technology, which allows measurement of surface deformations in densely located points.

Our investigations show that earthquakes can also influence the strain rate. Earthquakes to the west of SGO generally increase the compressive strain rate, while earthquakes in the Pannonian Basin, with some exceptions, have no significant effect on the local strain rate variations measured in the SGO.

Based on our measurements, we can assume that in addition to GPS and PSInSAR measurements, continuous, long-term extensometric observations may play a very important role in investigation and understanding of local tectonic movements and deformations in the future.

Acknowledgements. This work was funded by the Hungarian National Research Fund (OTKA) under the project No. K 109060. Special thanks to Tibor Molnár for his careful maintenance of the instruments.

References

Bada G., Horváth F., Gerner P., Fejes I., 1999: Review of the present day geodynamics of the Pannonian basin: Progress and problems. J. Geodyn., **27**, 4-5, 501–527, doi: 10.1016/S0264-3707(98)00013-1.

Bada G., Grenerczy Gy., Tóth L., Horváth F., Stein S., Cloetingh S., Windhoffer G., Fodor L., Pinter N., Fejes I., 2007a: Motion of Adria and ongoing inversion of the Pannonian Basin: Seismicity, GPS velocities and stress transfer. In: S.Stein, S. Mazzotti, (Eds.), Continental Intraplate Earthquakes: Science, Hazard, and Policy Issues. Geological Society of America Special Papers, **425**, 16, 243–262, doi: 10.1130/2007.2425(16).

Bada G., Horváth F., Dövényi P., Szafián P., Windhoffer G., Clothing S., 2007b: Present-day stress field and tectonic inversion in the Pannonian basin. Glob. Planet. Change, **58**, 1-4, 165–180, doi: 10.1016/j.gloplacha.2007.01.007.

Bán D., Mentes Gy., Kis M., Koppán A., 2018: Observation of the Earth liquid core resonance by extensometers. Pure Appl. Geophys., **175**, 5, 1631–1642, doi: 10.1007/s00024-017-1724-6.

Bogusz J., Figurski M., Kontny B., Grzempowski P., 2012: Horizontal velocity field derived from EPN and ASG-EUPOS satellite data on the example of south-western part of Poland. Acta Geodyn. Geomater., **9**, 3, 349–357.

Bokelmann G., Qorbani E., Bianchi I., 2013: Seismic anisotropy and large-scale deformation of the Eastern Alps. Earth Planet Sci. Lett., **383**, 1–6, doi: 10.1016/j.epsl.2013.09.019.

Braitenberg C., Nagy I., Negusini M., Romagnoli C., Zadro M., Zerbini S., 2001: Geodetic measurements at the northern border of the Adria plate. J. Geodyn., **32**, 1-2, 267–286, doi: 10.1016/S0264-3707(01)00025-4.

Brimich L., Kohút I., Kostecký P., 1998: Influence of the Cavity Effect on Tidal Measurements. In: Ducarme B., Paquet P., (Eds.): Proceedings of the 13th International Symposium on Earth Tides, Brussels, Observatoire royal de Belgique, pp. 397–412.

Brimich L., 2006: Strain measurements at the Vyhne tidal station. Contrib. Geophys. Geod., Geophysical Institute of the Slovak Academy of Sciences, **36**, 4, 361–371.

Brückl E., Behm M., Decker K., Grad M., Guterch A., Keller G. R., Thybo H., 2010: Crustal structure and active tectonics in the Eastern Alps. Tectonics, **29**, 2, TC2011, doi: 10.1029/2009TC002491.

Burgmann R., Rosen P. A., Fielding E. J., 2000: Synthetic aperture radar interferometry to measure Earth's surface topography and its deformation. Annu. Rev. Earth Planet. Sci., **28**, 169–209, doi: 10.1146/annurev.earth.28.1.169.

Bus Z., Grenerczy Gy., Tóth L., Mónus P., 2009: Active crustal deformation in two seismogenic zones of the Pannonian region – GPS versus seismological observations. Tectonophysics, **474**, 1-2, 343–352, doi: 10.1016/j.tecto.2009.02.045.

Caporali A., 2009: Lithospheric flexure, uplift and expected horizontal strain rate in the Pannonian Carpathian region. Tectonophysics, **474**, 1, 337–342, doi: 10.1016/j.tecto.2008.10.033.

Caporali A., Martin S., 2000: First results from GPS measurements on present day Alpine kinematics. J. Geodyn., **30**, 1, 275–283, doi: 10.1016/S0264-3707(99)00037-X.

Caporali A., Aichhorn C., Becker M., Fejes I., Gerhatova L., Ghitau D., Grenerczy G., Hefty J., Krauss S., Medak D., Milev G., Mojzes M., Mulic M., Nardo A., Pesec P., Rus T., Simek J., Sledzinski J., Solaric M., Stangl G., Vespe F., Virág G., Vodopivec F., Zablotskyi F., 2008: Geokinematics of Central Europe: new insights from the CERGOP-2/Environment Project. J. Geodyn., **45**, 4-5, 246–256, doi: 10.1016/j.jog.2008.01.004.

Caporali A., Aichhorn C., Barlik M., Becker M., Fejes I., Gerhatova L., Ghitau L., Grenerczy Gy., Hefty J., Krauss S., Medak D., Milev G., Mojzes M., Mulic M., Nardo A., Pesec P., Rus T., Simek J., Sledzinski J., Solaric M., Stangl G., Stopar B., Vespe F., Virág G., 2009: Surface kinematics in the Alpine–Carpathian–Dinaric and Balkan region inferred from a new multi-network GPS combination solution. Tectonophysics, **474**, 1-2, 295–321, doi: 10.1016/j.tecto.2009.04.035.

Cloetingh S., Burov E., Poliakov A., 1999: Lithosphere folding: Primary response to compression? (from central Asia to Paris basin). Tectonics, **18**, 6, 1064–1083, doi: 10.1029/1999TC900040.

Cloetingh S., Maţenco L., Bada G., Dinu C., Mocanu B., 2005: The evolution of the Carpathians–Pannonian system: interaction between neotectonics, deep structure,

polyphase orogeny and sedimentary basins in a source to sink natural laboratory. Tectonophysics, **410**, 1-4, 1–14, doi: 10.1016/j.tecto.2005.08.014.

Dal Moro G., Zadro M., 1998: Subsurface deformations induced by rainfall and atmospheric pressure: tilt/strain measurements in the NE Italy seismic area. Earth Planet. Sci. Lett., **164**, 1-2, 193–203, doi: 10.1016/S0012-821X(98)00203-9.

Decker K., Peresson H., Hinsch R., 2005: Active tectonics and Quaternary basin formation along the Vienna Basin Transform fault. Quat. Sci. Rev., **24**, 3-4, 307–322, doi: 10.1016/j.quascirev.2004.04.012.

Dombrádi E., Sokoutis D., Bada G., Cloetingh S., Horváth F., 2010: Modelling recent deformation of the Pannonian lithosphere: Lithospheric folding and tectonic topography. Tectonophysics, **484**, 1-4, 103–118, doi: 10.1016/j.tecto.2009.09.014.

Farrell W. E., 1972: Deformation of the Earth by surface loads. Rev. Geophys., **10**, 3, 761–797, doi: 10.1029/RG010i003p00761.

Fodor L., Bada G., Csillag G., Horváth E., Ruszkiczay-Rudiger Zs., Palotás K., Sikhegyi F., Timár G., Cloetingh S., Horváth F., 2005: An outline of neotectonic structures and morphotectonics of the western and central Pannonian Basin. Tectonophysics, **410**, 1, 15–41, doi: 10.1016/j.tecto.2005.06.008.

Gebauer A., Kroner C., Jahr T., 2009: The influence of topographic and lithologic features on horizontal deformations. Geophys. J. Int., **177**, 2, 586–602, doi: 10.1111/j.1365-246X.2009.04072.x.

Gebauer A., Steffen H., Kroner C., Jahr T., 2010: Finite element modelling of atmosphere loading effects on strain, tilt and displacement at multi-sensor stations. Geophys. J. Int., **181**, 3, 1593–1612, doi: 10.1111/j.1365-246X.2010.04549.x.

Gráczer Z., Czifra T., Kiszely M., Mónus P., Zsíros T., 2012–2016: Hungarian National Seismological Bulletin 2011–2016 (Magyar Nemzeti Szeizmológiai Bulletin 2011–2016). Budapest: Kövesligethy Radó Szeizmologiai Obszervatórium, MTA CSFK GGI.

Grenerczy Gy., Kenyeres A., Fejes I., 2000: Present crustal movement and strain distribution in Central Europe inferred from GPS measurements. J. Geophys. Res., **105**, B9, 21835–21846, doi: 10.1029/2000JB900127.

Grenerczy Gy., Sella G., Stein S., Kenyeres A., 2005: Tectonic implications of the GPS velocity field in the northern Adriatic region. Geophys. Res. Lett., **32**, 16, L16311, doi: 10.1029/2005GL022947.

Gutenberg B., Richter F., 1942: Earthquake magnitude, intensity, energy and acceleration. Bull. Seismol. Soc. Am., **32**, 3, 163–191.

Haas J. (Ed.), 2001: Geology of Hungary. Budapest: Eötvös University Press.

Hackl M., Malservisi R., Hugentobler U., Wonnacott R., 2011: Estimation of velocity uncertainties from GPS time series: Examples from the analysis of the South African TrigNet network. J. Geophys. Res., **116**, B11404, doi: 10.1029/2010JB008142.

Hanssen R. F., 2001: Radar Interferometry: Data Interpretation and Error Analysis. Kluwer Academic Publishers, Dordrecht, pp. 328.

Harrison J. C., 1976: Cavity and topographic effects in tilt and strain measurements. J. Geophys. Res., **81**, 2, 319–328, doi: 10.1029/JB081i002p00319.

Horváth F., Cloetingh S., 1996: Stress-induced late stage subsidence anomalies in the Pannonian basin. Tectonophysics, **266**, 1-4, 287–300, doi: 10.1016/S0040-1951(96)00194-1.

Kisházi P., Ivancsics J., 1985: Genetic petrology of the Sopron crystalline schist sequence. Acta Geol. Hung., **28**, 3–4, 191–213.

Kontny B., Bosy J., Borkowski A., 2006: The use of permanent and epoch GPS coordinate time series in geodynamic investigations of Sudetes area – proposal of a new approch. Acta Geodyn. Geomater., **3**, 3(143), 31–38.

Krásná H., Malkin Z., Böhm J., 2015: Non-linear VLBI station motions and their impact on the celestial reference frame and the Earth orientation parameters. J. Geod., **89**, 10, 1019–1033, doi: 10.1007/s00190-015-0830-4.

Krásná H., Ros C. T., Pavetich P., Böhm J., Nilsson T., Schuh H., 2013: Investigation of crustal motion in Europe by analysing the European VLBI sessions. Acta Geod. Geophys., **48**, 4, 389–404, doi: 10.1007/s40328-013-0034-4.

Kroner C., Jahr T., Kuhlmann S., Fischer K. D., 2005: Pressure induced noise on horizontal seismometer and strainmeter records evaluated by finite element modelling. Geophys. J. Int., **161**, 1, 167–178, doi: 10.1111/j.1365-246X.2005.02576.x.

Massonnet D., Feigl K. L., 1998: Radar interferometry and its application to changes in the Earth's surface. Rev. Geophys., **36**, 4, 441–500, doi: 10.1029/97RG03139.

Mentes Gy., 2000: Influence of Temperature and Barometric Pressure Variations on Extensometric Deformation Measurements at the Sopron Station. Acta Geod. Geophys. Hu., **35**, 3, 277–282, doi: 10.1007/BF03325617.

Mentes Gy., 2010: Quartz tube extensometer for observation of Earth tides and local tectonic deformations at the Sopronbánfalva Geodynamic Observatory, Hungary. Rev. Sci. Instrum., **81**, 7, 074501, doi: 10.1063/1.3470100.

Mentes Gy., 2012: Observation of local tectonic movements by a quartz-tube extensometer in the Sopronbanfalva Geodynamic Observatory, in Hungary – Validation of extensometric data by tidal analysis and simultaneous radon concentration measurements. J. Geodyn., **58**, 38–43, doi: 10.1016/j.jog.2012.01.004.

Müller T., Zürn W., 1983: Observation of gravity changes during the passage of cold fronts. J. Geophys., **53**, 155–162.

Olaiz A. J., Muñoz-Martín A., De Vicente G., Vegas R., Cloetingh S., 2009: European continuous active tectonic strain–stress map. Tectonophysics, **474**, 1, 33–40, doi: 10.1016/j.tecto.2008.06.023.

Onoue K., Takemoto S., 1998: Atmospheric pressure effect on ground strain observation at Donzurubo Observatory, Nara, Japan. In: Ducarme B., Paquet P., (Eds.), Proceedings of the 13th International Symposium on Earth Tides, Brussels: Observatoire royal de Belgique, pp. 157–164.

Pellegrinelli A., Perfetti N., Russo P., 2005: Time series analysis of daily solutions of IGFN permanent GPS stations. B. Geofis. Teor. Appl., **46**, 2–3, 85–97.

Plank L., Böhm J., Schuh H., 2014: Precise station positions from VLBI observations to satellites: a simulation study. Journal of Geodesy, **88**, 7, 659–673, doi: 10.1007/s00190-014-0712-1.

Rabbel W., Zschau J., 1985: Static deformations and gravity changes at the Earth's surface due to atmospheric loading. J. Geophys., **56**, 81–99.

Rajner M., Liwosz T., 2017: Analysis of seasonal position variation for selected GNSS sites in Poland using loading modelling and GRACE data. Geod. Geodyn., **8**, 4, 253–259, doi: 10.1016/j.geog.2017.04.001.

Salcher B. C., Meurers B., Smit J., Decker K., Hölzel M., Wagreich M., 2012: Strike-slip tectonics and Quaternary basin formation along the Vienna Basin fault system inferred from Bouguer gravity derivatives. Tectonics, **31**, 3, TC3004, doi: 10.1029/2011TC002979.

Sánchez L., Völksen C., Sokolov A., Arenz H., Seitz F., 2018: Present-day surface deformation of the Alpine region inferred from geodetic techniques. Earth Syst. Sci. Data, **10**, 1503–1526, doi: 10.5194/essd-10-1503-2018.

Sato T., Harrison J.C., 1990: Local effects on tidal strain measurements at Esashi, Japan. Geophys. J. Int., **102**, 3, 513–526, doi: 10.1111/j.1365-246X.1990.tb04577.x.

Serpelloni E., Anzidei M., Baldi P., Casula G., Galvani A., 2005: Crustal velocity and strain-rate fields in Italy and surrounding regions: new results from the analysis of permanent and non-permanent GPS networks. Geophys. J. Int., **161**, 3, 861–880, doi: 10.1111/j.1365-246X.2005.02618.x.

Síkhegyi F., 2002: Active Structural Evolution of the Western and Central Parts of the Pannonian Basin: a Geomorphological Approach, vol. 3. EGU Stephan Mueller Special Publication Series pp. 203–216.

Steffen H., Kuhlmann S., Jahr T., Kroner C., 2006: Numerical Modeling of the Barometric Pressure-Induced Noise in Horizontal Components for the Observatories Moxa and Schiltach. J. Geodyn., **41**, 1-3, 242–252, doi: 10.1016/j.jog.2005.08.011.

Sternai P., Sue C., Husson L., Serpelloni E., Becker T. W., Willett S. D., Faccenna C., Di Giulio A., Spada G., Jolivet L., Valla P., Petit C., Nocquet J.-M., Walpersdorf A., Sébastien Castelltort S., 2019: Present-day uplift of the European Alps: Evaluating mechanisms and models of their relative contributions. Earth-Sci. Rev., **190**, 589–604, doi: 10.1016/j.earscirev.2019.01.005.

Sun H. P., Ducarme B., Dehant V., 1995: Effect of the atmospheric pressure on surface displacement. J. Geod., **70**, 3, 131–139, doi: 10.1007/BF00943688.

Takemoto S., Lee M., Chen C.-Y., Kao M.-C., Mukai A., Ikawa T., Kuroda T., Abe T., 2006: Tidal strain observations in Chu-Chie, Taiwan. J. Geodyn., **41**, 1–3, 198–204, doi: 10.1016/j.jog.2005.08.004.

Tesauro M., Hollenstein C., Egli R., Geiger A., Kahle H.-G., 2006: Analysis of central western Europe deformation using GPS and seismic data. J. Geodyn., **42**, 4-5, 194–209, doi: 10.1016/j.jog.2006.08.001.

Tóth L., Mónus P., Bus Z., Györi E., 2008: Seismicity of the Pannonian Basin. In: Husebye E.S., eds) Earthquake Monitoring and Seismic Hazard Mitigation in Balkan Countries. NATO Science Series: IV: Earth and Environmental Sciences, Vol 81. Dordreht: Springer.

Tóth L., Mónus P., Zsíros T., Bondár I., Bus Z., Kosztyu Z., Kiszely M., Wéber Z., Czifra T. 1996–2018: Hungarian earthquake bulletin, 1995–2017. MTA GGKI és Georisk Kft, Budapest.

Varga P., Varga T., 1994: Recent horizontal deformation in the Pannonian Basin measured with extensometers. Acta Geod. Geophys. Hu., **29**, 1, 57–80.

Venedikov A. P., Arnoso J., Cai W., Vieira R., Tan S., Velez E. J., 2006: Separation of the long-term thermal effects from the strain measurements in the Geodynamics Laboratory of Lanzarote. J. Geodyn., **41**, 1–3, 213–220, doi: 10.1016/j.jog.2005.08.029.

Ward S. N., 1994: Constraints on the seismotectonics of the central Mediterranean from very long baseline interferometry. Geophys. J. Int., **117**, 2, 441–452, doi: 10.1111/j.1365-246X.1994.tb03943.x.

Wenzel H. G., 1996: The nanogal software: Earth tide data processing package ETERNA 3.30. Bulletin d'Information Marées Terrestres, **124**, 9425–9439.

Zürn W., Exß J., Steffen H., Kroner C., Jahr T., Westerhaus M., 2007: On reduction of long-period horizontal seismic noise using local barometric pressure. Geophys. J. Int., **171**, 2, 780–796, doi: 10.1111/j.1365-246X.2007.03553.x.

ZAMG, 2018: Austrian Earthquake Catalogue (AEC), Wien: Central Institute for Meteorology and Geodynamics (ZAMG), Geophysical Department.